Evaluation of a Soil Radar Backscatter Model with Applicability to Radar Observations of a sub-Arctic Environment

by

Ryan Ahola

A thesis
presented to the University of Waterloo
in fulfillment of the
thesis requirement for the degree of
Master of Science
in
Geography

Waterloo, Ontario, Canada, 2013

© Ryan Ahola 2013

Author's Declaration

I hereby declare that I am the sole author of this thesis. This is a true copy of the thesis, including any required final revisions, as accepted by my examiners.

I understand that my thesis may be made electronically available to the public.

Abstract

This research explores the applicability of a semi-empirical soil backscatter model for estimating X-band (9.35-9.85 GHz) backscatter from snow covered sub-Arctic terrain in the Hudson Bay Lowlands, Manitoba, Canada. The studied radar frequencies and model have been identified for potential use within Snow Water Equivalent (SWE) retrievals for future remote sensing missions. In open tundra environments, the predominant X-band response is controlled by soil frozen status, soil moisture and soil surface roughness. Snow in these environments is expected to have little influence on backscatter due to the transparent nature of shallow snowpacks at this frequency. Therefore, understanding a backscatter model's sensitivity to soil parameters is of primary concern for appropriate use under sub-Arctic terrain conditions.

Using measurements and estimates of soil complex relative permittivity (ϵ_r) as well as a series of *in situ* soil surface roughness measurements for parameterization, backscatter model estimates are compared with two X-band remote sensing observation datasets obtained between October 2010 and May 2011: 1) ground-based scatterometer measurements acquired by the University of Waterloo Scatterometer (UW-Scat), and 2) TerraSAR-X observations of the same region. Comparisons reveal mixed agreement between the remote sensing measurements and backscatter model estimates, with average differences ranging from -0.76 to 11.43 dB. This range of agreement occurred from two sources: 1) comparisons with TerraSAR-X VV measurements, and 2) variations in agreement between *in situ* soil surface roughness measurements used to parameterize the backscatter model. Backscatter model comparisons with TerraSAR-X VV measurements achieved an average difference of $\sim$1.0 dB for the study period, the greatest agreement observed for all remote sensing measurements. The largest RMS soil surface roughness produced backscatter model estimates which achieved the greatest agreement for almost all UW-Scat and TerraSAR-X measurements. Smoother roughness observations achieved lower agreement, more than 10 dB in some cases. While TerraSAR-X VV measurements and *in situ* soil surface roughness observations contributed to the range of differences, overall agreement was typically $\sim$6 dB, indicating poor agreement for the majority of backscatter model, UW-Scat and TerraSAR-X comparisons. These results thus illustrate substantial challenges for application of the backscatter model within dual-frequency SWE retrieval frameworks, without proper incorporation of roughness, soil moisture and ϵ_r for the areas under observation.

Results from this study reveal uncertainties in the applicability of the soil backscatter model for sub-Arctic terrain of the Hudson Bay Lowlands. While good agreement was observed for TerraSAR-X VV measurements, poor and varied agreement for the remaining ground and satellite-based measurements suggests the current modelling framework needs

improvement for use in sub-Arctic terrain. By improving the characterization of the Hudson Bay Lowlands region, a better understanding of the nature of sub-Arctic terrain parameters required for this application can be achieved. This may also lead to improved modelling frameworks for representing sub-Arctic terrain within future satellite missions.

Acknowledgements

This thesis would not have been possible without the help and support of many individuals. My supervisor, Dr. Richard Kelly, provided the initial inspiration for my undergraduate thesis which led to this Masters project. Without his continuous guidance and support, I would not have maintained the drive to complete this work. The success of this work as well as my future prospects are due much to his efforts, and is something which I will never be able to fully thank him for.

I also owe many thanks to Joshua King and Andrew Kasurak who answered innumerable questions and substantially improved the focus of my research. I have been very fortunate to learn from them and will sorely miss having quick access to their ideas and opinions. I would also like to thank everyone else in the UW Cryosphere group for their guidance and support throughout my time at UW. These individuals have been the best group of people I have ever worked with and I am much better off having getting to know all of them. I certainly hope that I will be able to work with everyone again in the future.

To my parents, Allen and Pat, I owe tremendous thanks. Your support during my undergraduate and graduate degrees helped me get through all the work and stress and has helped me become the person I am. My parents initial encouragement to attend UW directly led to this research, something which I cannot thank them enough for.

Finally, to my girlfriend Liza, I owe the most thanks. The experience of your support, laughter and love everyday is something that I cannot come close to describing. I would not have gotten through this research without you and I am thankful everyday that I am fortunate enough to know you. I can't wait to see what's next for us.

Table of Contents

Author's Declaration ii

Abstract iii

Acknowledgements v

List of Tables viii

List of Figures ix

List of Acronyms xii

List of Symbols xiv

1 Introduction 1

1.1 Objectives 2

1.2 Thesis Structure 3

2 Active Microwave Remote Sensing of Snow Covered Landscapes 4

2.1 The Active Microwave Process 4

2.2 Factors Affecting Active Microwave Remote Sensing of Snow-Covered Landscapes 7

2.2.1 Influence of Signal Properties 8

2.2.2 Influence of Surface Properties . . . 10
2.2.3 Summary . . . 15
2.3 Research Motivation: Understanding and Quantifying X-band Response from a Cold Season Tundra Landscape . . . 16

3 Research Study Site **18**
3.1 Site Location . . . 18
3.2 Climate . . . 19
3.3 Specific Site Characteristics . . . 20
3.4 Summary . . . 21

4 Methodology **23**
4.1 Overview . . . 23
4.2 Remote Sensing Measurements . . . 24
4.2.1 Ground-Based Scatterometer . . . 24
4.2.2 TerraSAR-X . . . 27
4.3 Models . . . 29
4.3.1 Oh Model . . . 29
4.3.2 Temperature-Dependable Generalized Refractive Mixing Dielectric Model (TD GRMDM) . . . 33
4.4 Field Measurements . . . 43
4.4.1 Surface Roughness Sampling . . . 43
4.4.2 Surface Roughness Picture Processing . . . 44
4.4.3 Roughness Used within the Oh Model . . . 46
4.5 Laboratory Measurements . . . 46
4.5.1 Sample Description . . . 48
4.5.2 Measurement Overview . . . 48
4.6 Analysis Methodology . . . 54
4.6.1 TD GRMDM Evaluation . . . 54
4.6.2 Oh Model Evaluation . . . 55

5 Results & Discussion **57**

5.1 TD GRMDM Evaluation 58

5.1.1 Ground-Up Sample Measurements (Stage 3) Results 58

5.1.2 Small Sample Measurements (Stage 2) Results 63

5.1.3 Whole Sample Measurements (Stage 1) Results 66

5.1.4 TD GRMDM Evaluation Discussion 68

5.2 Oh Model Evaluation 70

5.2.1 Agreement using TD GRMDM ϵ_r 70

5.2.2 Agreement Results using Measured ϵ_r 78

5.2.3 Oh Model Evaluation Discussion 82

5.3 Oh Model Applicability within Potential Dual-Frequency SWE Retrieval Missions 83

5.4 Recommendations for Oh Model Improvement 85

6 Conclusion **87**

APPENDICES **89**

A TD GRMDM Evaluation Plots for Bottom Peat Samples **90**

References **98**

List of Tables

4.1 UW-Scat and TerraSAR-X Acquisition Dates 26

4.2 TD GRMDM Coefficients for Equations 4.9 and 4.10 37

4.3 TD GRMDM Coefficients for Equation 4.11 38

4.4 TD GRMDM Coefficients for Equation 4.12 39

4.5 TD GRMDM Evaluation Soil Parameters 55

5.1 TerraSAR-X and UW-Scat vs. Oh Model using TD GRMDM ϵ_r Agreement Statistics 72

5.2 TerraSAR-X and UW-Scat vs. Oh Model using Measured ϵ_r Agreement Statistics 81

List of Figures

3.1 Study Site Location 19
3.2 Tundra Study Site Characteristics 20
3.3 Churchill Meteorological Conditions 22

4.1 Study Site Measurement Locations 25
4.2 UW-Scat Set-Up 27
4.3 TerraSAR-X Acquisitions Footprint 28
4.4 Processed TerraSAR-X Scene 29
4.5 Oh Model Evaluation 32
4.6 Surface Roughness Pin Board and Frame 44
4.7 Back to Back Roughness Measurement Set-up 45
4.8 Processed Surface Roughness Picture Example 46
4.9 Pin Board and Ground Roughness Pictures for 0.62 cm Level 47
4.10 Pin Board and Ground Roughness Pictures for 1.15 cm and 1.84 cm Levels 47
4.11 Peat Sample Description 49
4.12 Stevens Hydra Probe II Accuracy Evaluation 50
4.13 Instrumentation of Whole Peat Sample 51
4.14 Small Peat Samples 52
4.15 Ground-Up Peat Samples 53

5.1 Experiment Comparison Work-flow 58

5.2 Measured and TD GRMDM Estimated $\epsilon_r^{'}$ Agreement for Ground-Up Top Peat Sample 59
5.3 Measured and TD GRMDM Estimated $\epsilon_r^{''}$ Agreement for Ground-Up Top Peat Sample 60
5.4 Differences between Measured and TD GRMDM Estimated $\epsilon_r^{'}$ for Ground-Up Top Peat Sample 61
5.5 Differences between Measured and TD GRMDM Estimated $\epsilon_r^{''}$ for Ground-Up Top Peat Sample 62
5.6 Measured and TD GRMDM Estimated $\epsilon_r^{'}$ and $\epsilon_r^{''}$ Agreement for the Small Top Peat Sample 64
5.7 Differences between Measured and TD GRMDM Estimated $\epsilon_r^{'}$ and $\epsilon_r^{''}$ for Small Scale Top Peat Sample 65
5.8 Agreement and Differences between Measured and TD GRMDM Estimated $\epsilon_r^{'}$ and $\epsilon_r^{''}$ for Top Portion of Whole Peat Sample 67
5.9 Ground-Up Top Sample at 4.45 g/g Moisture Content 69
5.10 TD GRMDM ϵ_r for Oh Model 73
5.11 Oh model and UW-Scat Agreement using TD GRMDM ϵ_r 74
5.12 Oh model and UW-Scat Correlation using TD GRMDM ϵ_r 75
5.13 Oh model and TerraSAR-X Agreement using TD GRMDM ϵ_r 76
5.14 Oh model and TerraSAR-X Correlation using TD GRMDM ϵ_r 77
5.15 Oh model and UW-Scat Agreement using Measured ϵ_r 79
5.16 Oh model and TerraSAR-X Agreement using Measured ϵ_r 80

A.1 Measured and TD GRMDM Estimated $\epsilon_r^{'}$ Agreement for Ground-Up Bottom Peat Sample 91
A.2 Measured and TD GRMDM Estimated $\epsilon_r^{''}$ Agreement for Ground-Up Bottom Peat Sample 92
A.3 Differences between Measured and TD GRMDM Estimated $\epsilon_r^{'}$ for Ground-Up Bottom Peat Sample 93
A.4 Differences between Measured and TD GRMDM Estimated $\epsilon_r^{''}$ for Ground-Up Bottom Peat Sample 94

A.5 Measured and TD GRMDM Estimated $\epsilon_r^{'}$ and $\epsilon_r^{''}$ Agreement for the Small Bottom Peat Sample 95

A.6 Differences between Measured and TD GRMDM Estimated $\epsilon_r^{'}$ and $\epsilon_r^{''}$ for Small Bottom Peat Sample 96

A.7 Agreement and Differences between Measured and TD GRMDM Estimated $\epsilon_r^{'}$ and $\epsilon_r^{''}$ for Bottom Portion of Whole Peat Sample 97

List of Acronyms

CoReH$_2$O	Cold Regions Hydrology High-Resolution Observatory
CST	Central Standard Time
CDT	Central Daylight Time
CRI	Complex Refractive Index
dB	decibels
ESA	European Space Agency
GIMP	GNU Image Manipulation Program
GO	Geometric Optics Model
HBL	Hudson Bay Lowlands
MGFBW	Maximum Gravimetric Fraction of Bound Water
MGFUW	Maximum Gravimetric Fraction of Unfrozen Water
NAC	Normalized Attenuation Coefficient
NEST	Next ESA Synthetic Aperture Radar Toolbox
PO	Physical Optics Model
RCS	Radar Cross Section
RI	Refractive Index
RMS	Root Mean Square

RMSE	Root Mean Square Error
SPM	Small Perturbation Method
SWE	Snow Water Equivalent
sRT	Semi-Empirical Radiative Transfer Model
TD GRMDM	Temperature-Dependable Generalized Refractive Mixing Dielectric Model
UTC	Coordinated Universal Time
UW-Scat	University of Waterloo Scatterometer

List of Symbols

σ	Radar Cross Section
σ_{ref}	Reference RCS
A_r	Radar Sensor Aperture
G_t	Transmitting Antenna Gain
P_σ	Incident Energy Available for Scattering
P_r	Actual Power of Signal Received at Sensor
p_r	Power Density at Sensor
$\bar{x}(l)$	Mean of Pin Board RMS Calculation Transition Positions
$\beta_{\sigma p}$	TD GRMDM Derivative of Conductivity for a given p
β_{vqp}	TD GRMDM Volumetric Expansion Coefficient for ϵ_r Limits
ΔH_p	TD GRMDM Activation Energy of Relaxation Process for a given p
ΔS_p	TD GRMDM Entropy of Activation for a given p
ϵ_0	Vacuum Permittivity
ϵ_{qp}	TD GRMDM Low (q=0) or High (q=∞) Frequency ϵ_r Limits for Bound (p=b), Unbound (p=u), Transient (p=t) or Moistened Ice Water (p=iw) Soil Water Conditions (p)
$\epsilon_r^{''}$	Imaginary Portion of Complex Relative Permittivity
$\epsilon_r^{'}$	Real Portion of Complex Relative Permittivity

ϵ_0 Free Space Permittivity

ϵ_r Complex Relative Permittivity

$\frac{(n_m-1)}{\rho_m}$ TD GRMDM RI for m

$\frac{\kappa_m}{\rho_m}$ TD GRMDM NAC for m

$\frac{n_s^*-1}{\rho_d(m_g)}$ TD GRMDM Soil CRI

Γ_h Fresnel Reflectivity for Horizontal Polarization

Γ_o Fresnel Reflectivity

Γ_v Fresnel Reflectivity for Vertical Polarization

κ_p TD GRMDM Imaginary Portion of Complex Frequency Dependence of a given p

$\kappa_p(f,T)$ NAC for a given p Dependent on f and T

λ Wavelength

ln Natural Logarithm

ρ_b TD GRMDM Density of Bound Water

ρ_d Bulk Density of Dried Soil Samples

ρ_t TD GRMDM Density of Transient Water

ρ_u TD GRMDM Density of Unbound Water

ρ_{iw} TD GRMDM Density of Moistened Ice Water

ρ TD GRMDM Density

σ^o Oh Model Backscatter

σ^o_{hh} Oh Model HH Backscatter

σ^o_{hv} Oh Model HV Backscatter

σ^o_{vv} Oh Model VV Backscatter

$\sigma_p(T)$ TD GRMDM Soil Conductivity at a given T for a given p

σ Standard Deviation of Surface Height at Target

σ^o Scattering Coefficient of Average RCS

$\tau_p(ps)$ TD GRMDM Relaxation Time for a given p

θ Incident Angle

b TD GRMDM Bound Water

$d\sigma$ RCS of Theoretical Areas of Features within RCS

$d\sigma/ds$ Average RCS per Unit Area of the Target

dP_r Scattering Coefficient of the Target

ds Theoretical Area of Features within RCS

f Frequency

F_{qp} TD GRMDM Low and High Frequency ϵ_r Limits for Soil Water Conditions for $T_{s\epsilon qp}$

g Coefficient for Oh Model VV Backscatter

G_r Receiving Antenna Gain

i Total Number of Position Measurements for Pin Board RMS Calculation

iv TD GRMDM Moistened Ice Water

j $\sqrt{-1}$

k Wavenumber

ks Oh Soil Surface Roughness Representation in terms of Signal Wavenmuber and Soil Surface RMS Height

l Position of Transition from Black to White for Pin Board RMS Calculation

m TD GRMDM Soil Solids

M_c Container Mass for mg Calculation

M_d Mass of Dried Soil for Bulk Density Calculation

m_g Gravimetric Soil Moisture

M_w Amount of Water Required to Achieve a given mg

M_{cds} Mass of Dried Soil and Contained for mg Calculation

M_{cms} Mass of Moist Soil and Sample Contained for mg Calculation

M_{ds} Mass of Dry Soil Sample for Calculation of Water Required to Achieve a given mg

m_{g1} TD GRMDM MGFBW

m_{g1} TD GRMDM MGFUW

n_b^* TD GRMDM CRI for Bound Water

n_{iw}^* TD GRMDM CRI for Moistened Ice Water

n_p^* TD GRMDM Complex Frequency Dependence of a given p

n_t^* TD GRMDM CRI for Transient Soil Water

n_u^* TD GRMDM CRI for Unbound Water

n_p TD GRMDM Real Portion of Complex Frequency Dependence of a given p

$n_p(f,T)$ TD GRMDM RI for a given p Dependent on f and T

p Oh Model Co-Polarized Ratio

p_d Soil Bulk Density

p_i Radar Signal Power Density at Target

P_t Transmitted Power

q Oh Model Cross-Polarized Ration

R Distance Between Target and Sensor

R TD GRMDM Universal Gas Constant

r_a Azimuth Resolution

r_g Range Resolution

s	Soil Surface RMS Height
T	Temperature
t	TD GRMDM Transient Water
T_f	TD GRMDM Soil Freezing Temperature
T_K	TD GRMDM Soil Temperature in K
$T_s\sigma p$	TD GRMDM Initial Temperature for Conductivity Estimate Calibration for a given p
$T_{s\epsilon qp}$	TD GRMDM Starting Temperature for ϵ_{qp}
u	Heaviside Step Function
u	TD GRMDM Unbound Water
V	Volume of Dried Soil Sample for Bulk Density Calculation
w	Gravimetric Moisture Water Content

Chapter 1

Introduction

Dual-frequency remote sensing approaches may present the most appropriate option for snow monitoring on a global scale, particularly for the retrieval of Snow Water Equivalent (SWE) levels. Ku- and X-band frequencies (12-18 and 8-12.5 GHz respectively) are viewed as particularly beneficial to snow monitoring due to their differing sensitivities to seasonal terrestrial snow and its background soil media. Typically, Ku-band demonstrates higher sensitivity to snow due to its lower penetration depth of 3 to 5 m, in comparison to X-band's penetration capability of ∼10 m (Ulaby *et al.*, 1984; Mätzler, 1987; Rott *et al.*, 1993). Therefore, in dry terrestrial snow environments, X-band backscatter is sensitive to sub-nivean ground surface dielectric properties, while Ku-band observations provide understanding of snowpack conditions.

To represent ground scattering from X-band, it is necessary to parameterize the soil status from a dielectric properties perspective. One way of achieving this is to make use of the Oh model (Oh *et al.*, 1992). Designed for use over bare agricultural soils (Oh *et al.*, 1992), the Oh model has not been evaluated for organic soil conditions, conditions which predominate in sub-Arctic and southern Arctic environments (French, 2007; Tarnocai, 2009). If future snow monitoring missions suggest use of the Oh model within their modelling frameworks, ensuring the model operates correctly under soil conditions of Arctic and sub-Arctic regions will be of critical importance. Such understanding will be necessary for future snow remote sensing missions to improve the characterization of snow across large remote regions, such as the Canadian Arctic and sub-Arctic.

In order to evaluate the potential use of the Oh model within SWE algorithms for future snow monitoring missions, this thesis aims to evaluate the application of the Oh model under organic soil conditions of the Hudson Bay Lowlands (HBL) region of the Canadian

sub-Arctic. Through this research, the Oh model's ability to represent ground backscatter from organic sub-Arctic terrain will be evaluated, providing insight into the appropriateness of the model's use for radar-based dual-frequency SWE retrievals from sub-Arctic areas.

1.1 Objectives

To evaluate the Oh model for soil conditions of the HBL region within the context of X-band radar measurements, three main objectives are defined:

1. Parametrizing the Oh model to allow for representation of organic sub-Arctic soil.
2. Evaluating ground-based and spaceborne X-band returns from the HBL region and subsequently, the degree to which the Oh model can represent these returns.
3. Determining the appropriateness of Oh model application within a radar focused SWE retrieval algorithm for the organic soil environment of the HBL.

For the first objective, ensuring parameters used within the Oh model are appropriate for representation of HBL soil will be required to allow for proper evaluation of Oh model operation under organic soil conditions. Values required for this parametrization will be obtained through field measurements where available, as well as through model estimates when appropriate. Parameter values not contained within the validated range of the Oh model will allow for expanded model evaluation through Objective 2.

For the second objective, X-band measurements obtained during the winter of 2010-2011 from a ground-based scatterometer (King *et al.*, 2013) and the TerraSAR-X satellite will be used to evaluate Oh model estimates of HBL soil backscatter. This time series validation approach will allow for a thorough evaluation of Oh model operation under varying snow and soil conditions in the HBL region, conditions which are applicable over large parts of Arctic and sub-Arctic tundra regions.

For the final objective, the representative capacity of the Oh model for ground-based and spaceborne X-band measurements explored through Objective 2 will lead to an indication of the Oh model's appropriateness for potential SWE retrieval algorithms for the HBL region. Based on the nature of Objective 2 results, recommendations regarding the implementation of the Oh model within the future SWE retrieval algorithms will be offered.

Through these objectives, the applicability of the Oh model for ground scattering representation of organic soils within potential SWE retrieval algorithms will be evaluated. While results will only be applicable to specific soil conditions examined within the HBL study area, they will nevertheless present insight into the capability of an existing approach for representing ground scatter from organic soil environments.

1.2 Thesis Structure

To facilitate full understanding of the presented research, this thesis is separated into addition chapters for each main project step. Chapter 2 outlines motivations for this research, including a discussion of active microwave remote sensing of snow along with an examination of the role of soil state in remote sensing observations of snow. In Chapter 3 the HBL study site is introduced, providing a description of the location from which field measurements were obtained. Chapter 4 outlines the research methodology, including descriptions of the Oh model, the data used to parametrize the model, as well as the process used to evaluate the model's appropriateness for the study site. Results and discussion are presented in Chapter 5 with a focus on the Oh model's representative capacity for the HBL study site as well as its suitability within SWE retrieval algorithms. The thesis concludes in Chapter 6 with a summary of presented results and discussion.

Chapter 2

Active Microwave Remote Sensing of Snow Covered Landscapes

This chapter provides background information regarding active microwave remote sensing of snow to inform the reader of motivations for this research. The chapter begins with a review of active microwave remote sensing principles. This is followed by an examination of factors which influence remote sensing of snow at X-band, from the perspective of the active microwave instrument and snowpack under observation. The chapter concludes with a review of the previous sections to outline the main motivation for this research.

2.1 The Active Microwave Process

Microwave remote sensing uses wavelengths within the microwave portion of the electromagnetic spectrum to interpret characteristics of surface features. Active microwave sensors utilize an on-board energy source to illuminate Earth's surface instead of capturing Earth's emitted microwave energy. Active microwave sensors typically operate with frequencies between 0.25 to 40 GHz[1]. (wavelengths of 120 to 0.75 cm) (Moreira *et al.*, 2013), due to the ability of these waves to travel through the atmosphere with minimal interaction. This presents a substantial advantage for microwave frequencies as they can obtain information about the terrestrial surface under almost all atmospheric conditions, including cloud cover, rainfall and darkness (Richards, 2009).

[1]This frequency range covers P- (0.25-0.5 GHz), L- (1-2 GHz), S- (2-3.75 GHz), C- (3.75-7.5 GHz), X- (7.5-12 GHz), Ku- (12-17.6) and Ka- (25-40 GHz) bands. L- C- and X-bands represent the most commonly used frequencies (Moreira *et al.*, 2013)

The majority of active microwave sensors operate using a *monostatic* configuration, wherein the same antenna is used to transmit and receive a microwave signal (Richards, 2009). The nature of this transmit and receive process defines the active microwave measurement which is made. Prior to investigating how characteristics of the sensing wave and target of interest influence active microwave measurements, it is useful to understand the theoretical measurement process of a single target. To begin, we can visualize the sensor as radiating a microwave frequency uniformly in all directions. With this configuration, the signal will achieve a *power density* (p_i) incident at the target, which is a distance of R away (metres in this case). This p_i, measured in watts per square metre (Wm^{-2}) is defined through the equation (Richards, 2009):

$$p_i = \frac{P_t}{4\pi R^2} \ \mathrm{Wm}^{-2} \tag{2.1}$$

where P_t is the *transmitted power* measured in watts. With an active microwave instrument, the use of an antenna to direct P_t alters the concentration of power at the target. This modifies (2.1) to become (Richards, 2009):

$$p_i = \frac{P_t G_t}{4\pi R^2} \ \mathrm{Wm}^{-2} \tag{2.2}$$

where G_t represents the *gain* of the transmitting antenna. Gain represents a ratio of the p_i of the signal as an isotropic radiator (as in (2.1)) versus its p_i generated in a specific direction through an antenna (Richards, 2009).

From (2.2) we have a representation of the energy incident at the target. In order to determine the actual amount of received power which is available for scattering by the target, we must consider its dimensions, defined by its Radar Cross Section (RCS). The RCS, represented mathematically as σ, describes the area of the target in square metres. It is assumed that the target scatters the incident signal isotropically within the area of its RCS (Richards, 2009). By accounting for the target's RCS, the amount of incident energy available for scattering (P_σ) is defined as (Richards, 2009):

$$P_\sigma = p_i \sigma = \frac{P_t G_t \sigma}{4\pi R^2} \ \mathrm{W} \tag{2.3}$$

The scattering of the signal produces a *power density at the sensor* (p_r) defined as (Richards, 2009):

$$p_r = \frac{P_t G_t \sigma}{(4\pi)^2 R^4} \text{ Wm}^{-2} \tag{2.4}$$

The presence of the additional $4\pi R^2$ term in (2.4) relates to the assumed isotropic scattering of the signal from the target (Richards, 2009). As the portion of the sensor sensitive to the scattered signal, its *aperture* (A_r), contains a given area, the *actual power* of the signal received by the antenna (P_r) is calculated through (Richards, 2009):

$$P_r = \frac{P_t G_t \sigma A_r}{(4\pi)^2 R^4} \text{ W} \tag{2.5}$$

The aperture of an antenna is normally used to describe its behaviour only for the received signal. To generalize (2.5) for signal reception and transmission, we can represent the aperture of the antenna in terms of its gain (G_r) through (Richards, 2009):

$$G_r = \frac{4\pi}{\lambda^2} A_r \tag{2.6}$$

This translates (2.5) into (Richards, 2009):

$$P_r = \frac{P_t G_t G_r \lambda^2 \sigma}{(4\pi)^3 R^4} \text{ W} \tag{2.7}$$

It is important to remember that (2.7) represents the power returned from a theoretical, discrete target. In reality, most targets are formed of multiple features, making them *distributed* in nature. To modify (2.7) for distributed targets, the definition of RCS must be altered to account for targets of any size. This is done by representing the RCS in decibels (dB) using (Richards, 2009):

$$\sigma^o = 10\log\frac{\sigma}{\sigma_{ref}} \text{ dB} \tag{2.8}$$

where σ_{ref} is 1 m^2. This transitions (2.8) to units of dBm^2 (Richards, 2009). To account for the distributed nature of the target, we can consider the target to be formed of an infinite number of features, each of which contains a given area (ds). The RCS of each of these areas is defined as $d\sigma$. The average RCS per unit area of the target is therefore defined as $d\sigma/ds$. This average RCS for the target thus represents the *scattering coefficient* of the region and is denoted as σ^o. Through this modification of the RCS, we

can redefine (2.7) to represent the signal returned to the sensor based on the scattering coefficient for the target (dP_r) through (Richards, 2009):

$$dP_r = \frac{P_t G_t G r \lambda^2 \sigma^o ds}{(4\pi)^3 R^4} \text{ W} \tag{2.9}$$

To determine the power returned from a single pixel within the target, (2.9) is integrated over the area of the pixel through (Richards, 2009):

$$P_r = \iint\limits_{pixel} \frac{P_t G_t G_r \lambda^2 \sigma^o ds}{(4\pi)^3 R^4} \text{ W} \tag{2.10}$$

By assuming that all quantities within the integral are constant, the power received by the sensor is defined as (Richards, 2009):

$$P_r = \frac{P_t G_t G_r \lambda^2 \sigma^o r_a r_g}{(4\pi)^3 R^4} \text{ W} \tag{2.11}$$

where r_a and r_g represent *azimuth* and *range* resolutions respectively. (2.11) is termed the *radar equation* and is commonly used for active microwave scattering representation as most observed features represent distributed targets. To fully understand σ^o derived from the radar equation, it is necessary to determine how target and signal characteristics influence backscatter measurements. This is explored in Section 2.2 with respect to snow covered terrain.

2.2 Factors Affecting Active Microwave Remote Sensing of Snow-Covered Landscapes

To obtain useful information about Earth surface properties from active microwave measurements, knowledge of signal interaction characteristics of the target(s) of interest are required. These interaction characteristics are influenced by two sets of properties: those of the *target* and those of the sensing *signal*. As the influence of these properties depends on the type of active microwave signal used as well as the Earth surface feature under observation, we will explore these properties within the context of the completed research, namely X-band active microwave signals and snow covered sub-Arctic organic terrain.

2.2.1 Influence of Signal Properties

From the sensor perspective, three properties of the sensing wave present the greatest influence to signal scattering: *frequency*, *polarization*, and *incident angle*. Each presents varying influences to target interaction and are discussed in turn through the following sections.

Frequency

The frequency of an active microwave signal depends on its wavelength, which represents the average distance between consecutive minimum or maximum wave peaks. Frequency is defined by the number of wavelengths which pass a stationary point in a given amount of time. Thus an inverse relationship exists between frequency and wavelength, with shorter wavelengths representing higher frequencies (Jensen, 2007). X-band signals occupy a wavelength range of 2.4 to 3.75 cm, corresponding to frequencies of 12.5 to 8 GHz (Lillesand *et al.*, 2008). Frequency is important for understanding target interaction as it defines the degree to which the signal will be subject to interaction with a given surface. Generally, variation in the surface height of the target of interest must approach the wavelength of the sensing wave for diffuse scattering to occur[2].

With respect to snow, a signal's frequency presents a strong control over its ability to interact with the snowpack. At X-band, the wavelength range of 2.4 to 3.75 cm (Lillesand *et al.*, 2008) suggests that this frequency will only interact with snow when the variation in the surface height of the pack, controlled principally by *grain size* (see Section 2.2.2) and snow thickness, reaches wavelength size. Several studies have confirmed this theory, identifying a penetration depth for X-band of $\sim$10 m under dry snow conditions (Ulaby *et al.*, 1984; Mätzler, 1987; Rott *et al.*, 1993), essentially characterizing X-band as transparent to snow. Other properties of snow, discussed further in Section 2.2.2, can affect the penetration capabilities of incident microwave signals, but the level of this influence is controlled by the signal's frequency.

Polarization

The polarization of an active microwave signal refers to the direction of the geometric plane in which the electric field of the wave is oscillating (Lillesand *et al.*, 2008). The orientation of this plane relates to the antenna from which the signal was emitted.

[2]This concept is discussed further with surface roughness.

Signals which are polarized to oscillate parallel to the axis of the antenna are said to have *horizontal* polarization. If the oscillation is perpendicular to the antenna axis the polarization is termed *vertical* (Lillesand *et al.*, 2008). Active microwave sensors are capable of both producing and measuring polarized signals. To denote the polarization of the transmitted and received wave, the letters H and V, representing horizontal and vertical polarizations respectively, are combined to represent the four possible transmit and receive polarization combinations: HH, VV, HV, VH. The first letter indicates the polarization of the transmitted wave while the second letter identifies the received wave's polarization. The first two combinations, HH and VV, are termed *co-polarized* as their transmit and receive polarizations are the same. *Cross-polarized* represents HV and VH as their transmit and receive polarizations are opposite (Lillesand *et al.*, 2008). By measuring multiple polarizations, sensors can provide more information regarding the interaction characteristics between the signal and the target of interest, possibly allowing useful information from the target to be obtained (Lillesand *et al.*, 2008).

From a snow-covered terrain perspective, research has shown that polarization does not appear to have a significant influence over backscatter characteristics at X-band. Observations have shown preferential scattering with co-polarizations, with variation occurring with changing incident angles. Cross-polarized signals, while producing less scattering, generally retain consistent backscatter levels across varying incident angles (Ulaby *et al.*, 1986; King *et al.*, 2013). These characteristics tend to remain constant across snowpacks with varying physical properties, indicating that variations in backscatter magnitude are related to snow physical properties and other active microwave signal properties (e.g. frequency) rather than polarization (Ulaby *et al.*, 1986).

Incident Angle

Incident angle (or "incidence angle") refers to the angle created between the transmitted radar signal and a line normal to the Earth's surface at the point of signal interaction with the target (Lillesand *et al.*, 2008). Incident angles are generally referred to as *large* or *small*, with large angles being more parallel to the surface (further from the normal line) and smaller angles more perpendicular to the surface. In general, backscatter decreases with larger incident angles as the changing geometry alters the portion of the target available for signal interaction (Lillesand *et al.*, 2008).

With snow, the general influence of incident angle on backscatter remains consistent with smaller angles producing greater backscatter due to potential volume scattering within the snowpack (Ulaby *et al.*, 1986). Observations at X-band performed by Mätzler *et al.* (1997), Floricioiu & Rott (2001) and King *et al.* (2013) demonstrated consistency with

theory as the greater thickness of snow within the sensor's field of view at smaller incident angles increases volume scattering. Similar to polarization, other signal and snow properties present greater control over observed backscatter than polarization.

2.2.2 Influence of Surface Properties

The influence of surface properties on active microwave signals presents the greatest interest for research. Knowledge of how signals interact with surface features under different conditions enables an understanding of the information microwave signals can provide regarding the surface under observation. In this section known influences of snow covered terrain on active microwave signals are explored to provide an indication of what types of information we can expect to obtain from snow covered sub-Arctic landscapes. Focus is given to X-band to demonstrate the theoretical basis for this research. These influences originate from the two main components of snow covered terrain: the overlying *snow layer* and the *ground surface*. The *surface roughness* of the snow covered terrain, which includes components of the overlying snow and underlying ground, also influences signal interaction. Properties comprising these components are explored in turn to describe their effects on active microwave signals.

Surface Roughness

Surface roughness defines how the target under observation appears to the incident microwave signal. In general the target can be *smooth* or *rough*. Rough surfaces produce more backscatter as the scattering produced by them is more diffuse in nature (Lillesand *et al.*, 2008). The level of roughness for a given target is determined primarily by the frequency of the signal, its incident angle, as well as the target's properties. Two criteria exist for providing a mathematical basis for a target's surface roughness at microwave frequencies. The first, the *Rayleigh* criterion, functions through (Ulaby *et al.*, 1982):

$$\sigma = \frac{\lambda}{8\ \cos(\theta)} \tag{2.12}$$

where σ is the standard deviation of the surface height of the target, λ is the wavelength and θ is the incident angle. Essentially this equation states that if the standard deviation of the target's surface height is less than the wavelength of the incident signal divided by 8 times the cosine of its incident angle, the target is considered to be smooth for the given wavelength. If σ is greater than the surface may be considered rough (Ulaby *et al.*,

1982). While a beneficial criterion, Rayleigh is less useful for microwave frequencies where wavelengths are typically near σ of desired targets. As such a more stringent criterion, termed *Fraunhofer*, may be used (Ulaby *et al.*, 1982):

$$\sigma = \frac{\lambda}{32\ \cos(\theta)} \tag{2.13}$$

The Fraunhofer principle is thus the same as Rayleigh, only with a more strict definition of the ratio between λ and θ (Ulaby *et al.*, 1982).

With snow, surface roughness is controlled by physical properties of the pack, primarily its grain size. Alterations in the size of snow grains can increase the overall variation in the surface height of the pack, increasing the interaction potential of the snow to microwave signals. At X-band, the relatively large wavelength range of 2.4 to 3.75 cm thus requires fairly large grain sizes to produce interaction, leading to the substantial penetration levels observed in previous research (Ulaby *et al.*, 1984; Mätzler, 1987; Rott *et al.*, 1993). This effect is enhanced for spaceborne signals which tend to be influenced more by features below the snowpack (Baumgartner *et al.*, 2002). Thus the surface roughness of the ground below the snow should play a more substantial role in signal scattering from snow covered terrain at X-band.

Physical Properties of Snow

SWE: SWE represents a measure of the amount of water contained within a snowpack. It is based on the amount of water which would be produced from melting a given amount of snow within a given area (Goodison *et al.*, 1981). SWE depends on the *depth* and *density* of the snowpack, expressed through the relation (Speers *et al.*, 1996):

$$SWE\ (\text{mm}) = Depth\ (\text{m}) * Density\ (\text{kg m}^{-3}) \tag{2.14}$$

Thus changes in either parameter affect a snowpack's SWE.

With respect to active microwave backscatter, research has focused principally on the influence of snow depth. This work has produced conflicting results, with some indicating potential interaction at X-band frequencies and others suggesting X-band is insensitive to snow depth. Two studies, Ulaby & Stiles (1980) and Kendra *et al.* (1998), demonstrated the potential influence of artificially altered snow depth on X-band signals. Within each, the depth of snow was gradually increased with X-band scans of the surface performed at

each depth interval. Depths of 120 and 170 cm were reached in Ulaby & Stiles (1980) and Kendra *et al.* (1998) respectively. With each experiment, X-band backscatter was found to increase slightly with increasing depth, with change occurring within depths of up to ∼70 cm. Within Ulaby & Stiles (1980), this corresponded to a range of SWE from 0 to 30 cm. Shi *et al.* (1993) also demonstrated X-band sensitivity to snow depth (63 cm); however this result was based purely on a modelled result.

In contrast, investigations by Mätzler *et al.* (1982), Mätzler & Schanda (1984) and Floricioiu & Rott (2001) have found limited sensitivity of snow depth on X-band signals. Each of these experiments were conducted in natural alpine settings in the presence of fairly deep snowpacks (up to 1 m depth). In all cases measurements acquired over the snow covered terrain exhibited similar backscatter response to snow free conditions (Mätzler & Schanda, 1984; Floricioiu & Rott, 2001). Results from King *et al.* (2013) also illustrate limited X-band response to snow under the sub-Arctic tundra snow conditions explored within this research.

It has been suggested that the observed sensitivity to snow depth at X-band in Ulaby & Stiles (1980) was caused by the use of artificially piled snow as this produced a snow volume that was not representative of naturally accumulated snow (Mätzler & Schanda, 1984). Kendra *et al.* (1998) indicate density and grain sizes (0.48 g/cm^3 and 0.27 mm respectively) of the packed snow utilized in their experiment approach levels which are rare in nature, again indicating a limitation in applying the observations to real world conditions. Nevertheless, while uncommon, these experiments suggest that X-band can demonstrate sensitivity to snow depth, and thus SWE, under the correct conditions.

Grain Size: After being deposited on the surface, snow crystals gradually transform as influences of atmospheric conditions and further falling snow alter their characteristics. Under cold conditions, the crystals evolve into highly faceted grains of ice. With warmer conditions, the faceted grains become more rounded. With warm and cold conditions possible within a pack simultaneously, coupled with the influence of further snow deposition, a snowpack can contain grains of many shapes and sizes (Langham, 1981; Colbeck, 1982). One type of grain, termed *depth hoar*, is of particular concern for active microwave remote sensing. Depth hoar occurs when strong temperature gradients develop in the snowpack due to warm conditions near the bottom of the pack and cold temperatures at the air-snow interface. Under these circumstances water vapor at the bottom of the pack travels upward toward the cooler snow surface. As the vapor rises it cools, condenses, and eventually crystallizes. Through further introduction of water vapour, the depth hoar layer takes shape, consisting of many complex, layered crystals (Langham, 1981). If depth hoar grains approach the size of microwave wavelengths they can influence backscatter.

Snow grains can influence active microwave backscatter only if their size is sufficient to generate signal interaction, or if their structure is sufficiently dense to facilitate scattering (Mätzler, 1987; Tse *et al.*, 2007). Yueh *et al.* (2009) identified increases in Ku-band backscatter through larger grain sizes present within a depth hoar layer of a mature snowpack. At X-band, larger grains than those identified in Yueh *et al.* (2009) would be required to achieve a similar result, but through a full winter of grain metamorphism this may be possible. In instances where smaller grain sizes have been observed (Bernier & Fortin, 1998; Kendra *et al.*, 1998), other snow properties control the level of backscatter originating from the snowpack.

Complex Relative Permittivity: The Relative Complex Permittivity[3] (ϵ_r) of a material represents a characterization of its electrical properties. It is a measurement of the material's ability to store an electric charge relative to a vacuum (Hallikainen & Winebrenner, 1992; Etzold, 2008). Mathematically this is defined as a complex number through (The Institute of Electrical and Electronics Engineers, 1997):

$$\epsilon_r = \epsilon_r^{'} - j\epsilon_r^{''} \tag{2.15}$$

where $\epsilon_r^{'}$ and $\epsilon_r^{''}$ represent the real and imaginary portions of ϵ_r respectively and $j = \sqrt{-1}$ (Hallikainen & Winebrenner, 1992; The Institute of Electrical and Electronics Engineers, 1997). Note that $\epsilon_r^{'}$ represents the material's electrical storage capacity relative to that of a vacuum while $\epsilon_r^{''}$ represents the electrical loss of the material (i.e. the amount of energy which is lost to the material) (Hallikainen & Winebrenner, 1992). Note that ϵ_r differs from permittivity as ϵ_r has been normalized to the *free space permittivity* (ϵ_0)[4] (The Institute of Electrical and Electronics Engineers, 1997).

Within snow, ϵ_r is controlled principally by three components: *air*, *ice*, and *liquid water* (Hallikainen *et al.*, 1986; Mätzler, 1987). The nature of these components within a given snowpack are controlled by other factors such as temperature and density, allowing ϵ_r to change throughout the winter as metamorphism alters the snow. Liquid water presents the greatest control as water exerts a substantial influence over a material's ability to conduct electricity. With liquid water and ice having very different ϵ_r characteristics ($\epsilon_r^{'} \approx 80$ and 3.15 respectively), changes in the proportion of liquid water and ice

[3]Relative Complex Permittivity is commonly referred to as Dielectric Constant in literature. While analogous terms, dielectric constant is now considered to be depreciated (The Institute of Electrical and Electronics Engineers, 1997).

[4]ϵ_0 is a scalar constant which ensures that the product of ϵ_0 and the electric field being applied is equal to the *electric flux density* (i.e. the charge displaced within the medium by an electric field). The constant value for ϵ_0 is $8.854{*}10^{-12}$F/m (The Institute of Electrical and Electronics Engineers, 1997).

contained within a snowpack will have a substantial impact on its ϵ_r (Colbeck, 1982; Scherer *et al.*, 2005). The ϵ_r of air is assumed to be identical to that of a vacuum, thus allowing higher levels of air within a snowpack to reduce its ϵ_r (Mätzler, 1987). With increasing density and grain size caused by snow metamorphism, the presence of air within the pack is reduced accordingly, thus limiting the effect of air on ϵ_r over time and increasing the ϵ_r of the snow (Cumming, 1952; Hallikainen *et al.*, 1986).

Changes in snow ϵ_r can have a substantial impact on backscatter. With dry snow, both $\epsilon_r^{'}$ and $\epsilon_r^{''}$ remain low, allowing active microwave signals to penetrate the snow surface and thus interact with the snow volume and ground surface (Hallikainen *et al.*, 1986). In such instances snow properties such as grain size and depth will control the backscatter response in accordance with the frequency of the incident wave. With wet snow, $\epsilon_r^{''}$ increases substantially, causing its absorption coefficient to rise as well. This severely limits the penetration capabilities of active microwave frequencies, causing any scattering to be controlled by the snow's surface roughness instead of its volume components (Hallikainen & Winebrenner, 1992; Scherer *et al.*, 2005). Measurements completed under wet snow conditions have illustrated marked reductions in backscatter at a variety of frequencies, including X-band (Stiles & Ulaby, 1980; Bernier & Fortin, 1991).

Ground Surface Properties

While the physical properties of snow can influence active microwave backscatter, they only do so if their characteristics allow for interaction with the incident wave. If interaction is not supported at the snow surface or within its volume, the last potential area for interaction lies at the ground surface. Ground properties which influence backscatter are similar to those for snow and operate in similar fashion. However, in most cases properties at the surface of the ground are of greatest interest as the limited penetration depth of most microwave frequencies limits potential soil volume scattering (Ulaby *et al.*, 1982). While the lowest frequencies can achieve substantial soil penetration (i.e. $\sim$1 m at 1.3 GHz), penetration capabilities of higher frequencies are on the order of centimetres (e.g. $\sim$5 cm at 10 GHz). Penetration is reduced further when the soil is wet ($<$1 cm at 10 GHz with 0.4 g cm^{-3} volumetric water content) (Ulaby *et al.*, 1982).

Soil ϵ_r impacts backscatter through changes in soil moisture and temperature (Hoekstra & Delaney, 1974; Ulaby *et al.*, 1986). Measurements of soil ϵ_r under frozen and thawed conditions reveal substantial reductions in ϵ_r when the soil is frozen as the transition of moisture to ice reduces ϵ_r (Hoekstra & Delaney, 1974; Hallikainen *et al.*, 1984, 1985; Wegmüller, 1990). In turn this causes reduced backscatter from frozen soil (Wegmüller, 1990; Bernier & Fortin, 1991). Similar to snow, the introduction of water into the soil

(i.e. soil moisture) increases its ϵ_r. However, unlike snow, higher water content in soil increases backscatter through increased *reflectivity* (Ulaby *et al.*, 1986; Wegmüller, 1990). Reflectivity determines the portion of the incident wave's power which is reflected back by the surface (Ulaby *et al.*, 1996). Thus with increased reflectivity and ϵ_r caused by higher moisture levels in soil, backscatter increases accordingly.

Soil surface roughness also exerts an important control over backscatter. Soils containing rougher surfaces for the incident wavelength generate higher backscatter as the potential for diffuse scattering is higher than for smooth surfaces (Ulaby *et al.*, 1982). Soil type can also influence backscatter, particularly through the size of grains contained within the soil (Dobson & Ulaby, 1981; Ulaby *et al.*, 1986). As the size of grains determines the availability of empty space within the soil medium, this also controls the potential for free water within the soil. Water molecules within soil may be either bound to soil particles or present within the space between grains (i.e. free) (Ulaby *et al.*, 1978). The ϵ_r of bound water molecules can be much lower than that of free water (Grim, 1953), thus allowing soils containing larger grains and ample empty space (e.g. sandy soils) to generate higher backscatter than smaller grained soils (e.g. clay soils) (Ulaby *et al.*, 1978, 1986).

2.2.3 Summary

Overall, the process of obtaining useful information from any feature observed through active microwave measurements requires an understanding of how characteristics of the sensing wave and feature(s) under observation influence the backscattered signal. With regards to snow, three signal properties (i.e. frequency, polarization and incident angle) control the degree to which an active microwave signal will interact with a given snowpack. Properties of the snow-covered terrain under observation, including surface roughness, SWE, grain size and ϵ_r, as well as characteristics of the ground beneath the snow layer, also influence backscatter received by a remote sensing instrument.

At X-band, previous research has generally indicated limited sensitivity to snow under dry snow conditions. In such instances X-band backscatter from snow will thus be most indicative of conditions below the snow, with control exerted by characteristics of the ground surface. Interaction within snow is achieved most easily through increases in liquid water content, which greatly increases snow ϵ_r. Increases in snow density and grain size can also cause X-band interaction within a snowpack, but this has not been observed with characteristics which are common for natural snowpacks. Based on this understanding, X-band backscatter from the dry, shallow snowpacks which characterize much of the Canadian sub-Arctic should be mostly representative of ground beneath the

snow. Therefore, this research focuses on the interaction of X-band signals with sub-nivean organic soils of the HBL.

2.3 Research Motivation: Understanding and Quantifying X-band Response from a Cold Season Tundra Landscape

From our understanding of the factors which contribute to active microwave remote sensing of snow, the motivation for this research can be framed. This motivation has centred on the proposed Cold Regions Hydrology High-Resolution Observatory ($CoReH_2O$) mission, which aimed to improve the measurement of both the extent and water equivalent of snow on a global scale (Rott *et al.*, 2010). $CoReH_2O$ was to implement a dual-frequency and dual-polarization approach for snow monitoring, utilizing both Ku- (17.2 GHz) and X-band (9.6 GHz) frequencies as well as VV and VH polarizations (Rott *et al.*, 2010). The dual-frequency approach is considered to be important due to the differing sensitivities of Ku- and X-band to snow properties. Ku-band measurements provide backscatter sensitivity to the snow volume as a result of sensitivity to snow properties. In contrast, X-band will primarily provide information regarding the ground surface owing to its limited sensitivity to snow properties. In mountainous regions where snow depth and grain size can increase substantially through significant snow accumulation, X-band is expected to provide measurements of the snow volume when these snow properties achieve sufficient size to produce X-band interaction. X-band measurements will therefore supplement Ku-band observations, which tend to demonstrate less sensitivity to snow at high SWE levels (European Space Agency, 2012). As previous work examining X-band interaction with snow covered sub-Arctic terrain has been limited, the exact behaviour of X-band signals within this environment is uncertain. This research will attempt to improve this understanding and look to inform the frameworks of future snow remote sensing missions, such as that previously proposed through $CoReH_2O$.

To obtain measurements of snow extent and SWE, a model, termed Semi-Empirical Radiative Transfer Model (sRT), has been developed. This model represents a semi-empirical forward model (s) based on the radiative transfer (RT) approach developed by Ulaby *et al.* (1984) (Heidinger *et al.*, 2010). To represent scattering from the ground surface below the snow, sRT utilizes the Oh model (Oh *et al.*, 1992; Heidinger *et al.*, 2010). The Oh model was originally developed to represent backscatter from bare

agricultural soil for a variety of active microwave frequencies (Oh *et al.*, 1992). As X-band returns from the majority of snow conditions will be representative of the ground surface, the Oh model should provide an appropriate representation of the observed backscatter. However, this will require the Oh model to properly represent the scattering characteristics of soils under conditions at the time of Ku- and X-band measurements, namely soils which are frozen and covered with snow.

As the Oh model has not been validated for use under winter soil conditions, an opportunity exists to explore its wider applicability. Ensuring the model will operate correctly under winter soil conditions is also critical to ensure correct snow information is obtained from a combined Ku- and X-band retrieval approach. As snow retrievals will likely focus on Arctic and sub-Arctic regions, the Oh model must be tested to ensure compatibility with soil types of these areas. Organic soils comprise a substantial component of Arctic and sub-Arctic regions and contain characteristics which differ greatly from agricultural soils. Therefore, three objectives can be identified for this research:

1. Evaluating Oh model performance under sub-Arctic organic soil conditions.
2. Evaluating Oh model performance under thawed and frozen soil conditions.
3. Evaluating Oh model performance under snow covered terrain conditions.

Through this research, the capability of the Oh model for representing X-band returns from snow-covered sub-Arctic terrain within the HBL region of Canada will be identified. This research will also extend our understanding of active microwave remote sensing of snow to sub-Arctic snow and ground characteristics which have not comprised a significant quantity of existing literature.

Chapter 3

Research Study Site

In this chapter an overview of the HBL study site used within this research is presented. It contains a description of the geography of the study site, including the specific site location as well as its land cover and climate characteristics.

3.1 Site Location

The study site is located ∼23 km east of Churchill, Manitoba, Canada (Figure 3.1). Churchill, as well as the surrounding area, is contained within the HBL physiographic region, a vast wetlands complex located in the northernmost regions of Ontario and Manitoba, as well as the eastern portion of Nunavut. This area is considered to contain the highest concentration of wetlands in North America (Abraham & Keddy, 2005). Due to its significant geographic coverage, land cover characteristics of the HBL vary substantially, from mud flats and intertidal marshes present along the shoreline of Hudson Bay to fens, peatlands and small lakes located further inland (Mitsch & Gosselink, 2007). The area surrounding Churchill is dominated by flat terrain with relief generated by glacial deposits. The area contains three ecological regions, including tundra, forest-tundra and open forest (Lafleur *et al.*, 1997; Duguay *et al.*, 2002), leading to varied terrain from the coast southwards. Shallow lakes are prominent, occupying up to 32% of the landscape in some areas (Lafleur *et al.*, 1997; Duguay *et al.*, 2002). Soils in the region typically consist of peat overlying marine silts and clays. The thickness of peat ranges from 10 to 50 cm, with the deepest peat layers occurring at greater distances from the coast (Duguay *et al.*, 2002).

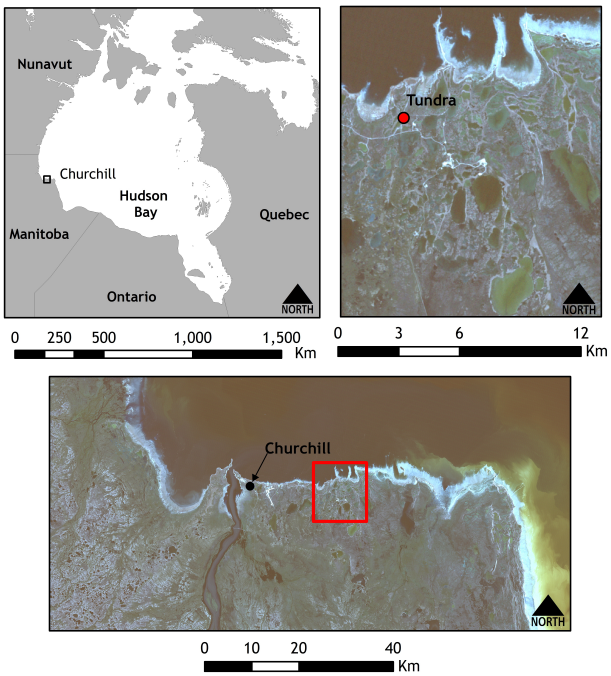
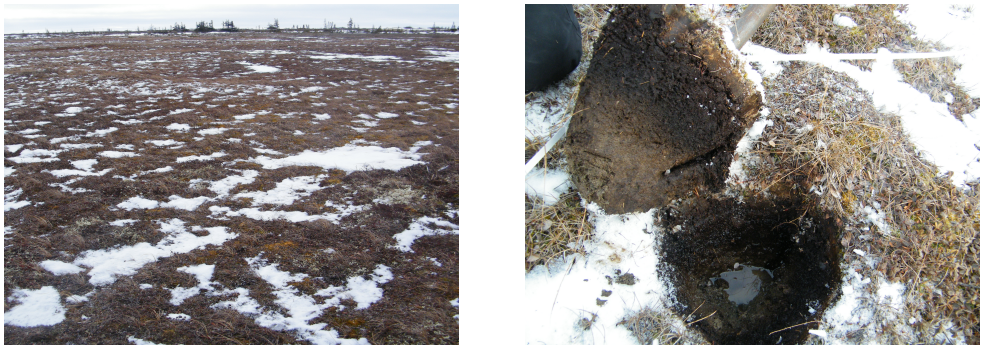


Figure 3.1: Location of study site. Top Left: Location of Churchill in relation to four Canadian Provinces (adapted from Duguay *et al.* (2002)). Top Right: Location of tundra study site. Bottom: Study area (square) in relation to Churchill. Imagery represents a Landsat 5 Thematic Mapper scene acquired on September 4, 2010 (National Aeronautics and Space Administration, 2010). Canadian Provinces shapefile acquired from the Atlas of Canada (Atlas of Canada, 2009).

3.2 Climate

The climate of the Churchill area is characterized by cold winters and cool summers. In comparison to other areas of the HBL, those surrounding Churchill typically experience cooler temperatures and drier conditions (Abraham & Keddy, 2005). The average annual air temperature for Churchill is -7.2°C with the coldest and warmest conditions occurring in January and July respectively, with average temperatures of -27.5 and 11.8°C for each month. Only during the short summer (June to September) are average temperatures above freezing. Average annual precipitation is 411 mm, of which almost half (43%) occurs as snow during the winter months (October to May) (Duguay *et al.*, 2002).



(a) (b)

Figure 3.2: The tundra study site (a) and its soil characteristics (b) in October 2010. Note the hummocky nature of the terrain as well as high soil moisture.

3.3 Specific Site Characteristics

The study site consists of tundra terrain located within close proximity of Hudson Bay (Figure 3.1). Terrain was relatively flat, with the exception of small hummocks (∼1 m in size) distributed throughout the site (Figure 3.2a). Vegetation consisted predominantly of grasses, with some shrubs and isolated trees occurring periodically. Soil characteristics consisted of peat containing a high soil moisture content (Figure 3.2b). Although measurements of soil moisture were not preformed, it is estimated that the soil contained a high level of moisture throughout the field measurement period, mostly in a frozen state.

The site was exposed to a range of weather conditions throughout the measurement period (October 2010 to May 2011). *In situ* measurements of air temperature, soil surface temperature and wind speed (Figure 3.3) were obtained from a meteorological station approximately 200 m to the south of the study site[1]. Air temperatures ranged from 12° to -34°C with an average of -14°C. Soil surface temperatures exhibited a reduced range, from 6.8° to -19.7°C with an average of -9.4°C. Wind conditions at the site were strong, with an average wind speed of 5.1 m/s^{-1}. The highest measured wind speed was 14.9 m/s^{-1}. Average snow depth at the study site was 15.1 cm, varying from 6.5 to 23 cm across a transect of the site. Due to the high wind speed, snow depth was minimized as fresh snow was readily transferred to reduced wind regions. The wind also

[1]The author would like to thank Peter Kershaw for providing access to meteorological station measurements.

produced a wind slab layer which persisted across much of the site. Throughout the measurement period snow grain size also increased, ranging from sizes less than 0.5 mm near the start of the campaign to 4.8 mm upon measurement completion. Grain sizes were highest within a depth hoar layer which developed soon after the onset of snowfall.

3.4 Summary

Overall, the research site provides a representation of HBL sub-Arctic conditions, with a prevalence of organic (peat) soil, cool climate conditions and intermediate precipitation levels. Terrain conditions at the site represent a tundra landscape, with a grassy, hummocky relief interspersed with few shrubs and trees. Soil moisture conditions at the site were high throughout the study period. In comparison to previous investigations of X-band behaviour over snow covered terrain, this site presents a substantial contrast to typical agricultural soil conditions, enabling results of this research to further our understanding of active microwave interaction.

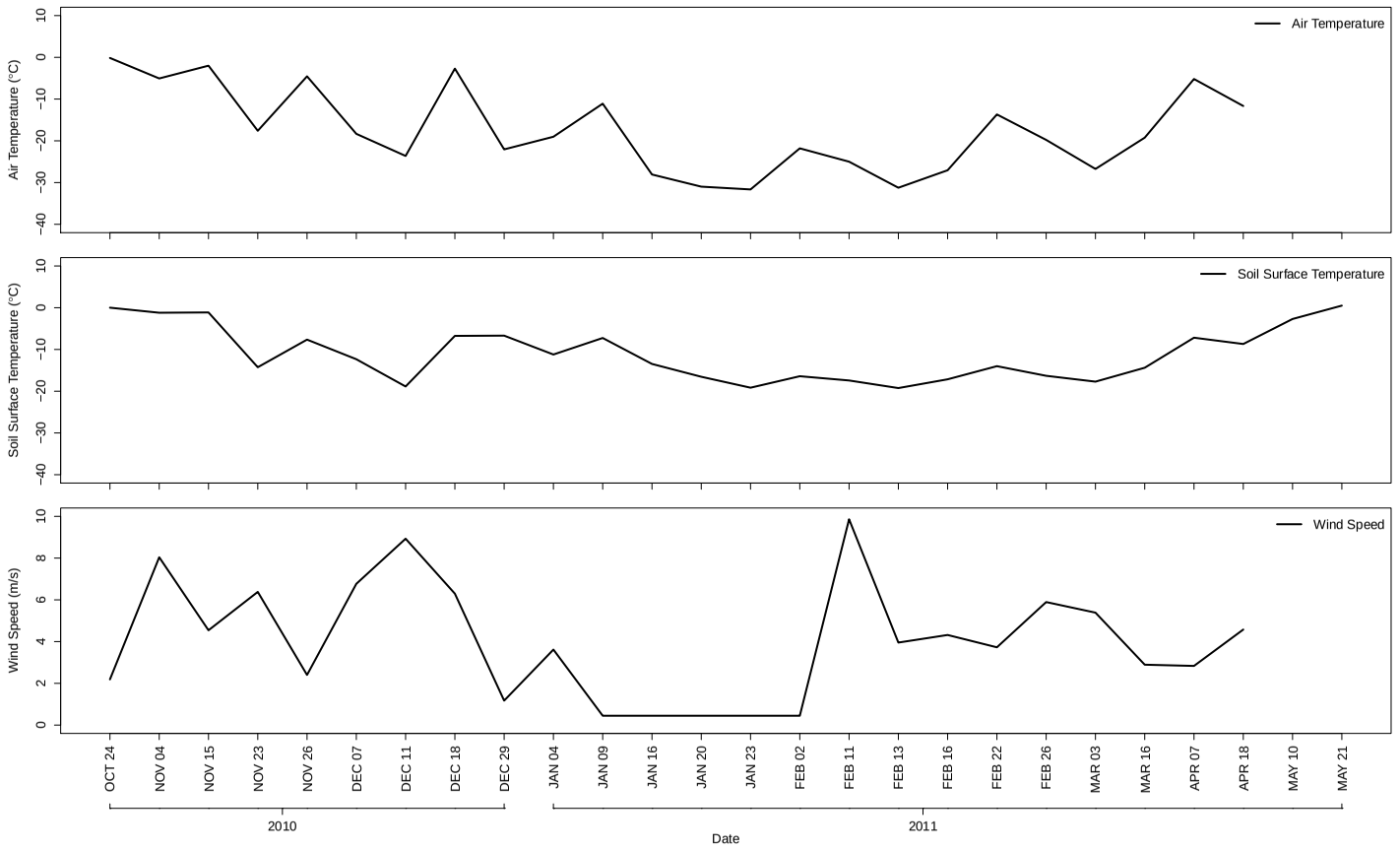


Figure 3.3: Measurements of air temperature (top), soil surface temperature (middle) and wind speed (bottom) throughout the study period. Measurements were acquired from a meteorological station ∼200 m south of the study site. Air temperature and wind speed was measured 1.5 m above ground level. Air temperature and wind speed was not measured on May 10^{th} and 21^{st} 2011.

Chapter 4

Methodology

This chapter presents an overview of the experimental methodology used within this research. To begin, an overview of the experiment framework is presented to outline the measurements and models used within this work as well as the analysis process. This is followed by detailed descriptions of the measurements and models to ensure familiarity with the instruments and processes which were utilized. A detailed description of the analysis follows, and the chapter is concluded with a summary of the complete experiment.

4.1 Overview

The primary goal of this research is to evaluate the proposed use of the Oh model within SWE retrieval algorithms based on soil conditions of the HBL study site. To achieve this, three components are required: 1) *remote sensing measurements*; 2) *models*; 3) *field measurements* and 4) *laboratory measurements*.

Remote Sensing Measurements: Two sets of remotely sensed data were utilized within this experiment; one representing measurements obtained from a ground-based scatterometer and the other representing acquisitions from the TerraSAR-X satellite. These measurements form the dataset with which Oh model output was compared. The use of *in situ* and satellite measurements for comparison provides the opportunity to extend Oh model evaluation to both ground-based and spaceborne projects for which it may be applied.

Models: Two models were required for this research; the Oh model (Oh *et al.*, 1992), for the representation of soil scattering, and a ϵ_r model, the Temperature-Dependable Generalized Refractive Mixing Dielectric Model (TD GRMDM) (Mironov *et al.*, 2010). TD GRMDM was used to supply estimates of organic soil ϵ_r, which were required by the Oh model. Implementation of both models was completed using the R statistical language (R Development Core Team, 2011). Each implementation was tested by replicating results presented in Oh *et al.* (1992) and Mironov *et al.* (2010) to ensure accuracy.

Field Measurements: Parametrization of the Oh model required soil surface roughness measurements. As these were not obtained in conjunction with remote sensing measurements, surface roughness sampling of the study site was completed in February 2012. These measurements were used within the Oh model to allow for a more accurate representation of study site conditions within the comparison of model estimated and remotely sensed X-band backscatter. Figure 4.1 illustrates the approximate location where field measurements were acquired at the study site, in relation to the position of UW-Scat and the meteorological station where *in situ* weather conditions were monitored.

Laboratory Measurements: To ensure correct use of TD GRMDM, laboratory measurements completed on a sample of peat obtained from the study site were required. These measurements allowed for an evaluation of the model's representative capacity for the soil conditions of the study site.

Through an evaluation of the TD GRMDM and Oh models based on the conditions of the study site as well as through comparisons with the remotely sensed measurements, the appropriateness of these models for use within the sub-Arctic environment of the Churchill region is identified. Within the results, focus is given to the Oh model due to its forecasted use within future dual-frequency SWE retrieval missions.

4.2 Remote Sensing Measurements

4.2.1 Ground-Based Scatterometer

Ground-based scatterometer observations of the study site were obtained using the University of Waterloo Scatterometer (UW-Scat) a dual-polarization frequency modulated continuous wave radar instrument (Figure 4.2). UW-Scat operated at centre frequencies of 9.6 GHz (X-band) and 17.2 GHz (Ku-band), and allowed measurements to be obtained from a range of elevation angles (21 to 81° in 3° increments) (King *et al.*,

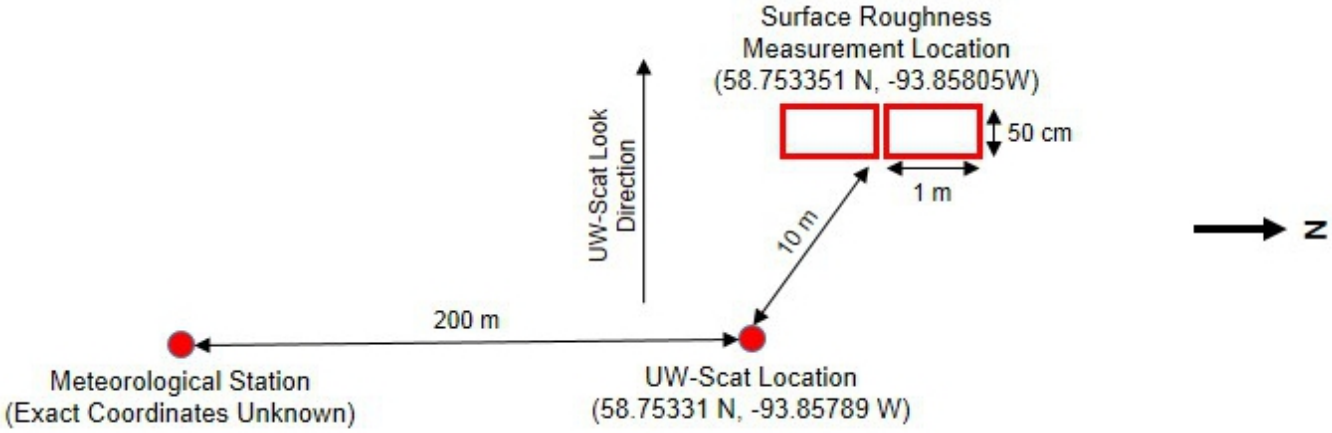


Figure 4.1: Approximate position of field measurements location in relation to UW-Scat sensor position. Roughness measurement location coordinates indicates midpoint between measurement locations. Meteorological station location is also illustrated. Peat sample obtained for laboratory measurements was acquired near UW-Scat's position, but exact coordinates are unknown. Note that the map is not to scale and distances are approximate.

2013). For this research, X-band measurements acquired with co- and cross-polarizations of HH, VV and HV at an elevation of 45° were utilized.

UW-Scat measurements were acquired using a consistent protocol throughout the study period. Conditions at the site were left unaltered within UW-Scat's field of view, allowing measurements to be obtained from naturally accumulated snow. Measurements were also obtained from bare ground prior to the onset of snow cover. Measurements of snow conditions (i.e. depth, density, grain size and SWE) were obtained during each acquisition outside of UW-Scat's field of view[1]. This allowed approximate snow conditions of the UW-Scat measurement site to be obtained without disturbing the natural evolution of the area. At the end of the measurement campaign, an excavation procedure was initiated at the site. This began with a final scan of the undisturbed ground. Then, snow measurements within UW-Scat's field of view were obtained to quantify snow conditions of the measurement site. Finally, the snow was removed from the measurement site and a scan of the uncovered ground was completed (King *et al.*, 2013). This process allowed any influence of snow on the UW-Scat signal to be described. A total of 13 UW-Scat measurements were completed at the study site during the campaign (Table 4.1).

[1]Summaries for a portion of these measurements are presented in Section 3.3

Table 4.1: UW-Scat and TerraSAR-X acquisition dates for the study site. Dates are in YYYY/MM/DD format. Times are also shown for TerraSAR-X acquisitions in CST and CDT where appropriate. All TerraSAR-X images were acquired at 23:56 UTC from an ascending orbit.

UW-Scat	TerraSAR-X	
Date	Date	Time (CST/CDT)
	2010/10/24	18:56
2010/11/04	2010/11/04	18:56
2010/11/15	2010/11/15	17:56
2010/11/23	2010/11/26	17:56
2010/12/11	2010/12/07	17:56
2011/12/18	2010/12/18	17:56
	2010/12/29	17:56
2011/01/04	2011/01/09	17:56
2011/01/16	2011/01/20	17:56
2011/01/23		
2011/02/02	2011/02/11	17:56
2011/02/13	2011/02/22	17:56
2011/02/16		
2011/02/26		
2011/03/03	2011/03/16	18:56
	2011/04/07	18:56
	2011/04/08	18:56
	2011/05/10	18:56
	2011/05/21	18:56

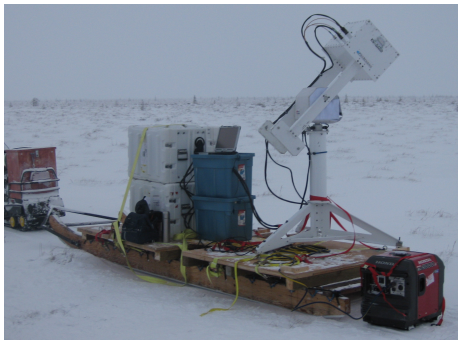


Figure 4.2: Set-up of UW-Scat. Instrument was transported by snowmobile to the study site. Separate instrument heads for X- and Ku-bands were used. UW-Scat is shown with Ku-band head attached.

4.2.2 TerraSAR-X

The TerraSAR-X satellite operates at an X-band frequency of 9.65 GHz and is capable of providing global coverage every 11 days (Infoterra GmbH, 2009). Sixteen images acquired at VV and VH polarizations were obtained throughout the measurement period (Table 4.1). Each image contained a swath size of ∼15 km by 50 km and a raw resolution of 1.72 m (Figure 4.3). Due to the size of the image swath, each acquisition contained a range of incident angles from 43 to 44°.

Processing

All images were acquired through TerraSAR-X's SSC format, which represents a Single Look Complex product. To obtain analysis-ready data, each image went through a five step processing work flow. All processing was completed using Version 4.0 of European Space Agency (ESA) Next ESA Synthetic Aperture Radar Toolbox (NEST) software. For each step, NEST's default parameters were utilized unless otherwise indicated. Descriptions of each processing step are as follows:

1. *Multilooking*: Multilooking provided an initial smoothing of the imagery through a reduction of its grainy texture. Two range and four azimuth looks were used for multilooking.

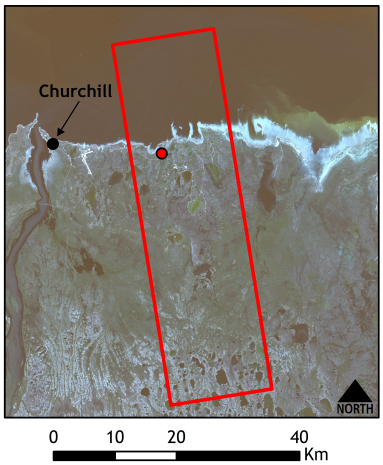


Figure 4.3: TerraSAR-X acquisitions footprint (red box). Study site location indicated by red dot. Imagery represents a Landsat 5 Thematic Mapper colour composite acquired on September 4, 2010 (National Aeronautics and Space Administration, 2010).

2. *Slant Range to Ground Range Conversion*: TerraSAR-X's SSC image format provides data in slant range format. A linear interpolation method with a warp polynomial order of four was used to convert the imagery to ground range format.

3. *Radiometric Correction*: Application of radiometric correction removed sensor induced noise from the imagery in addition to converting the raw digital numbers to decibel (dB) format.

4. *Reprojection*: Raw TerraSAR-X imagery was present in a mirrored format, causing latitude and longitude values of each image to be incorrect. Reprojection transformed the imagery to correct geographic coordinates based on the World Geodetic System 1984 geodetic datum.

5. *Filtering*: Additional filtering was applied to remove excess speckle remaining after multilook processing. After experimentation with several of NEST's available filters, a 2x2 Lee filter was selected based on its ability to reduce speckle while retaining a maximum amount of information. Application of the multilook and filtering procedures degraded spatial resolution to $\sim$5 m.

Application of this processing yielded geometrically correct TerraSAR-X imagery suitable for analysis (Figure 4.4). For comparisons with Oh model output, TerraSAR-X

data was extracted from a 3x3 window (i.e. ∼15 m x 15 m) centred at the middle of the study site, using PCI Geomatics software. This produced nine pixel values which were averaged to create one backscatter value for each acquisition. This window method was used to capture a greater proportion of the variation of the terrain which would influence backscatter, in addition to approximating the area viewed by UW-Scat. As well, the influence of any residual pixel values was diminished through this process.

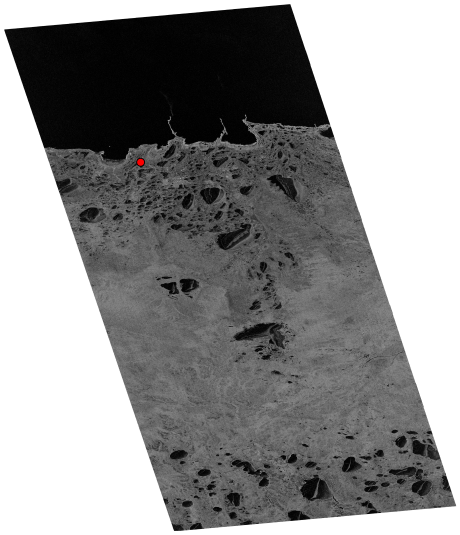


Figure 4.4: A processed TerraSAR-X image acquired on October 24, 2010. Red dot indicates study site location.

4.3 Models

4.3.1 Oh Model

The Oh model presents a framework for representing active microwave scattering from bare soil surfaces (Oh *et al.*, 1992). This model has been explored for implementation within the Cold Regions Hydrology High-Resolution Observatory ($CoReH_2O$) framework. The model was originally designed as an integrated approach for representing backscatter for a variety of active microwave frequencies (i.e. 1.25, 4.75 and 9.5 GHz), polarizations (i.e. HH, VV and HV) and surface roughness conditions (i.e. 0.32 to 3.02 cm) (Oh *et al.*, 1992). Prior to its development, three separate models, namely the Small Perturbation

Method (SPM), the Physical Optics Model (PO) and the Geometric Optics Model (GO), were required to achieve the same representation of the above frequencies, polarizations and surface roughness conditions as provided by the Oh model (Oh *et al.*, 1992). Due to this multi-frequency, polarization and roughness representation capability, the Oh model has become popular for bare soil active microwave applications.

The approach developed by Oh *et al.* (1992) consists of both an forward and inverse model. The inverse model allows for the estimation of soil moisture and roughness levels from input active microwave observations while the forward model provides backscatter estimates based on measured soil ϵ_r and roughness. As this research focuses on backscatter comparisons, only the forward model is described here.

The basis of the model is formed through two terms: ks , which represents the surface roughness of the soil in terms of the *wavenumber*[2] (k) of the desired microwave frequency as well as the Root Mean Square (RMS) height of the soil surface (s). k is calculated using (Oh *et al.*, 1992):

$$k = 2\pi/\lambda \tag{4.1}$$

where λ is the wavelength of the desired frequency in centimetres. The second term consists of the Relative Complex Permittivity[3] (ϵ_r) of the soil surface.

Using these terms, Oh *et al.* (1992) developed five equations to represent HH, VV and HV backscatter (σ^o) returns. The first two equations represent the *cross-* and *co-polarized ratios* respectively for the three investigated polarizations. They form the basis for the three final equations which produce σ^o estimates for the three polarizations. The cross-polarized ratio (q) (i.e $\sigma^o_{hv}/\sigma^o_{vv}$) is represented by (Oh *et al.*, 1992):

$$q \triangleq \frac{\sigma^o_{hv}}{\sigma^o_{vv}} = 0.23\sqrt{\Gamma_o}[1 - exp(-ks)] \tag{4.2}$$

where Γ_o represents the *Fresnel Reflectivity* of the surface at a nadir incident angle. The Γ_o of a surface relates to the Fresnel Equations which predict the transmission and reflection characteristics of light passing from one medium to another (Mack, 2006), in essence defining the portion of incident energy which will be reflected from the medium and the portion which will be transmitted through it. In the Oh model, Γ_o is determined from the soil's ϵ_r through (Oh *et al.*, 1992):

[2]Wavenumber represents the reciprocal of a given wavelength (Lakowicz, 2006).

[3]See Section 2.2.2 for a detailed discussion of ϵ_r

$$\Gamma_o = \left| \frac{1 - \sqrt{\epsilon_r}}{1 + \sqrt{\epsilon_r}} \right|^2 \tag{4.3}$$

By calculating Γ_o as part of q, the authors were able to develop a co-polarized ratio (p) for the available polarizations (i.e. $\sigma^o_{hh}/\sigma^o_{vv}$), illustrated through (Oh *et al.*, 1992):

$$\sqrt{p} = \sqrt{\frac{\sigma^o_{hh}}{\sigma^o_{vv}}} = 1 - \left(\frac{2\theta}{\pi}\right)^{\left[\frac{1}{3\Gamma_o}\right]} exp(-ks) \tag{4.4}$$

where θ is the incidence angle in radians.

Based on the cross- and co-polarized ratios illustrated through Equations 4.2 and 4.4, separate equations to derive σ^o for the VV, HH and HV polarizations were developed. The calculation for VV, for a given θ, ϵ_r and ks is shown through (Oh *et al.*, 1992):

$$\sigma^o_{vv}(\theta, \epsilon_r, ks) = \frac{g cos^3\theta}{\sqrt{p}} [\Gamma_v(\theta) + \Gamma_h(\theta)] \tag{4.5}$$

where Γ_v and Γ_h represent the Fresnel Reflectivities for the vertical and horizontal polarizations respectively for the given θ and p is given by Equation 4.4. g is represented through (Oh *et al.*, 1992):

$$g = 0.7[1 - exp(-0.65(ks)^{1.8})] \tag{4.6}$$

The remaining calculations for σ^o_{hh} and σ^o_{hv} are represented through (Oh *et al.*, 1992):

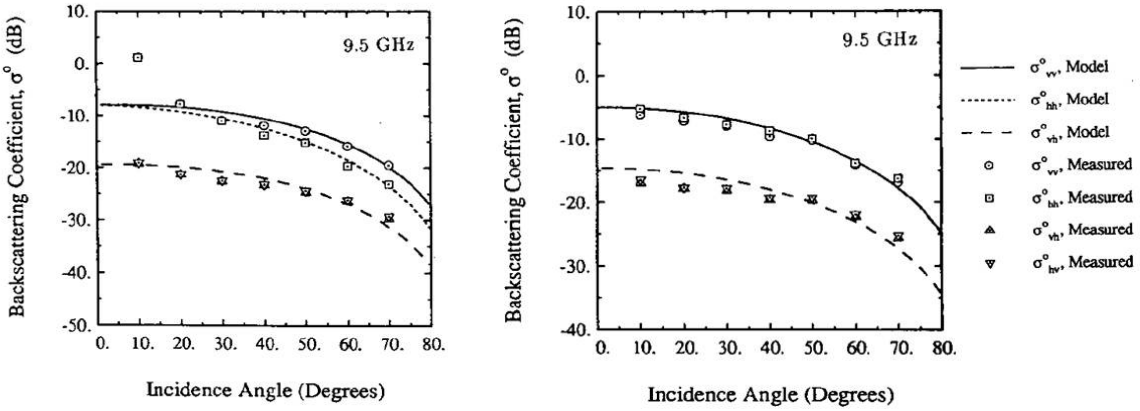
$$\sigma^o_{hh}(\theta, \epsilon_r, ks) = g\sqrt{p} cos^3\theta [\Gamma_v(\theta) + \Gamma_h(\theta)] \tag{4.7}$$

and

$$\sigma^o_{hv}(\theta, \epsilon_r, ks) = q\sigma^o_{vv}(\theta, \epsilon_r, ks) \tag{4.8}$$

respectively.

To evaluate the empirical model, *in situ* measurements were performed at four agricultural fields, each of which contained different s levels (i.e. from 0.32 to 3.02 cm). Sampling was completed under wet and dry conditions, leading to volumetric moisture



(a) (b)

Figure 4.5: Comparison of Oh empirical model output with X-band scatterometer measurements for the wet cases of fields one (a) and four (b). Fields one and four contained s values of 0.40 and 3.02 cm respectively as well as soil moisture levels of 0.29 and 0.19 cm^3 cm^{-3} respectively (Oh *et al.*, 1992). Note that the legend is the same for both graphs.

levels from 0.09 to 0.30 cm^3 cm^{-3}. Such variation led to ϵ_r values from 4.26, 0.76 to 13.14, 3.85 ($\epsilon_r^{'}, \epsilon_r^{''}$) at X-band. Ground-based scatterometer measurements were performed at θ's from 10 to 70° at 10° intervals (Oh *et al.*, 1992). Figure 4.5 illustrates the ability of the model to represent the scatterometer measurements for two of the investigated soils. The soils for Figure 4.5a and 4.5b contained s values of 0.40 and 3.02 cm respectively and surface soil moisture levels of 0.29 and 0.19 cm^3 cm^{-3} respectively. The results demonstrate the ability of the model to operate correctly at both the high and low soil moisture and surface roughness levels examined during the experiment, indicating its potential for representing σ^o for a variety of soil moisture and roughness conditions.

While the results illustrated through Figure 4.5 demonstrate the potential of the Oh model for representing σ^o from soil, there are two limitations which question the ability of the model to operate correctly under situations not examined within the experiment. For one, the model was developed and evaluated for σ^o occurring from bare agricultural soils. As soil characteristics vary widely, the suitability of the model for representing σ^o from non-agricultural soil types (e.g. organic soils) is unknown. Secondly, the model was only validated for a maximum volumetric soil moisture level of 0.30 cm^3 cm^{-3}. Certain soils, such as organics, likely contain greater soil moisture levels during the year. While the Oh model may be able to operate correctly under saturated soil conditions, this has

not been demonstrated through existing evaluation.

These limitations may restrict the use of the Oh model within a dual Ku- and X-band retrieval framework. As a global Ku- and X-band satellite mission would inevitably capture significant quantities of data from tundra soils, expanding the evaluated range of the Oh model to organic tundra soils under high moisture conditions is critical to demonstrate the appropriateness of the model. These limitations form the basis of the experiment completed as part of this study.

4.3.2 Temperature-Dependable Generalized Refractive Mixing Dielectric Model (TD GRMDM)

From Section 4.3.1, we see that three parameters are required for the Oh model, namely soil s and ϵ_r, as well as the θ of the incident active microwave signal. Within this research, θ values are supplied by UW-Scat and TerraSAR-X acquisitions. Soil s measurements completed in February 2012 fulfill the s parameter (see Section 4.4). As *in situ* measurements of ϵ_r were not completed at the study site, estimates of this parameter are required. This was achieved through TD GRMDM (Mironov *et al.*, 2010), which currently represents the only representation of ϵ_r for organic Arctic soils. Note that as laboratory measurements of ϵ_r were completed on a sample of peat obtained from the study site[4], TD GRMDM estimates of ϵ_r were not required. However, by exploring the application of TD GRMDM within the Oh model and for the representation of HBL soil ϵ_r, the use of TD GRMDM within applications involving organic sub-Arctic soils without available *in situ* ϵ_r could be evaluated, providing benefit to future projects.

Prior to the development of TD GRMDM, previous undertakings for soil ϵ_r representation focused almost exclusively on agricultural soils under thawed conditions (e.g. Hallikainen *et al.* (1985)). Some authors explored effects of freezing on soil ϵ_r within their representations (e.g. Wang & Schmugge (1980)); however, none of these approaches could be deemed appropriate for application in Arctic regions due to differences in Arctic and temperate soil characteristics (Mironov *et al.*, 2010).

Through their approach, Mironov *et al.* (2010) identified five components of Arctic organic soil which comprise its Complex Refractive Index (CRI): 1) *solid content*, which represents non-liquid components; 2) *bound water*, which represents liquid water that is bound to solid materials in the soil; 3) *unbound water*, which represents water not bound to soil materials; 4) *transient bound water*, which represents a type of liquid water within

[4]See Section 4.5.

frozen soil which behaves differently than liquid water under thawed conditions, and 5) *moistened ice water*, which represents liquid water bound to ice particles within frozen soil (Mironov *et al.*, 2010). Components 2 and 3 are termed *soil water conditions* as they represent water within the soil. The CRI represents the complex form of the soil's Refractive Index (RI). In general, the RI provides a measure of the degree to which a ray of light bends when interacting with different mediums (Encyclopædia Britannica, 2013). With respect to active microwave remote sensing, this bending relates to signal scattering. The complex form of RI allows energy stored within the medium to be accounted for (Fox, 2001), which in this case represents signal absorption by soil. This is defined by the imaginary component of CRI, which is termed the Normalized Attenuation Coefficient (NAC). The ϵ_r of a soil can be determined through a volume-weighted average of its CRI; thus developing a model to represent an Arctic soil's CRI also allows its ϵ_r to be determined (Mironov *et al.*, 2010).

The model was developed through investigation of a soil sample collected from the Alaska North Slope during the summer of 2004. The sample was collected from a depth of 20 cm within relatively dry terrain which supported substantial shrub growth. The sample was composed primarily of organic matter (80-90%), with five minerals comprising the remaining components (i.e. Quartz [7.5-8.2%], Tiff [4-5%], Mica [0.75-1.5%], Plagioclase [0.75%] and Smectite [0.75])[5]. With the high organic content, the soil's bulk density was low (0.254 g/cm^3). To measure the soil's ϵ_r for a variety of moisture and temperature conditions, the sample was dried for 24 hours in a 104°C oven and then weighed. Predetermined amounts of water were added to the dried sample to achieve a desired moisture content. Gravimetric moistures from 0.05 to 1.1 g/g were utilized. For each moisture level, the sample's ϵ_r was measured at frequencies from 1.0-16 GHz using a Rohde & Schwarz ZVK network analyzer. Measurements were made in 5°C intervals from -30 to 25°C, allowing for numerous samples from frozen and thawed conditions. The authors estimate relative errors within the CRI at 1 and 6% for real and imaginary components respectively, with absolute errors for these components of 0.04 and 0.006 respectively (Mironov *et al.*, 2010).

TD GRMDM consists of a seven step process: 1) assigning a temperature and determining if the soil is frozen or thawed; 2) calculating low and high frequency ϵ_r limits, as well as relaxation time and conductivity for each soil water condition; 3) determining $\epsilon_r^{'}$ and $\epsilon_r^{''}$ for each soil water condition as a function of frequency at the defined temperature; 4) translating ϵ_r into RI and NAC for all soil water conditions; 5) assigning a gravimetric soil moisture and calculating the Maximum Gravimetric Fraction of Bound Water (MGFBW) and the Maximum Gravimetric Fraction of Unfrozen

[5]Totals do not add to 100% due to rounding.

Water (MGFUW); 6) assigning soil bulk density and determining the complete soil CRI, and 7) translating the soil CRI value into ϵ_r. The following sections outline each of these steps in detail. Note that while primary development of TD GRMDM was published in Mironov *et al.* (2010), updates to the model were presented in Mironov & Savin (2010). Instances where updates from Mironov & Savin (2010) supersede original published work are indicated.

Step 1: Assigning Temperature and Soil State - Soil temperature is important to consider within ϵ_r as the presence of ice at freezing temperatures greatly alters the nature of ϵ_r in comparison to temperatures above freezing[6]. The soil analyses conducted within Mironov *et al.* (2010) revealed that the majority of liquid water transitioned to ice between temperatures of -7 and -5°C. As such, a temperature of -6°C is assigned as a threshold between frozen and thawed soil.

The identification of the soil as being either frozen or thawed plays an important role in subsequent modeling steps in two ways. Firstly, the presence of specific soil water conditions depends directly on soil state. Within thawed soil, TD GRMDM accounts for bound, unbound and transient water. With frozen soil, the model accounts for bound, transient and moistened ice water conditions as the presence of ice enables the development of moistened ice water but prevents the presence of unbound water. Bound and transient water are often present together as not all liquid water attached to solid soil materials freezes at sub-zero temperatures. Secondly, temperature-dependant model coefficients must be adjusted based on soil state (Mironov *et al.*, 2010). In the following steps, instances where these two factors are present will be identified to demonstrate the model's differences for frozen and thawed soils.

Step 2: Calculating ϵ_r Limits, Relaxation Time and Conductivity - ϵ_r limits refer to ϵ_r values which would theoretically occur if the material was exposed to an electric field with very low or high frequencies. The *low frequency limit* represents the ϵ_r which would occur if the material was exposed to an electric field with a frequency of 0 Hz. In contrast *high frequency limit* represents the ϵ_r which would occur if the material was exposed to an electric field with an infinite frequency (Bartnikas, 1997). As each of these limits can only occur in theoretical terms, they present the upper and lower ϵ_r limits for a given medium. In TD GRMDM, low and high frequency ϵ_r limits are calculated for each soil water condition using (Mironov *et al.*, 2010):

$$\epsilon_{qp}(T) = \frac{1 + 2exp[F_{qp}(Ts\epsilon qp) - \beta_{vqp}(T - T_{s\epsilon qp})]}{1 - exp[F_{qp}(T_{s\epsilon qp}) - \beta(T - T_{s\epsilon qp})]} \tag{4.9}$$

[6]See Section 2.2.2.

where ϵ_{qp} represents the low ($q = 0$) or high ($q = \infty$) frequency ϵ_r limit for one of the soil water conditions (p) (i.e. bound [$p = b$], unbound [$p = u$], transient [$p = t$] or moistened ice water [$p = iw$]) for a given temperature (T) in °C; F_{qp} represents low and high frequency ϵ_r limits for one of the soil water conditions for a starting temperature ($T_{s\epsilon qp}$), and β_{vqp} represents the volumetric expansion coefficient for low and high frequency ϵ_r limits for each p. Table 4.2 contains coefficients for β_{vqp} and $T_{s\epsilon qp}$, as well as ϵ_{qp} when $T = T_{s\epsilon qp}$ (Mironov *et al.*, 2010). F_{qp} is calculated through (Mironov *et al.*, 2010):

$$F_{qp}(T) = \ln\left[\frac{\epsilon_{qp}(T) - 1}{\epsilon_{qp}(T) + 2}\right] \tag{4.10}$$

where ln is the natural logarithm. To obtain F_{qp} for low and high frequency limits, ϵ_{qp} values for $T_{s\epsilon qp}$ are used. The result is then utilized within Equation 4.9 through $F_{qp}(T_{s\epsilon qp})$ to allow the determination of ϵ_{qp} at any temperature (Mironov *et al.*, 2010).

Relaxation time refers to the frequency at which $\epsilon_r^{''}$ will peak for a given material (Bartnikas, 1997). In TD GRMDM, relaxation time is calculated as a function of temperature as a material's temperature will influence the frequency at which $\epsilon_r^{''}$ will peak. In general, higher temperatures will cause the relaxation time to occur at lower frequencies (Bartnikas, 1997). TD GRMDM relaxation time is calculated through (Mironov *et al.*, 2010):

$$\tau_p(ps) = \frac{48}{T_K} exp\left[\frac{\Delta H_p}{R}\frac{1}{T_K} - \frac{\Delta S_p}{R}\right] \tag{4.11}$$

where $\tau_p(ps)$ is the relaxation time for a given p; T_K is the soil temperature in K; ΔH_p is the activation energy of the relaxation process; R is the universal gas constant ($8.314 \times 10^3 J.K^{-1}$) and ΔS_p is the entropy of activation. Table 4.3 provides constants for the $\Delta H_p/R$ and $\Delta S_p/R$ ratios for all soil water conditions for frozen and thawed soils. Equation 4.11 thus allows the relaxation time to be calculated for all soil water conditions at any temperature.

Conductivity describes the movement of electricity through a material. In general materials can facilitate conduction (high conductivity) or resist it (low conductivity) (Yoshino, 2011). As conductivity is influenced by temperature, TD GRMDM takes soil temperature into account when calculating conductivity through (Mironov *et al.*, 2010):

$$\sigma_p(T) = \sigma_p(T_{s\sigma p}) + \beta_{\sigma p}(T - T_{s\sigma p}) \tag{4.12}$$

Table 4.2: Coefficients for use within TD GRMDM Equations 4.9 and 4.10 for low and high frequency limits and all soil water conditions. T_f represents the soil's freezing temperature (i.e. -6°C) (Mironov *et al.*, 2010). Note that some coefficients were updated within a subsequent version of the model (Mironov & Savin, 2010). These coefficients are indicated with an asterisk (*).

Parameter	Units	Bound Water		Unbound Water
p	(subscript)	b		u
Temperature Range		$T < T_f$	$T > T_f$	$T > T_f$
$\epsilon_{0p}(T_{s\epsilon 0p})$	-	8.19	13.66	83.53*
β_{v0p}	1/K	-4.8×10^{-3}	-2.87×10^{-3}	$+7.6 \times 10^{-5}$*
$T_{s\epsilon 0p}$	°C	-30	0	+20
$\epsilon_{\infty p}(T_{s\epsilon\infty p})$	-	5.92	9.29	10.76*
$\beta_{v\infty p}$	1/K	-4.37×10^{-3}	-4.0×10^{-3}	-3.51×10^{-3}
$T_{s\epsilon\infty p}$	°C	-20	+20	+25*
Parameter	Units	Transient Water		Moistened Ice Water
p	(subscript)	t		iw
Temperature Range		$T < T_f$	$T > T_f$	$T < T_f$
$\epsilon_{0p}(T_{s\epsilon 0p})$	-	24	87.01*	5.57
β_{v0p}	1/K	-5.62×10^{-3}	-1.27×10^{-4}*	-5.93×10^{-3}
$T_{s\epsilon 0p}$	°C	-20	+20*	-20
$\epsilon_{\infty p}(T_{s\epsilon\infty p})$	-	5.05	20.4*	4.07
$\beta_{v\infty p}$	1/K	0	-1.66×10^{-5}*	-2.4×10^{-3}
$T_{s\epsilon\infty p}$	°C	-20	+20*	-20

Table 4.3: Constants for $\Delta H_p/R$ and $\Delta S_p/R$ ratios for all soil water conditions (Mironov *et al.*, 2010). Note that some coefficients were updated within a subsequent version of the model (Mironov & Savin, 2010). These coefficients are indicated with an asterisk (*).

Parameter	Units	Bound Water		Unbound Water
p	(subscript)	b		u
Temperature Range		$T < T_f$	$T > T_f$	$T > T_f$
$\Delta H_p/R$	K	1540	1540	1884*
$\Delta S_p/R$	-	0.1	0.1	2.23*
Parameter	Units	Transient Water		Moistened Ice Water
p	(subscript)	t		iw
Temperature Range		$T < T_f$	$T > T_f$	$T < T_f$
$\Delta H_p/R$	K	1493	2004*	1352
$\Delta S_p/R$	-	0.45	1.8*	0.39

where $\sigma_p(T)$ is the conductivity at a given T for a given p; $T_s\sigma p$ is an initial temperature value used to calibrate conductivity estimates for a given p, and $\beta_{\sigma p}$ is the derivative of conductivity for a given p. Table 4.4 provides constants for $T_{s\sigma p}$ and $\beta_{\sigma p}$ as well as $\sigma_p T_{s\sigma p}$, the conductivity for a given p at the initial temperature. Equation 4.12 thus allows the conductivity for all soil water conditions to be calculated for any temperature.

Step 3: Calculating ϵ_r for Soil Water Conditions - With low and high frequency limits, relaxation times and conductivities calculated for each appropriate p given the soil T, the frequency dependence of each p can be calculated as a function of frequency and T through (Mironov *et al.*, 2010):

$$\left(n_p^*\right)^2 = \epsilon_{\infty p} + \frac{\epsilon_{0p} - \epsilon_{\infty p}}{1 - i2\pi f \tau_p} + \frac{i\sigma_p}{2\pi f \epsilon_0} \tag{4.13}$$

where n_p^* is the complex frequency dependence of a given p; $\epsilon_{\infty p}$ is the high frequency limit for the given p (from Equation 4.9); ϵ_{0p} is the low frequency limit for the given p (from Equation 4.9); f is the frequency in GHz; τ_p is the relaxation time for the given p (from Equation 4.11); σ_p is the conductivity for the given p (from Equation 4.12), and ϵ_0 is the vacuum permittivity (8.854 pF/m). For this research, the centre frequencies of UW-Scat and TerraSAR-X were used for f to produce TD GRMDM estimates for the their respective Oh model comparisons. The result of Equation 4.13 can be converted into $\epsilon_r^{'}$ through (Mironov *et al.*, 2010):

Table 4.4: Constants for $\sigma_p T_{s\sigma p}$, $\beta_{\sigma p}$ and $T_{s\sigma p}$ for all soil water conditions (Mironov *et al.*, 2010). Note that some coefficients were updated within a subsequent version of the model (Mironov & Savin, 2010). These coefficients are indicated with an asterisk (*).

Parameter	Units	Bound Water		Unbound Water
p	(subscript)	b		u
Temperature Range		$T < T_f$	$T > T_f$	$T > T_f$
$\sigma_p(T_{s\sigma p})$	S/m	0.07	0.23	0.95*
$\beta_{\sigma p}$	(S/M)/K	$+3.37 \times 10^{-3}$	$+3.76 \times 10^{-3}$	$+3.52 \times 10^{-3}$*
$T_{s\sigma p}$	°C	-20	+20	+20*
Parameter	Units	Transient Water		Moistened Ice Water
p	(subscript)	t		iw
Temperature Range		$T < T_f$	$T > T_f$	$T < T_f$
$\sigma_p(T_{s\sigma p})$	S/m	1.0*	1.35*	0.077
$\beta_{\sigma p}$	(S/M)/K	3.37×10^{-3}*	$+5.11 \times 10^{-3}$	$+0.69 \times 10^{-3}$
$T_{s\sigma p}$	°C	-20*	+20*	-20

$$\epsilon_p^{'} = n_p^2 - \kappa_p^2 \tag{4.14}$$

as well as $\epsilon_r^{''}$ through:

$$\epsilon_p^{''} = 2 n_p \kappa_p \tag{4.15}$$

where n_p and κ_p are the real and imaginary portions respectively of the complex frequency dependence of a given p (from Equation 4.13).

Step 4: Converting ϵ_r to RI and NAC for each p - As the main goal of TD GRMDM is to calculate the CRI for Arctic soils, ϵ_r for each p calculated through Equations 4.14 and 4.15 has to be converted into RI and NAC through Equations 4.16 and 4.17 respectively (Mironov *et al.*, 2010):

$$n_p(f,T) = \frac{1}{\sqrt{2}} \sqrt{\sqrt{\epsilon_p^{'2}(f,T) + \epsilon_p^{''2}(f,T)} + \epsilon_p^{'}(f,T)} \tag{4.16}$$

$$\kappa_p(f,T) = \frac{1}{\sqrt{2}} \sqrt{\sqrt{\epsilon_p^{'2}(f,T) + \epsilon_p^{''2}(f,T)} - \epsilon_p^{'}(f,T)} \tag{4.17}$$

where $n_p(f,T)$ and $\kappa_p(f,T)$ are the RI and NAC respectively for a given p, dependent on f and T.

Step 5: Assigning Soil Moisture Values - With RI and NAC values calculated for appropriate soil water conditions, TD GRMDM can now take soil moisture considerations into account. This starts by specifying the soil's gravimetric soil moisture (m_g) content. TD GRMDM was tested with m_g values from 0.05 to 1.1 g/g during its development (Mironov *et al.*, 2010). m_g values used within this research are defined in Section 4.6.1.

In addition to m_g, MGFBW and MGFUW require specification (Mironov *et al.*, 2010). MGFBW represents the highest proportion of bound water which can occur within a soil containing a given m_g. MGFUW represents a transition moisture level which separates the range of transient water from moistened ice water (Mironov & Savin, 2011). Under thawed conditions, MGFBW (m_{g1}) is calculated through (Mironov & Savin, 2010)[7]:

$$m_{g1}\ (\text{g/g}) = 0.258 - 0.0003(T) \tag{4.18}$$

Under frozen conditions, MGFBW (m_{g1}) is calculated through (Mironov *et al.*, 2010):

$$m_{g1}\ (\text{g/g}) = 0.164 + 0.0462exp\left(\frac{T}{13.441}\right) \tag{4.19}$$

MGFUW (m_{g2}) is calculated through Equations 4.20 and 4.21 under thawed and frozen conditions respectively[8] (Mironov & Savin, 2010; Mironov *et al.*, 2010):

$$m_{g2}\ (\text{g/g}) = 0.418 - 0.0008(T) \tag{4.20}$$

$$m_{g2}\ (\text{g/g}) = 0.35 + 0.757exp\left(\frac{T}{3.311}\right) \tag{4.21}$$

Steps 6 & 7: Assigning Dry Soil Bulk Density, Calculating Soil RI and NAC and Determining Soil ϵ_r - Development of TD GRMDM revealed the influence of bulk soil density (p_d) on soil CRI. Thus p_d must be assigned. In Mironov *et al.* (2010), p_d was measured as 0.254 g/cm^3. p_d values used within this research are defined in Section 4.6.1.

With the definition of p_d as well as m_g, MGFBW and MGFUW (if appropriate), RI and NAC for the complete soil can be calculated. This process takes into account RI and

[7]Note that this equation was updated within Mironov & Savin (2010).

[8]MGFUW was not calculated under thawed soil conditions in Mironov *et al.* (2010).

NAC values for all p, as well as p_d and moisture values to produce a single soil CRI. To begin, we must calculate RI and NAC for soil solids, the non-liquid components of the soil which have not been taken into account through previous steps. Under thawed conditions, RI and NAC of the soil solids are determined through Equations 4.22 and 4.23 respectively (Mironov *et al.*, 2010):

$$\frac{(n_m - 1)}{\rho_m} \text{ cm}^3/\text{g} = 0.52181 - 0.221T \tag{4.22}$$

$$\frac{\kappa_m}{\rho_m} \text{ cm}^3/\text{g} = 0.00684 - 0.000048T \tag{4.23}$$

where $\frac{(n_m-1)}{\rho_m}$ and $\frac{\kappa_m}{\rho_m}$ represent the RI and NAC for the soil soilds (m) respectively as a function of density (ρ). Equations 4.24 and 4.25 are utilized for frozen conditions (Mironov *et al.*, 2010):

$$\frac{(n_m - 1)}{\rho_m} \text{ cm}^3/\text{g} = 0.58806 - 0.000432T \tag{4.24}$$

$$\frac{\kappa_m}{\rho_m} \text{ cm}^3/\text{g} = 0.00752 - 0.000038T \tag{4.25}$$

The soil solids RI and NAC can then be combined with soil water RI and NAC, as well as moisture values to produce a single soil CRI. For thawed soil, Equation 4.26 is applied (Mironov & Savin, 2010)[9]:

$$\begin{aligned}\frac{n_s^* - 1}{\rho_d(m_g)} = &\frac{(n_m^* - 1)}{\rho_m} \\ &+ \frac{(n_b^* - 1)}{\rho_b}[m_g + ((m_{g1} - m_g)u(m_g - m_{g1}))] \\ &+ \frac{(n_t^* - 1)}{\rho_t}[(m_g - m_{g1})u(m_g - m_{g1}) + (m_{g2} - m_g)u(m_g - m_{g2})] \\ &+ \frac{(n_u^* - 1)}{\rho_u}(m_g - m_{g1})u(m_g - m_{g1})\end{aligned} \tag{4.26}$$

[9]In Mironov *et al.* (2010), the RI and NAC values for transient soil water (t) are not included in this equation.

where $\frac{n_s^*-1}{\rho_d(m_g)}$ is the soil CRI; $\frac{(n_m^*-1)}{\rho_m}$ is the RI for soil solids (from Equation 4.22); n_t^* is the CRI for transient soil water (from Equations 4.16 and 4.17); n_b^* is the CRI for bound water (from Equations 4.16 and 4.17); ρ_b is the density of bound water (1 g/cm^3); n_u^* is the CRI for unbound water (from Equations 4.16 and 4.17); ρ_u is the density of unbound water (1 g/cm^3), and u is the Heaviside step function (Mironov *et al.*, 2010). The Heaviside step function contains a value of either 0 or 1, depending on the result of the calculation following the u character (i.e. $u(x)$). If $x > 0$, $u(x) = 1$. If $x \leq 0$, $u(x) = 0$. For example, for the first occurrence of u in Equation 4.26, if $m_g - m_{g1}$ is > 0, $u(m_g - m_{g1})$ will equal 1. If $m_g - m_{g1}$ is ≤ 0, $u(m_g - m_{g1})$ will equal 0 (Mironov *et al.*, 2010). For frozen soil, Equation 4.27 is applied:

$$\begin{aligned}\frac{n_s^*-1}{\rho_d(m_g)} &= \frac{(n_m^*-1)}{\rho_m} \\ &+ \frac{(n_b^*-1)}{\rho_b}[m_g + ((m_{g1}-m_g)u(m_g-m_{g1}))] \\ &+ \frac{(n_t^*-1)}{\rho_t}[(m_g-m_{g1})u(m_g-m_{g1}) + (m_{g2}-m_g)u(m_g-m_{g2})] \\ &+ \frac{n_{iw}^*-1}{\rho_{iw}}(m_g-m_{g2})u(m_g-m_{g2})\end{aligned} \tag{4.27}$$

where n_t^* is the CRI for transient water (from Equations 4.16 and 4.17); ρ_t is the density of transient water (1g/cm^3); n_{iw}^* is the CRI for moistened ice water (from Equations 4.16 and 4.17), and ρ_{iw} is the density of moistened ice water (0.917 g/cm^3). All other densities occurring in Equation 4.27 contain the same values as their counterparts in Equation 4.26 (Mironov *et al.*, 2010).

Through the calculation of a single soil CRI value, $\epsilon_r^{'}$ and $\epsilon_r^{''}$ for the soil as a whole can be calculated through Equations 4.14 and 4.15 respectively using the real and imaginary portions of $\frac{n_s^*-1}{\rho_d(m_g)}$ from Equations 4.26 (when thawed) and 4.27 (when frozen) (Mironov *et al.*, 2010).

4.4 Field Measurements

4.4.1 Surface Roughness Sampling

To fulfill the roughness component of the Oh model, surface roughness measurements were completed at the study site on February 12, 2012. While not obtained in conjunction with UW-Scat and TerraSAR-X acquisitions, these measurements should provide a reasonable representation of roughness conditions present during winter acquisitions, due to limited rates of landscape change within the HBL environment. Uncertainty will be greater for UW-Scat and TerraSAR-X measurements obtained during unfrozen ground conditions (i.e. fall and spring) as ground freezing and thawing would alter roughness characteristics.

Roughness was measured using a pin board (Figure 4.6a) containing dimensions of 60 cm (width) by 30 cm (height). 26 cm pins constructed from survey fags were positioned between 5 cm and 55 cm, allowing roughness to be sampled over 50 cm. Pins were held to the board with staples, each of which held 6 pins. This allowed 264 pins to be present on the board, providing a ∼2 mm measurement resolution. Two sheets of plastic were attached to the board to limit snow accumulation and keep the pins in place. A wooden lever mechanism was attached to the bottom of the board to prevent removal of pins during transportation. This was also initially used to release pins for measurement. However, due to difficulties with resetting the board, a clamping mechanism constructed from wood and foam was utilized. Clamping this apparatus to the board over the pins prevented their removal during board movement and also provided more control over board set up and pin release.

Pin board measurements were also aided through a wooden frame (Figure 4.6b). Two 1 m boards were attached to two perpendicular boards to construct the frame. The upper boards were positioned just over 50 cm apart, allowing the 5 cm edges of the pin board to rest on the frame. The frame allowed a ∼10 cm gap between the base of the pin board and the measurement surface, providing space for the pins to fall on to the surface. Lines were drawn at 10 cm intervals on the upper frame boards to provide a reference point for measurement locations. This enabled nine measurements to be obtained along the frame. Two screws positioned at one end of the frame allowed an A-shaped metal camera mount to be centred with the frame. This provided a stable and consistent location for pictures of the pin board to be taken.

Roughness measurements were obtained from a representative area of the Tundra site sampled by UW-Scat and TerraSAR-X (Figure 4.1). Representativeness was evaluated as



(a) (b)

Figure 4.6: Pin board (a) and frame (b) used for surface roughness measurements.

best as possible through snow and vegetation conditions. At the selected location, two sets of measurements were taken back to back, using the frame for alignment (Figure 4.7). This set-up allowed measurements to be obtained over a 180 cm distance, providing improved sampling of the site's roughness. Measurements were completed through three iterations which allowed the full range of roughness to be sampled. First, the snow surface was measured. Second, the snow was removed and underlying vegetation was sampled. Finally, vegetation was removed and bare soil was measured. For each iteration, the pin board was positioned at the first measurement line on the frame (i.e. 10 cm). The pin board was clamped to the frame to ensure stability during measurement. The pin clamping mechanism was removed, allowing the pins to fall onto the surface. Pins which did not reach the surface were manually lowered until slight tension was felt, indicating that the pin was resting on the surface. Two pictures of the pin board were then taken. To reset the pin board, the pin clamping mechanism was placed over the dropped pins and the board was inverted. The pin clamping mechanism was then loosened, allowing pins to fall into their upright position. The pin board was then righted and the next measurement set was completed. Between some measurements the camera height was adjusted to maintain board centring within each picture.

4.4.2 Surface Roughness Picture Processing

Roughness levels in RMS format were retrieved from pin board photographs through a script implemented in the R statistical language (R Development Core Team, 2011). The script operates by examining the variation of a line defined by the transition between two colours. To facilitate this procedure, pin board pictures were converted into black and



Figure 4.7: Back to back surface roughness measurement set-up used at the study site. Frame is positioned over Location One while snow has been removed from Location Two.

white images, with the black portion positioned below the pins and the white portion above (Figure 4.8)[10]. The transition was defined by the top of the pins. A black line was drawn from pin to pin, connecting each and establishing the transition between the black and white sections. The remaining area above the line was filled black while the area below was filled white, creating the black and white image. Each picture was also cropped so that only the area containing pins was used within the R script. Run length encoding was applied to each picture to identify the pixel location in each column where the transition from black to white occurred. As image dimensions were known, pixel locations could be transformed into a length measurement (i.e. mm). With length values determined for all image columns, the Root Mean Square Error (RMSE) calculation could be applied to determine the average variation in pin heights across the image:

$$\sqrt{\sum \frac{l - \bar{x}(l)^2}{i}} \tag{4.28}$$

[10]Photograph editing was completed using the GNU Image Manipulation Program (GIMP), Version 2.6.11. GIMP is available on-line at: http://www.gimp.org/

where l is the position of the transition from white to black (i.e. the top of the pins) in mm for each column in the image, $\bar{x}(l)$ is the mean of the position values and i is the total number of position measurements (i.e. the number of columns in the image). This produced an RMS surface roughness value in mm format. This value was converted to cm for use in the Oh model. Note that for this research, only soil surface roughness measurements were used for Oh model parametrization as the majority of X-band backscatter should have been returned from the soil surface at both study sites.



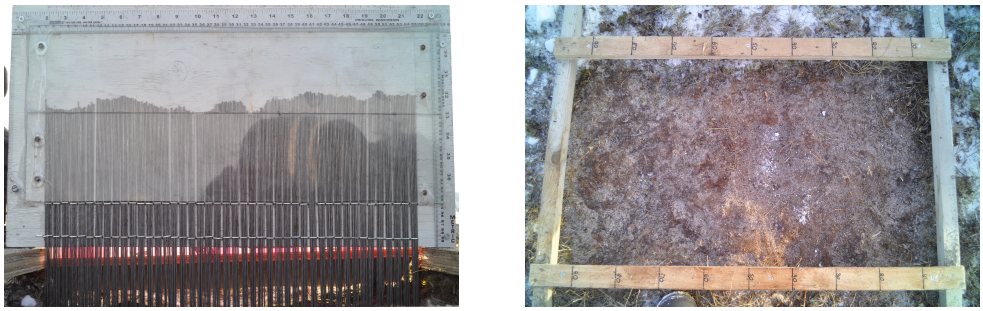
Figure 4.8: Example of a processed surface roughness picture. Photograph represents soil roughness measured at study site Location Two at the 50 cm position on the measurement frame. The processed picture is ∼50 cm wide. The height of the picture was cropped to allow the tops of the pins (i.e. transition from white to black) to be visible over the entire width while removing excess picture area.

4.4.3 Roughness Used within the Oh Model

To simplify operation of the Oh model, three RMS levels were defined: 0.62, 1.15 and 1.84 cm (Figures 4.9 and 4.10). These represent, respectively, the minimum, median and maximum bare soil RMS levels measured at the study site. Exploring this range provided an opportunity to potentially characterize the RMS level which best represented the UW-Scat and TerraSAR-X scenes. It should be noted that each RMS level exceeded Rayleigh and Fraunhofer criteria for a rough surface (Ulaby *et al.*, 1982) at the examined UW-Scat and TerraSAR-X wavelengths and incidence angles.

4.5 Laboratory Measurements

As *in situ* measurements of soil ϵ_r were not obtained in conjunction with UW-Scat and TerraSAR-X measurements, TD GRMDM estimates are used within this research to provide the ϵ_r parameter for the Oh model. As TD GRMDM was designed to represent ϵ_r characteristics of soil for a single study site, its ability to represent ϵ_r of the site



(a) (b)

Figure 4.9: (a) Pin board picture for 0.62 cm soil surface roughness. (b) illustrates ground characteristics where measurement was obtained (Location One). The measurement was acquired at the 60 cm position.



(a) (b) (c)

Figure 4.10: Pin board pictures for 1.15 (a) and 1.84 cm (b) soil surface roughness levels. (c) illustrates ground characteristics where these measurements were obtained (Location Two). 1.15 and 1.84 cm levels were obtained at the 20 and 50 cm positions respectively.

explored within this research must be evaluated. This was accomplished through the acquisition of a soil sample from the study site in December 2012. ϵ_r measurements under a range of moisture and temperature conditions were completed to evaluate TD GRMDM's ability to represent the specific soil type explored within this research in addition to providing measured soil ϵ_r values which could be implemented directly within the Oh model. Although the acquisition of ϵ_r measurements from the study site soil could have replaced the use of TD GRMDM within this research, the opportunity to expand the use of TD GRMDM was viewed as beneficial, particularly for potential TD GRMDM use within Oh model parametrization for other Arctic and sub-Arctic regions within a dual-frequency SWE retrieval framework.

4.5.1 Sample Description

The dimensions of the sample obtained from the study site were approximately 50 cm (length) by 50 cm (width) by 23 cm (height) (Figure 4.11a). It consisted of two primary layers, beginning with an overlying organic layer comprised primarily of grass, moss and decayed vegetation. This top layer made up only a small portion of the sample, containing a thickness of $\sim$5 cm. The majority of the sample was made up of the second layer, consisting of decomposed peat extending from the base of the organics layer to the bottom of the sample. This layer contained organic material within various stages of decomposition, with the most decomposed material present at sample's base. Layers closer to the surface contained a greater proportion of less decomposed material (Figure 4.11b). Mineral matter (i.e. sand) was present sporadically throughout the sample, but did not comprise a substantial portion of its volume. The presence of relatively intact organic material throughout the sample provided structural integrity, preventing the sample from slumping outside of its square dimensions. The sample's moisture content was relatively high, with gravimetric values of $\sim$4 g/g measured from the top and bottom of the sample. Moisture retention was also high, with little pooled water present at the bottom of the sample after extraction.

4.5.2 Measurement Overview

Measurements performed on the peat sample focused on deriving information for TD GRMDM evaluation. Gravimetric moisture content, bulk density, volume, temperature and ϵ_r were sampled. ϵ_r measurements were obtained using Stevens® Hydra Probe II® instruments, operating at a frequency of 50 MHz (Stevens Water Monitoring System Inc.,



(a) (b)

Figure 4.11: (a) Peat sample obtained from the study site. (b) illustrates characteristics of the sample. With a small portion of the sample removed, the thickness of the organic layer can be seen. Organic matter present throughout the soil is also visible.

2007). Temperature measurements were obtained using Campbell Scientific® 105T thermocouples. ϵ_r and temperature measurements were performed under thawed and frozen conditions to test TD GRMDM's thawed and frozen components. Accuracy of the Stevens Hydra Probes was evaluated by placing the sensor in distilled water and measuring ϵ_r under liquid and frozen conditions. Figure 4.12 illustrates the results, which agree well with theoretical $\epsilon_r^{'}$ values in water (i.e. $\sim$80) and ice (i.e. $\sim$3.15) (Colbeck, 1982; Scherer *et al.*, 2005). Observation of thermocouple measurements under room and freezing temperature conditions revealed consistency and accuracy in these sensor measurements.

The measurement process consisted of three stages: first, the sample in its whole form was instrumented with ϵ_r probes and thermocouples in order to measure these characteristics while the sample remained in its field state. During the second stage small samples were removed from the top and bottom of the sample to complete additional measurements where the water content of the soil was altered. In the final stage the structure of the small samples was destroyed by grinding them into powder, in order to replicate the experiment conducted by Mironov *et al.* (2010). The moisture content of the ground-up samples was also altered to match the experiment procedure outlined by Mironov *et al.* (2010). Through these stages, the ability of TD GRMDM to properly estimate ϵ_r

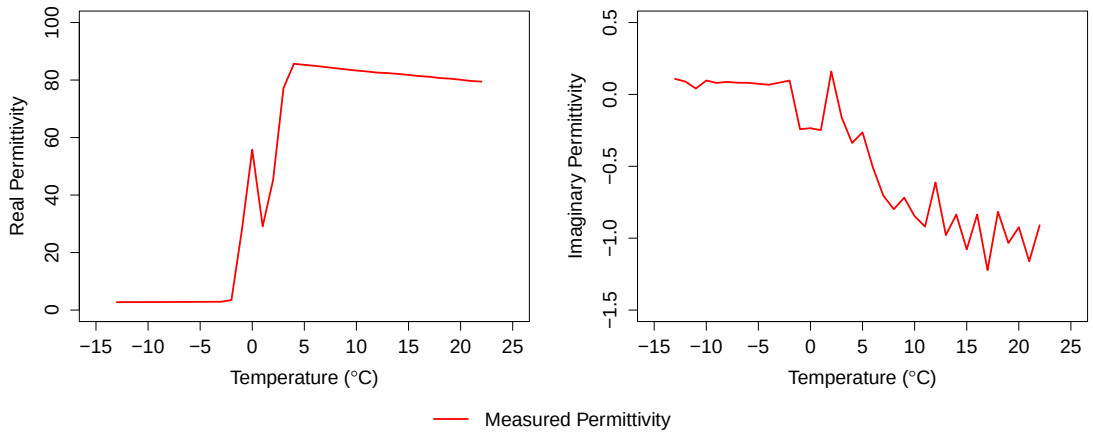


Figure 4.12: Stevens Hydra Probe II measurements of distilled water under liquid and frozen conditions. Results demonstrate consistency with theoretical ϵ_r values for water (i.e. ∼80) and ice (i.e. ∼3.15) (Colbeck, 1982; Scherer *et al.*, 2005).

characteristics of the study site's soil under frozen and thawed conditions was evaluated. The use of ground-up and unaltered soil also allowed the model to be evaluated under conditions for which it was developed in addition to near-real world soil characteristics.

Stage 1: Whole Form Measurements - Sampling began in January 2013 through instrumentation of the entire peat sample. As the peat was obtained in December 2012, it was kept frozen until time allowed measurements to be completed. To facilitate instrumentation, the sample was thawed. Wrapping of the sample in plastic after extraction from the field allowed for the greatest possible retention of natural soil moisture. Two ϵ_r probes were utilized, one positioned ∼3.5 cm below the surface of the sample with the other located ∼7 cm above the bottom of the sample (Figure 4.13a). Two thermocouples were positioned near the ϵ_r probes to provide a record of soil temperature at each measurement location (Figure 4.13b). An additional thermocouple was positioned near the middle of the sample (i.e. ∼10.5 cm below the surface) to facilitate the development of a soil temperature profile. The final thermocouple was located above the sample to measure the surrounding air temperature. In addition to being wrapped in plastic, the sample was placed in a foam box and surrounded with additional foam packaging material, with only its surface left uninsulated (Figure 4.13c). This was completed in an attempt to simulate a natural soil condition where temperature



(a) (b) (c)

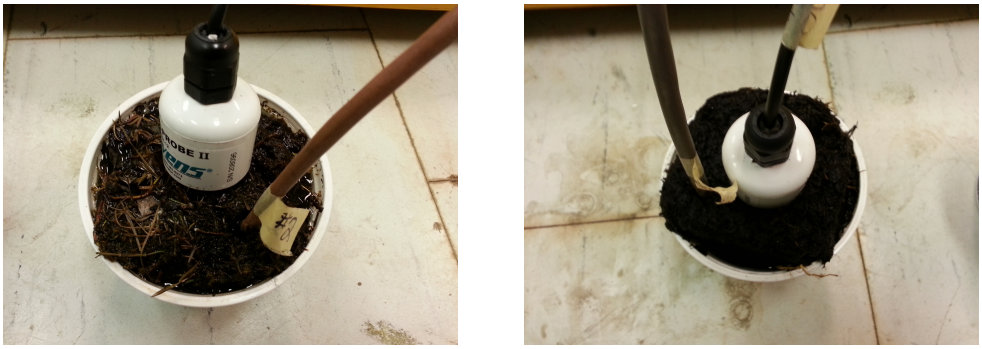
Figure 4.13: Instrumentation of whole peat sample. (a) illustrates the location of the two ϵ_r probes. (b) presents a close-up view of the ϵ_r probe near the top of the sample, in addition to the thermocouples positioned at the top of the sample and within the air above. Foam packed around the sample simulated the insulating effect of surrounding terrain. (c) illustrates complete instrumentation. The top of the sample was left uninsulated to simulate the natural condition of air temperature acting on the soil. Plastic wrapped around the sample helped retain soil moisture.

changes at the soil surface present the greatest influence to the soil volume. The instrumented sample was placed into a commercial freezer for 7 days to simulate the onset of winter. The sample remained in the freezer until the near-surface thermocouple recorded a temperature of -7°C, placing the sample into the frozen soil condition defined by Mironov *et al.* (2010) (i.e. -6°C). Time constraints prevented the sample from remaining in the freezer where it may have achieved a lower temperature. The sample was then removed from the freezer and allowed to thaw to room temperature.

After the sample had thawed, small portions of soil were removed from the top and bottom layers to facilitate gravimetric soil moisture measurement. Gravimetric moisture measurement was completed by comparing weights of the samples while wet (i.e. near field condition) to weights obtained after the samples were dried in a 105°C oven over 48 hours. Equation 4.29 defines this process (ASTM International, 2010):

$$w\ (\mathrm{g/g}) = (M_{cms} - M_{cds})/(M_{cds} - M_c) \tag{4.29}$$

where w is the water content; M_{cms} is the mass of the moist soil and the container holding the sample; M_{cds} is the mass of the dried soil and container, and M_c is the mass of the container. Moisture contents for the top and bottom samples were 3.99 and 2.43 g/g respectively.



(a) (b)

Figure 4.14: Instrumentation of small peat samples for Stage 2 measurements. (a) illustrates sample obtained from the top of the peat while (b) indicates sample taken from the bottom of the peat. Note that both pictures were taken after the samples were saturated with water.

Stage 2: Small Sample Measurements - Upon completion of the whole sample experiment, samples of peat were removed from the top and bottom layers to facilitate further measurement[11] (Figure 4.14). A ϵ_r probe and thermocouple were placed into the centre of each sample with an additional thermocouple present outside of the samples to measure air temperature. The samples were again subjected to freezing and thawing, but also to altered soil moisture conditions. First, measurements were performed without moisture alteration in order to obtain measurements as close to the sample's natural field condition as possible. Second, each sample was completely saturated with water to evaluate ϵ_r and temperature characteristics under saturated soil conditions. Finally samples were dried in a 105°C oven over 48 hours with additional ϵ_r and temperature measurements performed on the dried samples. Samples were frozen within a chest freezer until reaching equilibrium with the freezer's air temperature (∼-12°C) and then thawed until reaching room temperature. Gravimetric moisture levels were calculated for each sample when the samples were in their field state (4.45 and 3.97 g/g for top and bottom samples respectively) and saturated (6.63 and 4.08 g/g for top and bottom samples respectively).

Stage 3: Ground-Up Sample Measurements - Once the measurements of the small dried samples were completed, each sample was ground to powder within a coffee grinder to replicate the procedure defined by Mironov *et al.* (2010) (Figure 4.15). Grinding allowed

[11]Note that the samples extracted for this stage were different from those extracted in Stage 1 for soil moisture determination.



(a) (b)

Figure 4.15: Pictures of small samples after grinding. (a) illustrates the top sample while (b) represents the bottom sample.

specific moisture contents to be achieved through addition of distilled water to the ground-up soil. Moisture contents from 0.0 (dry) to 1.1 g/g in steps of 0.1 g/g were tested to match the soil moisture levels explored within Mironov *et al.* (2010). Additional moisture contents of 4.45 and 3.97 g/g were completed for the top and bottom samples respectively to examine the influence of grinding on temperature and ϵ_r at the moisture levels observed for the field state of each sample.

The amount of water required for each soil sample (M_w) to achieve a given moisture content was determined through:

$$M_w = M_{ds} * mg \tag{4.30}$$

where M_{ds} is the mass of the dry soil sample and mg is the desired gravimetric water content. The calculated mass of water was added to the appropriate soil sample and stirred to distribute it evenly through the sample. This was difficult for lower water contents as the peat absorbed the water quickly, transforming portions of the soil into clumps. Freezing and thawing was performed in the same manner as for Stage 2 measurements. The volume of the dried ground-up samples was also determined to enable the calculation of bulk density. Volume was measured by pouring the dried ground-up sample into a beaker. Volumes for ground-up top and bottom samples were determined to be 140 and 325 cm^3 respectively. Bulk density (ρ_d) of the dried samples was calculated using (Mironov *et al.*, 2010):

$$\rho_d = M_d/V \tag{4.31}$$

where M_d is the mass of the dried soil and V is its volume in cm^3. Bulk densities for the ground-up top and bottom samples were calculated as 0.420 and 0.409 g/cm^3 respectively.

4.6 Analysis Methodology

Experimental analysis consisted of two parts: 1) evaluating TD GRMDM for the study area's soil conditions using measurements obtained from the three stages of the laboratory experiment, and 2) evaluating the Oh model for backscatter representation of the study site's terrain through comparisons with UW-Scat and TerraSAR-X measurements. Descriptions of each analysis step are presented in the following sections.

4.6.1 TD GRMDM Evaluation

To evaluate the TD GRMDM approach for soil conditions of the study site, TD GRMDM estimates were compared with ϵ_r measurements obtained during Stages 1-3 of the laboratory measurement process. This led to three comparisons: TD GRMDM vs. Ground-Up Sample ϵ_r; TD GRMDM vs. Small Sample ϵ_r, and TD GRMDM vs. Whole Sample ϵ_r, corresponding to laboratory measurement Stages 3, 2 and 1 respectively. The comparison between TD GRMDM and ground-up sample ϵ_r measurements were completed first as the ground-up sample measurements represented the closest methodology to that implemented in Mironov *et al.* (2010) for TD GRMDM development. Comparisons between TD GRMDM, small sample ϵ_r and whole sample ϵ_r represented an extension of TD GRMDM to natural soil conditions. Results of these comparisons are important for determining the ability of TD GRMDM estimates to parametrize the Oh model to allow for proper backscatter representation from natural terrain conditions.

To facilitate each comparison, aspects of TD GRMDM were specified to produce appropriate estimates for each soil sample. TD GRMDM requires the specification of four parameters: soil temperature, gravimetric soil moisture, dry soil bulk density and measurement frequency. Soil temperature measurements were obtained from thermocouples used in conjunction with ϵ_r probes for each laboratory measurement stage. Soil moisture and bulk density values were obtained from samples used within each laboratory measurement stage. Table 4.5 presents the soil temperature, moisture and

Table 4.5: Soil parameters used within each comparison for TD GRMDM evaluation

Comparison Soil Sample	Soil Temperature Range (°C)		Gravimetric Soil Moisture (g/g)	
	Top	Bottom	Top	Bottom
Ground-Up	-13 - +21	-13 - +21	0 - 1.1, 4.45	0 - 1.1, 3.97
Small	-13 - +21	-13 - +21	0, 4.45, 6.63	0, 3.97, 4.08
Whole	-8 - +10	-6 - +7	3.99	2.43

Comparison Soil Sample	Dry Soil Bulk Density (g/cm^3)	
	Top	Bottom
Ground-Up	0.420	0.409
Small	0.114	0.195
Whole	0.577	0.726

bulk density values used for each comparison. For frequency, TD GRMDM estimates for use in the Oh model used frequencies matching UW-Scat and TerraSAR-X (i.e. the measurements to which Oh model estimates were compared). These corresponded to 9.65 and 9.6 GHz for TerraSAR-X and UW-Scat respectively. For TD GRMDM estimate comparison to Stevens probe ϵ_r measurements, 50 MHz was used. Note that only comparison results for measurements obtained from the top of the peat sample within each experiment stage are presented in Section 5.1 as results for the bottom samples were similar. Comparison results for the bottom samples are presented in the Appendix.

4.6.2 Oh Model Evaluation

Evaluation of the Oh model was completed through time series comparisons of Oh backscatter estimates with both TerraSAR-X and UW-Scat measurements obtained from the study site. The parameters required for the model, namely incident angle, wavelength, surface roughness and soil ϵ_r, defined the modelling approach for this research. For incident angle, 44° was used to produce estimates for TerraSAR-X acquisitions. For UW-Scat, 45° was used as this represented the elevation angle which most closely matched TerraSAR-X's incident angle. For wavelength, 3.11 and 3.12 cm were used for TerraSAR-X and UW-Scat respectively, corresponding to their frequencies of 9.65 and 9.6 GHz respectively. For surface roughness, measured RMS values of 0.62, 1.15 and 1.84 cm were chosen[12]. For ϵ_r, laboratory measured values as well as TD GRMDM estimates were

[12]See Section 4.4.3 for an explanation of why these values were selected.

used to parametrize the model. Laboratory measured values presented the best possible representation of ϵ_r conditions present at the time of TerraSAR-X and UW-Scat measurements, while the use of TD GRMDM estimates allowed for the appropriateness of the use of ϵ_r estimates within the Oh model to be evaluated. For laboratory measurements and TD GRMDM estimates, ϵ_r values obtained from the small sample and whole sample experiments were used. *In situ* soil temperature measurements obtained during UW-Scat and TerraSAR-X acquisitions were used to identify corresponding ϵ_r measurements for input to the Oh model. Note that only laboratory measurements and TD GRMDM estimates obtained for the top portion of the peat sample were implemented in the Oh model as it is unlikely UW-Scat and TerraSAR-X signals reached lower regions of the study site's terrain. Overall, three comparisons were produced for UW-Scat and TerraSAR-X based on the three ϵ_r datasets selected for analysis. Oh model estimates for the selected RMS levels were produced within each comparison.

Chapter 5

Results & Discussion

This chapter presents results and discussion of the analysis completed for this research. Figure 5.1 contains an illustration of the comparison work-flow. To begin, comparisons between measured ϵ_r and companion estimates derived from TD GRMDM for each laboratory measurement stage are presented. Stages are presented in reverse order (i.e. 3, 2, and 1) to demonstrate results most consistent with the methodology implemented in TD GRMDM first, followed by experimental results which extend the application of TD GRMDM to new soil forms. Discussion of these results follows with a focus on determining the ability of TD GRMDM to represent measured ϵ_r values. Next, comparisons between UW-Scat, TerraSAR-X and companion Oh model estimates are presented. Discussion of each comparison will focus on evaluating the ability of the Oh model to represent UW-Scat and TerraSAR-X measurements from the study site environment using *in situ* measurements and TD GRMDM estimates of ϵ_r. This chapter concludes with an evaluation of the potential use of the Oh model within future dual-frequency SWE retrieval frameworks based on results of this research.

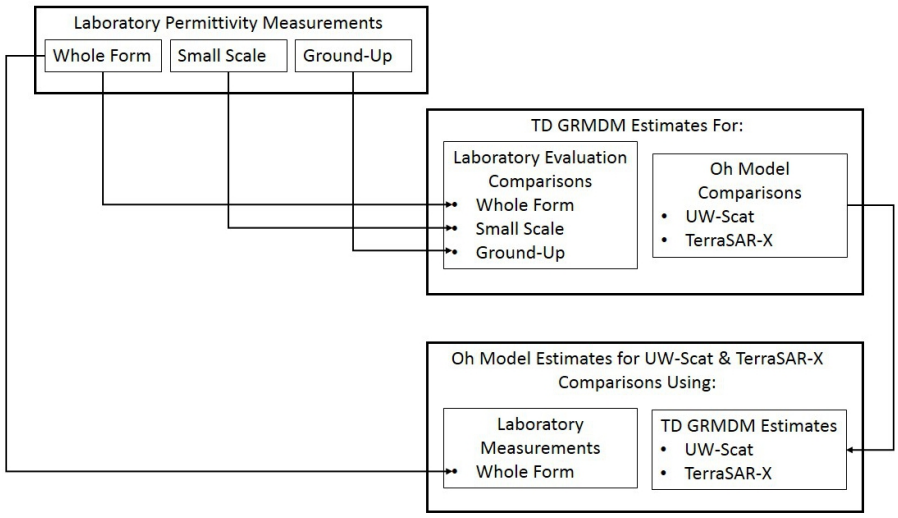


Figure 5.1: Work-flow of comparison methodology illustrating the source of inputs for each comparison step.

5.1 TD GRMDM Evaluation

5.1.1 Ground-Up Sample Measurements (Stage 3) Results

Figure 5.2 illustrates agreement between measured and TD GRMDM estimated $\epsilon_r^{'}$ values for a series of gravimetric soil moisture levels for the ground-up top soil sample. Figure 5.3 presents similar plots for $\epsilon_r^{''}$. Figures 5.4 and 5.5 illustrate differences between measured and estimated $\epsilon_r^{'}$ and $\epsilon_r^{''}$ respectively. On both figures a trend of increasing disagreement between estimated and measured values is apparent, particularly for moisture levels greater than 0.3 g/g. For the moisture level representing the natural field condition of the sample (i.e. 4.45 g/g), disagreement is especially high, reaching differences beyond 250 units for $\epsilon_r^{'}$ and 1200 units for $\epsilon_r^{''}$. It is also evident that disagreement is much higher for soil temperatures above -6°C for higher soil moisture levels. This transition point defines the separation between thawed and frozen soil in TD GRMDM, suggesting a potential problem in the model for the representation of thawed soils.

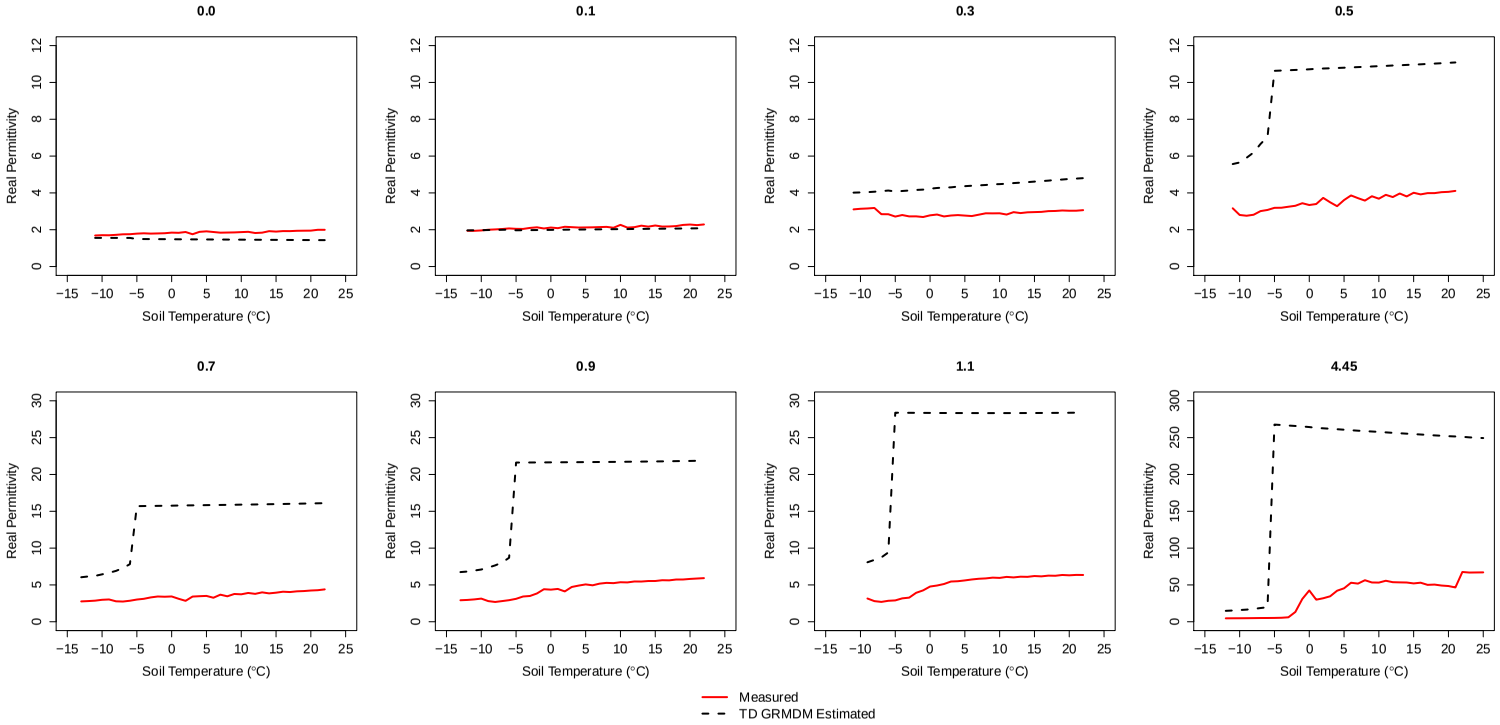


Figure 5.2: Agreement between measured and TD GRMDM 50 MHz estimates of $\epsilon_r^{'}$ obtained for the ground-up top sample. Gravimetric moisture levels of 0.0, 0.1, 0.3, 0.5, 0.7, 0.9, and 1.1 g/g represent a sample of moisture levels examined within TD GRMDM. The 4.45 g/g level represents the measured gravimetric moisture of the small scale top sample in its field state.

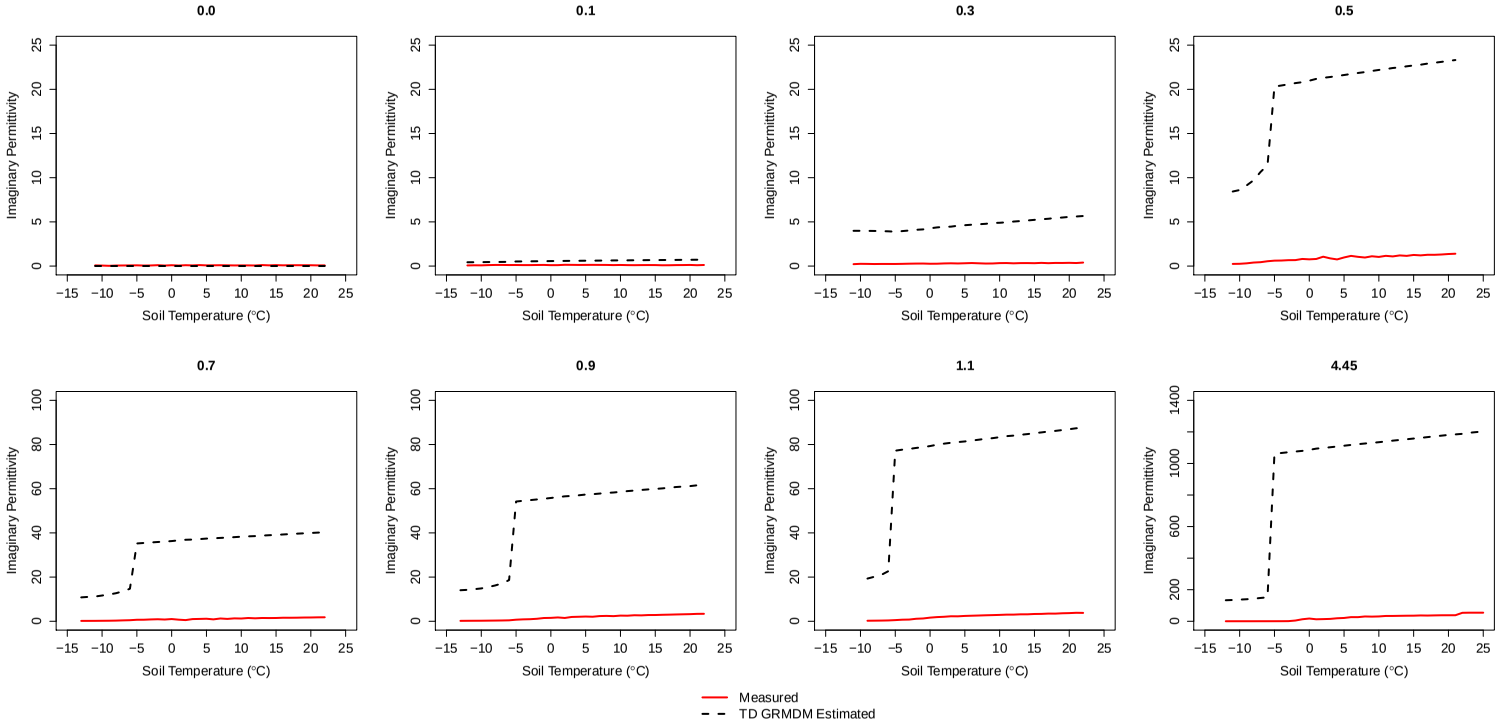


Figure 5.3: Agreement between measured and TD GRMDM 50 MHz estimates of ϵ_r'' obtained for the ground-up top sample. See Figure 5.2 for an explanation of presented moisture levels.

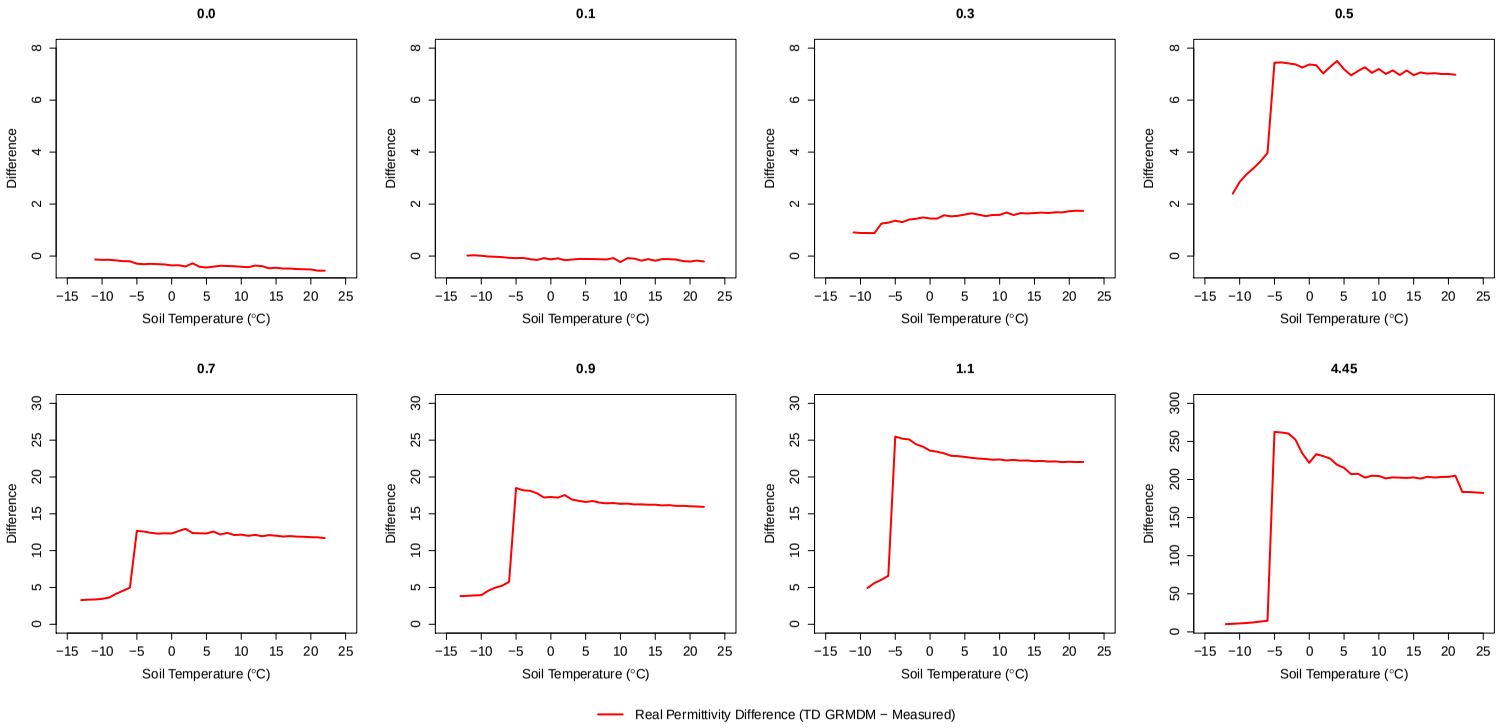


Figure 5.4: Differences between measured and TD GRMDM 50 MHz estimates of $\epsilon_r^{'}$ obtained for the ground-up top sample (TD GRMDM - Measured).

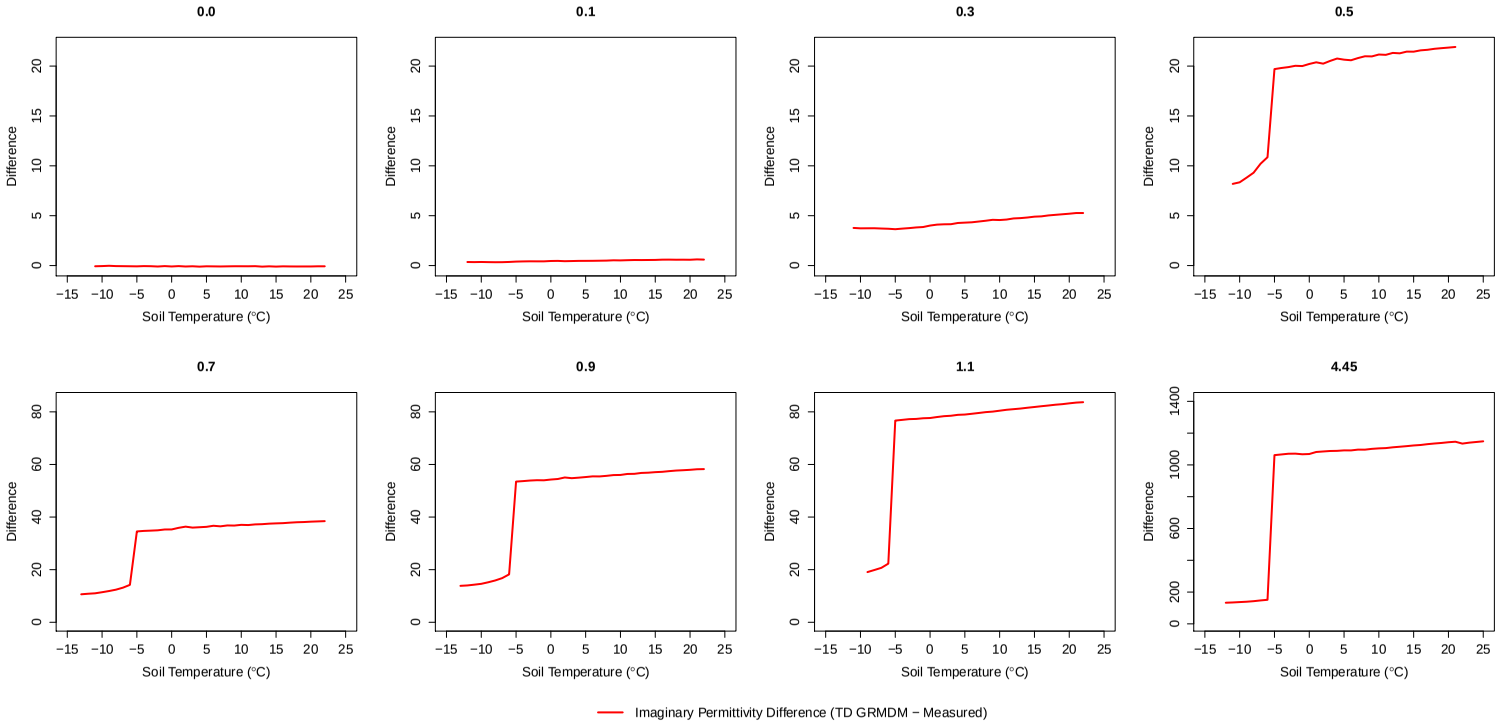


Figure 5.5: Differences between measured and TD GRMDM 50 MHz estimates of ϵ_r'' obtained for the ground-up top sample (TD GRMDM - Measured).

5.1.2 Small Sample Measurements (Stage 2) Results

Figure 5.6 illustrates agreement between measured and TD GRMDM estimated $\epsilon_r^{'}$ and $\epsilon_r^{''}$ for the small top sample prior to grinding. Figure 5.7 illustrate differences between the measured and estimated ϵ_r components for this sample. For $\epsilon_r^{'}$, agreement between measured and modelled results is poor for higher moisture levels, particularly between temperatures of -5 and 5°C. However, in comparison to results obtained for the ground-up sample, differences between measured values and estimates are substantially reduced. For $\epsilon_r^{''}$, results are comparable to those for the ground-up sample, with increasing differences for higher soil moisture levels. However, the magnitude of these differences are lower than those observed for the ground-up sample (e.g. $\sim$90 for small sample 4.45 g/g moisture vs. $\sim$1200 for the ground-up sample). Similar to results for the ground-up sample, measured and estimated $\epsilon_r^{'}$ and $\epsilon_r^{''}$ agreement is worse for thawed soil conditions (i.e. soil temperatures above -6°C). For frozen soil, TD GRMDM estimates are typically only several units away from measured values.

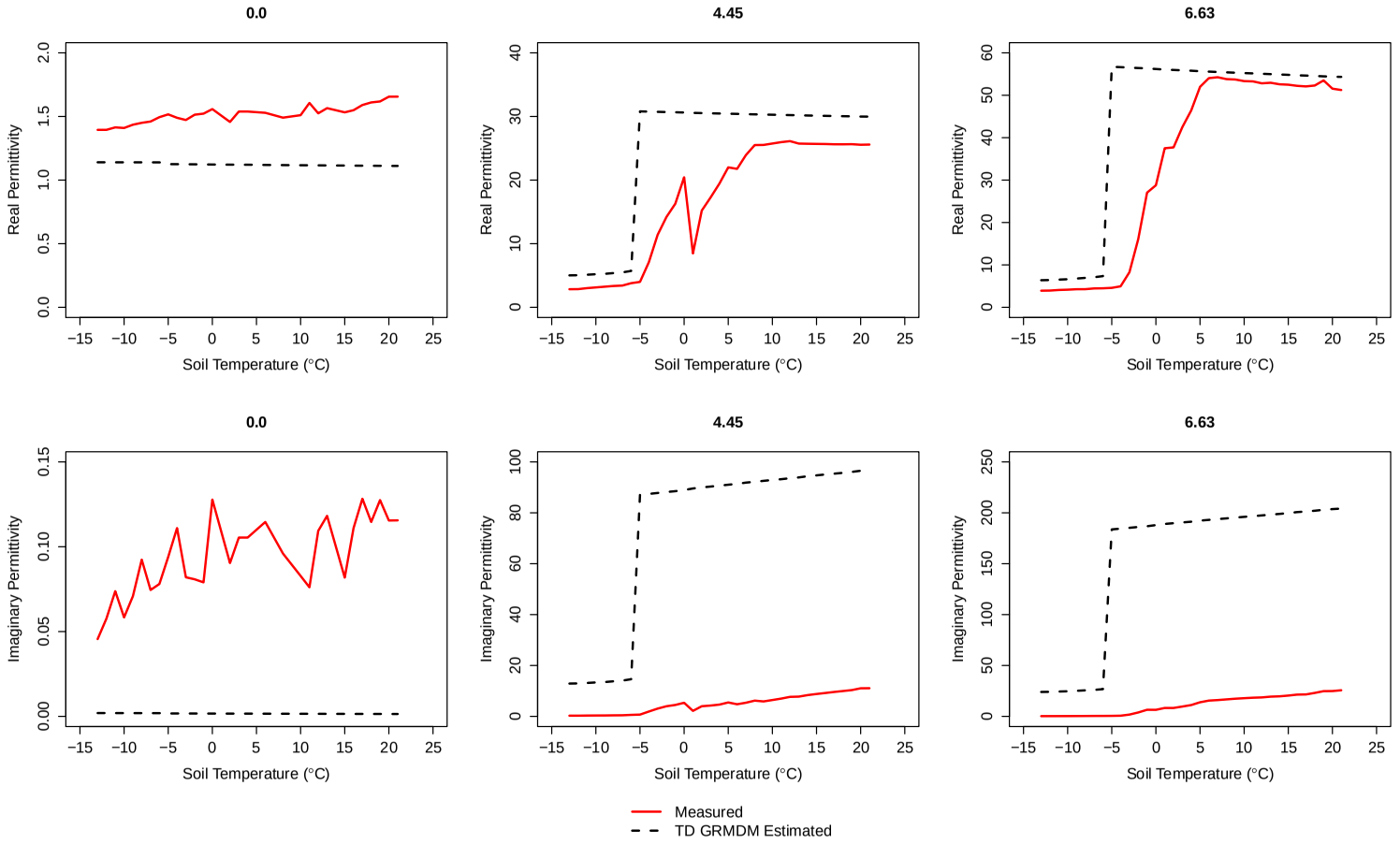


Figure 5.6: Agreement between measured and TD GRMDM 50 MHz estimates of $\epsilon_r^{'}$ and $\epsilon_r^{'}$ for the small top sample. Gravimetric moisture levels of 0.0, 4.45 and 6.63 g/g represent the sample in its dried, field state and saturated conditions respectively.

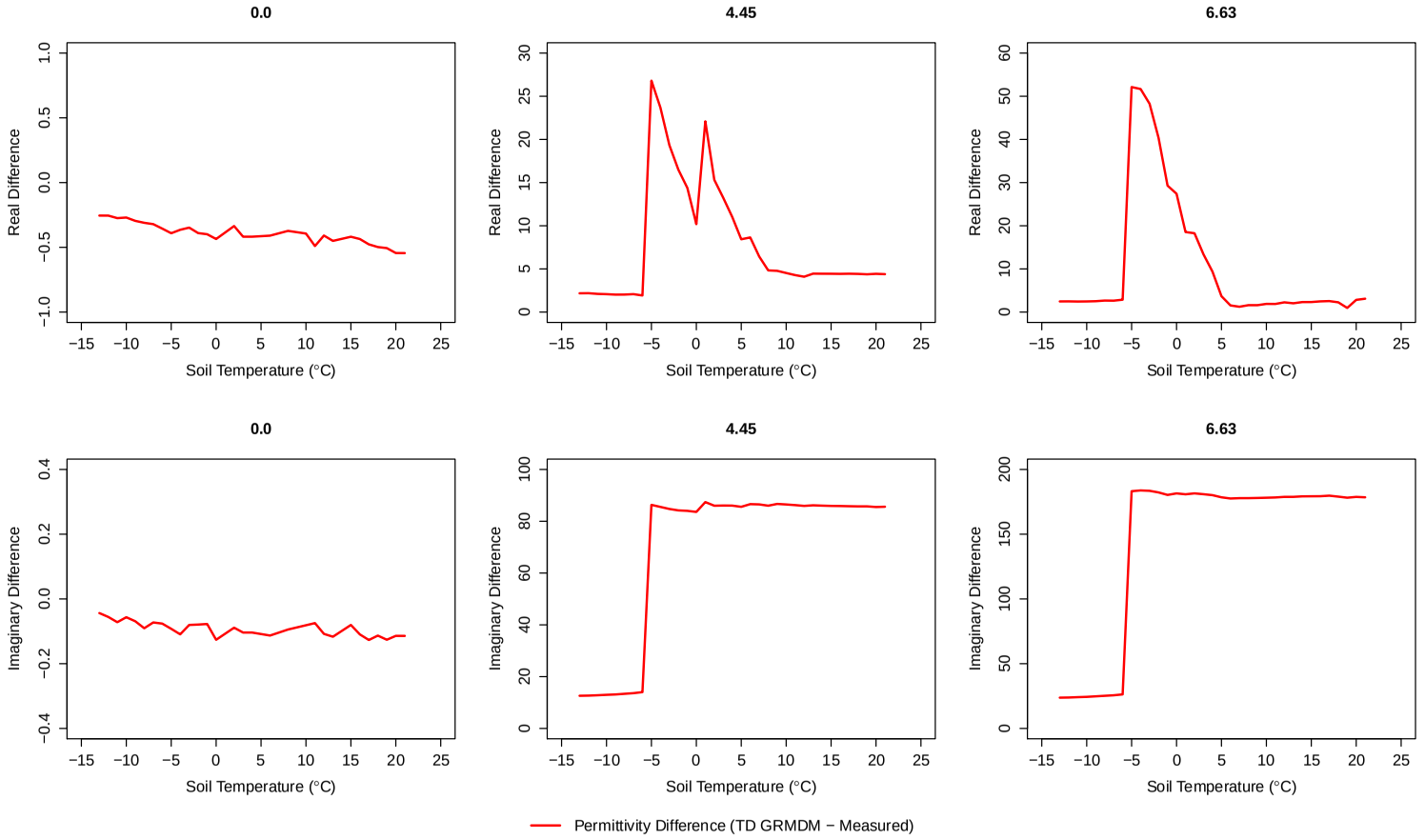


Figure 5.7: Differences between measured and TD GRMDM 50 MHz estimates of $\epsilon_r^{'}$ and $\epsilon_r^{''}$ obtained for the small scale top sample (TD GRMDM - Measured).

5.1.3 Whole Sample Measurements (Stage 1) Results

Figure 5.8 illustrates agreement as well as differences between measured and TD GRMDM estimated $\epsilon_r^{'}$ and $\epsilon_r^{''}$ for the top portion of the whole peat sample. Based on the moisture content of this sample (3.99 g/g), results are similar to the ground-up sample measurements preformed for the 4.45 g/g moisture content (Figures 5.2 and 5.3), namely a high level of disagreement between the measured and modelled results for both $\epsilon_r^{'}$ and $\epsilon_r^{''}$ for this high moisture content. Again, this is most evident for thawed soil conditions. Frozen soil conditions (i.e. soil temperatures below -6°C) illustrate substantially better agreement.

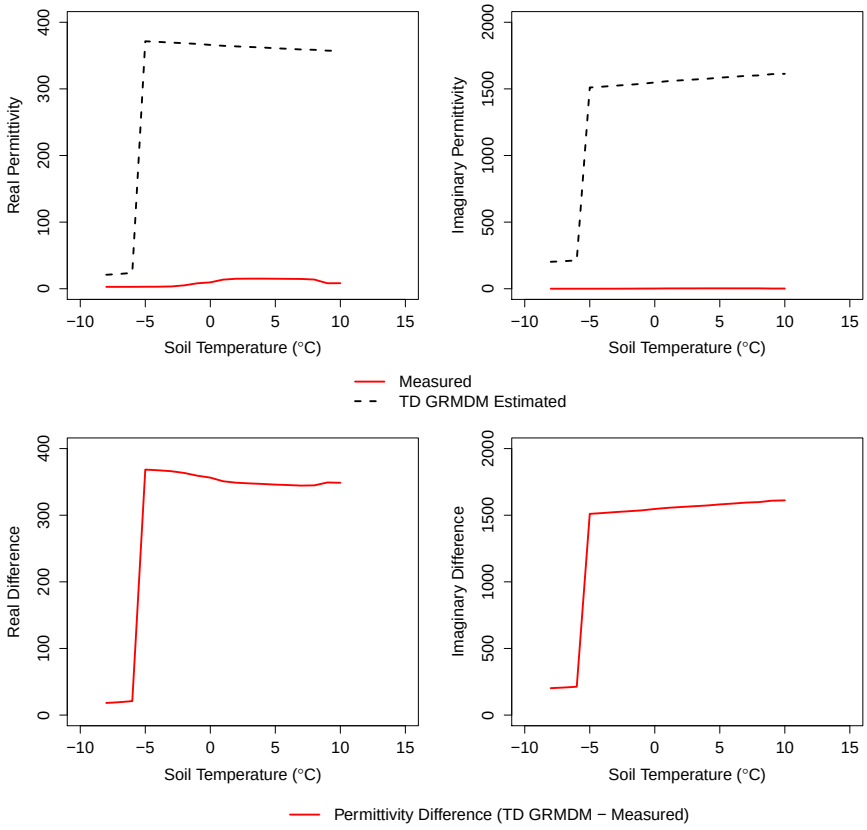


Figure 5.8: Agreement (top) and differences (bottom) between measured and TD GRMDM 50 MHz estimates of $\epsilon_r^{'}$ and $\epsilon_r^{''}$ obtained for top portion of the whole sample (TD GRMDM - Measured).

5.1.4 TD GRMDM Evaluation Discussion

From the results presented in Sections 5.1.1 to 5.1.3, it is clear that TD GRMDM has difficulty representing ϵ_r for peat obtained from the study site based on moisture and temperature conditions of its natural environment. Results obtained for the ground-up sample (Figures 5.2 - 5.5) are most relevant for TD GRMDM evaluation as they best represent the methodology used within Mironov *et al.* (2010). For both $\epsilon_r^{'}$ and $\epsilon_r^{''}$, TD GRMDM estimates most closely matched measured values for lower soil moisture contents, in some cases achieving near-zero disagreement. However, for higher soil moisture contents under thawed conditions, in particular the soil moisture representing the natural condition of the sample, TD GRMDM estimates were different than the measured values. Results for frozen soil were much better, with differences remaining more stable for all soil moisture contents for $\epsilon_r^{'}$. $\epsilon_r^{''}$ differences were more variable at increased soil moisture levels under frozen conditions, but still exhibited much less variability than differences for thawed soil.

For the ground-up sample, the poor agreement observed for the natural soil moisture condition, as well as observations made during the measurement of this moisture level, call into question the appropriateness of the TD GRMDM development methodology. The 4.45 g/g moisture content explored at this stage represented just over 4 grams of water being present for each gram of ground peat. With a much higher ratio of water to soil, this mixture developed a highly liquefied texture, with a small portion of liquid water remaining above the solid component of the ground-up sample throughout the measurement process (Figure 5.9). This represents a very different condition in comparison to the natural state of the sample explored within the small sample experiment stage (Figure 4.14), wherein visible liquid water (i.e. liquid water present outside of the soil volume) was not present. Such a condition also presented challenges to the use of the HydraProbe which is supposed to remain completely in contact with soil material to achieve correct measurements. The presence of liquid water above the soil volume prevented perfect contact between the base of the HyrdaProbe sensor and the soil volume, possibly affecting measurement accuracy. Overall, this observation illustrates a potential shortcoming in the TD GRMDM methodology, particularly for organic soils containing high moisture contents and irregular textures.

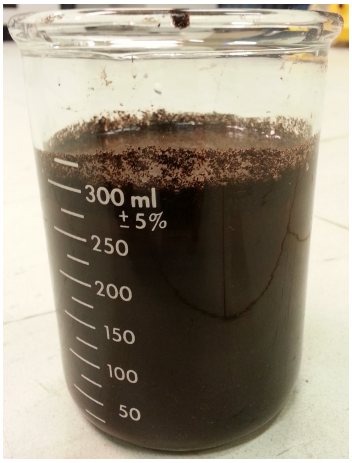


Figure 5.9: Ground-up top sample at 4.45 g/g moisture content, representing the natural moisture condition of the small peat sample. Note the highly liquefied nature of the soil as well as the presence of liquid water above the soil volume.

Through the small scale (Figures 5.6 - 5.7) and whole form (Figure 5.8) experiments, the results also demonstrate similar TD GRMDM behaviour as that observed for ground-up sample measurements. The primary difference is represented by improved agreement within the small scale results. While the general trend of model behaviour is consistent for all experiment stages, namely increasing disagreement between TD GRMDM estimates and measured ϵ_r for higher soil moisture contents and thawed soil conditions, improved agreement within the small scale measurement stage contrasts with higher disagreement observed for whole form and ground-up measurement stages. This lack of consistency suggests a potential problem in model parametrization which is specific to this experiment. Soil bulk density represents the most likely parameter for this error, as the only other parameter altered between measurement stages was soil moisture. Soil moisture was measured in the same way throughout the experiment, while slightly different methods were used to measure bulk density. In all experiment stages, bulk density was calculated by dividing the weight of the dried samples by their volume. For the ground-up sample the measurement of volume was accomplished by placing the sample in a beaker, while for the whole form and small samples, a water displacement method was used. This inconsistent methodology may have impacted the accuracy of the bulk density values which were used within TD GRMDM for each experiment stage. The water displacement method was also not implemented within the development of TD GRMDM; as such bulk density values used to generate estimates for the whole form and

small sample measurement stages may not have been appropriate for use within the model. While potentially impacting the consistency of results between each measurement stage, the use of different bulk density measurement techniques does not appear to have affected the general agreement trend between modelled and measured ϵ_r, which still suggests improvements are necessary to properly apply TD GRMDM within the study site's environment.

Overall, the evaluation results do not illustrate either complete failure or success of the model as both excellent and poor agreement was observed. TD GRMDM estimates from frozen soil appear to represent measured values well in most cases, suggesting this component of the model is appropriate for application within the study site's environment. However, poor performance of the model under thawed soil conditions for higher moisture contents indicates the need for refinement under these conditions. Future work should also examine the use of a different methodology for developing representations of organic soil ϵ_r as the use of ground-up soil does not accurately reflect the characteristics of natural peat, particularly for high moisture contents.

5.2 Oh Model Evaluation

5.2.1 Agreement using TD GRMDM ϵ_r

Figures 5.10a and 5.10b illustrate TD GRMDM ϵ_r estimates for UW-Scat and TerraSAR-X acquisitions respectively. Figures 5.11 and 5.13 illustrate agreement between UW-Scat and TerraSAR-X measurements of X-band backscatter with corresponding Oh model estimates which used TD GRMDM estimates of ϵ_r for parametrization. Average differences between Oh model estimates and the remote sensing measurements for each RMS level and polarization are shown in Table 5.1.

For UW-Scat, Oh model estimates consistently underestimate measured backscatter for each polarization (Figure 5.11). This underestimation is highest for the November 23rd and October 18th acquisitions, as well as for the majority of acquisitions between January 4th and March 3rd. From a surface roughness perspective, the highest measured roughness (1.84 cm) demonstrated the greatest agreement with UW-Scat measurements. Differences between Oh estimates and UW-Scat measurements for this roughness level are typically $\sim$7.5 dB for non-excavation UW-Scat measurements (Table 5.1). Differences between Oh model estimates and UW-Scat excavation measurements are $\sim$5 dB for each polarization for 1.84 cm roughness, representing a substantial improvement over

acquisitions where snow is present. Bare ground UW-Scat acquisitions also exhibit similar agreement with Oh estimates. Note that the drop in Oh backscatter after November 15 is due to the onset of freezing soil conditions which influences TD GRMDM ϵ_r estimates. The increase in UW-Scat backscatter on December 18 may be due to movement of water toward the soil surface with the onset of freezing soil surface temperatures after November 15 (Figure 3.3). As demonstrated by Nagare *et al.* (2012), water contained in soil moves toward the soil surface as freezing conditions propagate into the soil. As moisture levels at the study site were known to be high, sufficient water would likely have been present to transition toward the soil surface. This movement would have increased moisture levels near the soil surface, thus increasing reflectivity and UW-Scat backscatter. Oh model estimates appear to capture this change, likely due to changing permittivity conditions captured by TD GRMDM.

Figures 5.12 and 5.14 illustrate correlations between UW-Scat (Figure 5.12), TerraSAR-X (5.14), and the Oh model for the 1.84 cm roughness level[1]. UW-Scat excavation measurements are not contained within the correlation shown in Figure 5.12. For UW-Scat (Figure 5.12), VV and HH demonstrate non-significant correlations between the ground-based measurements and model estimates. HV does illustrate a significant correlation, but this may be due to the appearance of two outliers at UW-Scat and Oh model backscatter values of -15 and -20 dB respectively. Overall, these results demonstrate low agreement levels between UW-Scat and Oh model estimates incorporating TD GRMDM estimated ϵ_r.

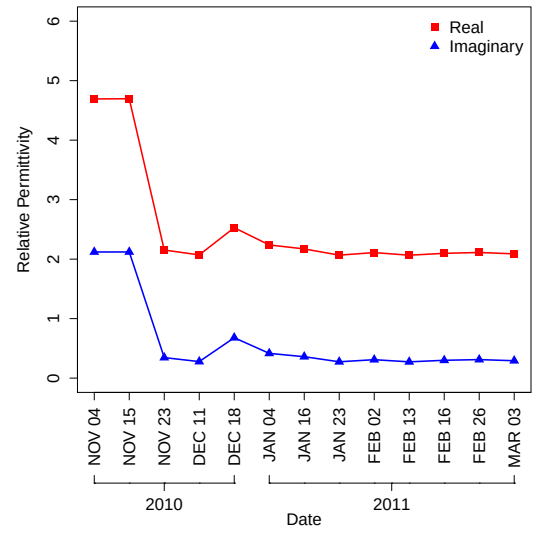
Agreement between TerraSAR-X acquisitions and Oh estimates incorporating TD GRMDM ϵ_r (Figure 5.13) is less consistent than agreement for UW-Scat. Figure 5.14 also demonstrates this through non-significant correlation for both polarizations. For TerraSAR-X's VH polarization, the compared Oh HV estimates demonstrate similar agreement as that for UW-Scat HV measurements (i.e. $\sim$7.5 dB) (Table 5.1). For acquisitions near the beginning and end of the study period where soil temperatures are above -6°C, the agreement is increased with differences of $\sim$5 dB (Figure 5.13). For the VV polarization, the results are more complex, with no single roughness level producing the greatest agreement throughout the study period. As well, Oh estimates do not consistently underestimate TerraSAR-X VV measurements as they did for TerraSAR-X's VH polarization and all polarizations for UW-Scat. Unlike UW-Scat measurements, TerraSAR-X observations do not illustrate an increase in backscatter in mid-December. This may be due to the differing sensitivity of TerraSAR-X to local conditions in comparison to UW-Scat, whose reduced range to the terrain would enhance its sensitivity to local terrain changes.

[1]Correlations represent the Pearson's product-moment correlation coefficient

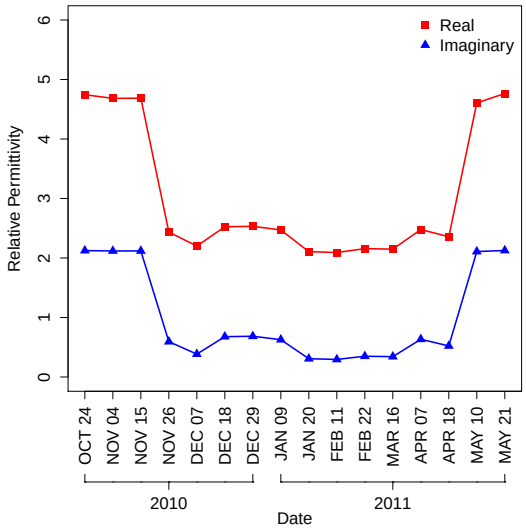
In general agreement with the Oh model is greatest for the TerraSAR-X VV measurements, which achieved average differences of ∼1 dB for all roughness levels. TerraSAR-X VH and all UW-Scat measurements achieved differences of ∼7.5 dB for the 1.84 cm roughness level, demonstrating poor but consistent agreement with Oh model estimates. A portion of the greater agreement for TerraSAR-X VV measurements in comparison to UW-Scat may be related to the increased sensitivity of UW-Scat to near-surface snow properties owing to its closer proximity to the surface, as demonstrated by Baumgartner *et al.* (2002). The increased distance between TerraSAR-X and the surface allows for greater scattering below the snowpack, increasing the volume scattering component and thus increasing backscatter (Baumgartner *et al.*, 2002).

Table 5.1: Average σ^o differences between TerraSAR-X, UW-Scat and the Oh model using TD GRMDM estimates (UW-Scat & TerraSAR-X - Oh Model). Pre-Excavation refers to differences calculated for UW-Scat measurements obtained prior to initiation of excavation procedure at study site. Post-Excavation refers to differences calculated for UW-Scat measurements obtained after snow was removed from the study site. Note that excavation differences are not averages as only one UW-Scat excavation scan was taken per site. Units are in dB.

Polarization	Roughness Level	UW-Scat		TerraSAR-X
		Pre-Excavation	Post-Excavation	
HH	0.62	9.27	7.81	N/A
	1.15	7.40	5.97	
	1.84	7.15	5.74	
VV	0.62	9.64	6.94	1.20
	1.15	7.83	5.10	-0.56
	1.84	7.62	4.87	-0.76
HV	0.62	11.43	9.91	10.54
	1.15	8.60	7.06	7.77
	1.84	8.04	6.49	7.23



(a)



(b)

Figure 5.10: TD GRMDM $\epsilon_r^{'}$ and $\epsilon_r^{''}$ estimates used within the Oh model. (a) 9.6 GHz Estimates for UW-Scat. (b) 9.65 GHz Estimates for TerraSAR-X acquisitions.

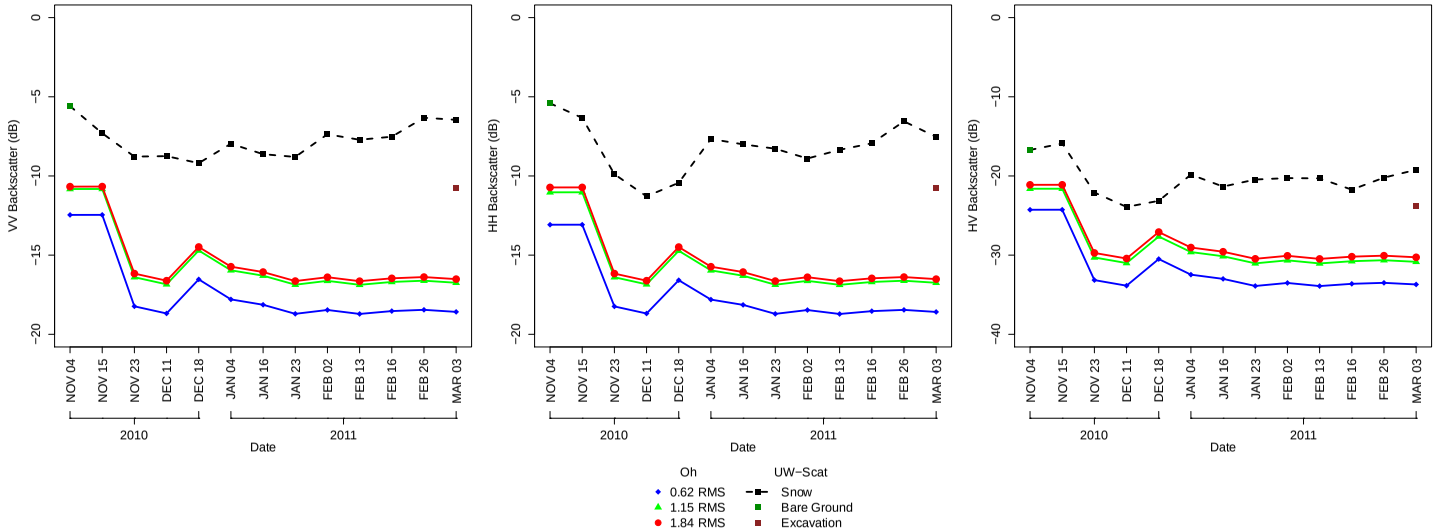


Figure 5.11: Agreement between Oh model and UW-Scat backscatter with TD GRMDM 9.6 GHz ϵ_r estimates used within the Oh model. Agreement for VV, HH and HV is shown in the left, centre and right figures respectively. Note the different scale for HV.

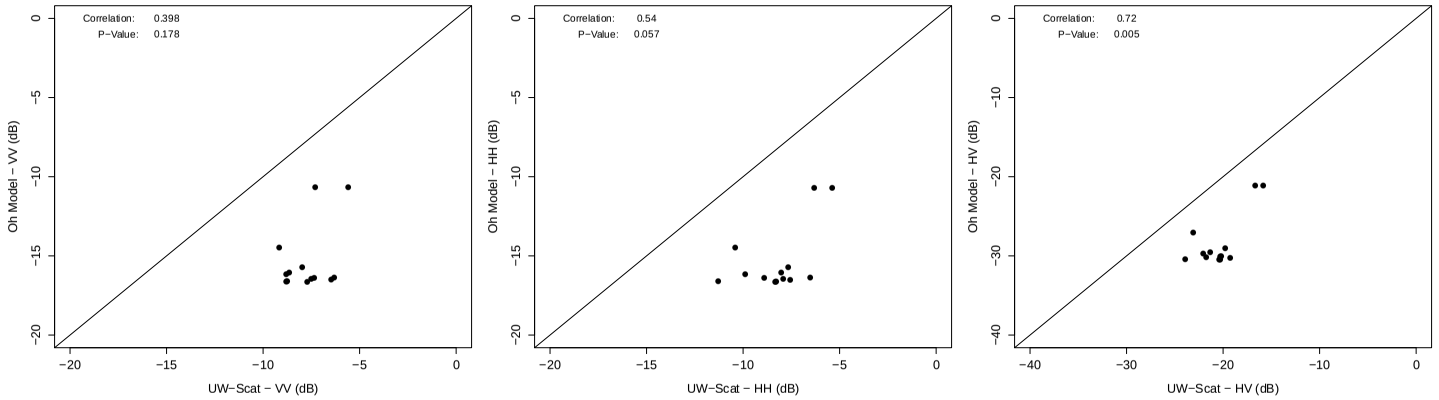


Figure 5.12: Correlation between Oh model and UW-Scat backscatter with TD GRMDM 9.6 GHz ϵ_r estimates used within the Oh model. Polarizations are identical to those for Figure 5.11.

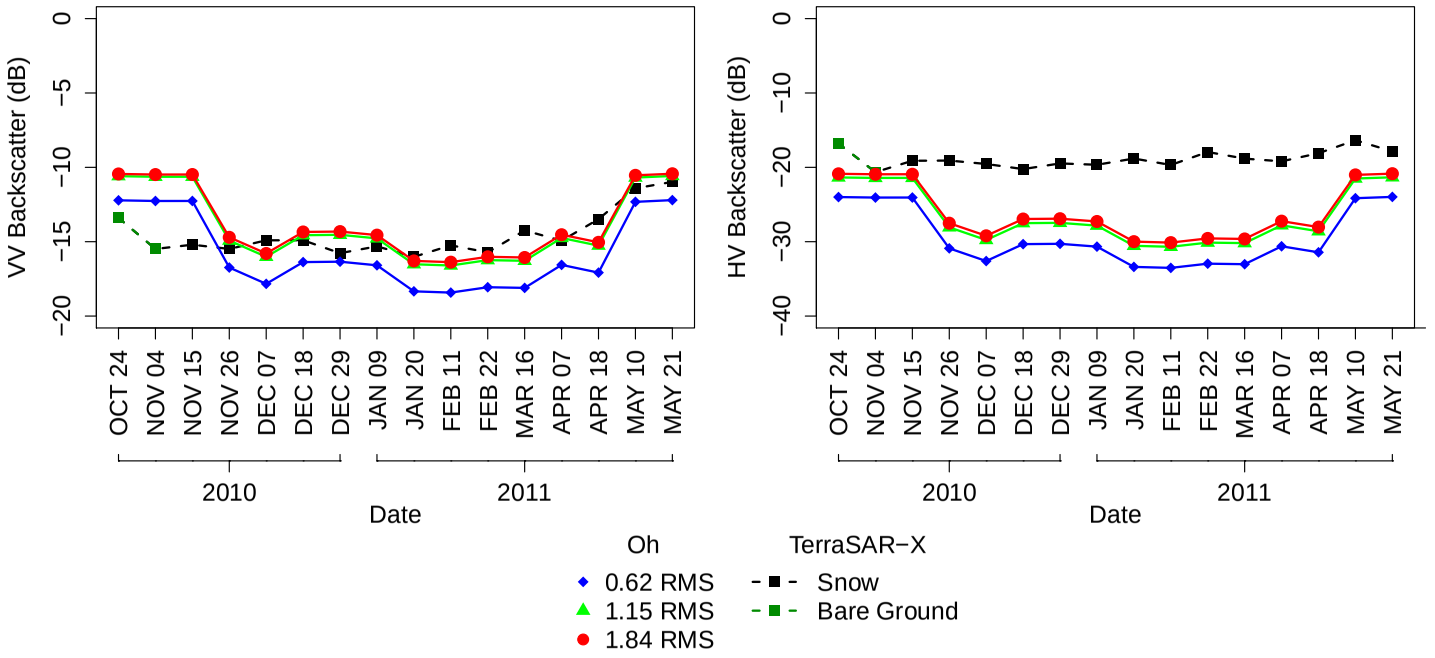


Figure 5.13: Agreement between Oh model and TerraSAR-X backscatter with TD GRMDM 9.65 GHz ϵ_r estimates used within the Oh model. Agreement for VV and HV polarizations is shown in the left and right figures respectively. Note the different plot scales.

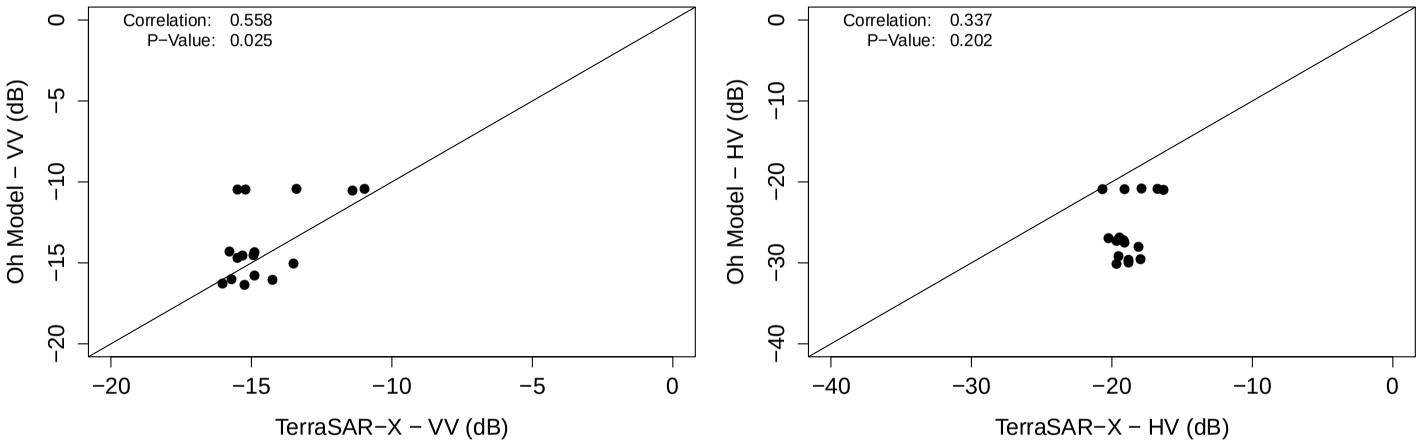


Figure 5.14: Correlation between Oh model and TerraSAR-X backscatter with TD GRMDM 9.65 GHz ϵ_r estimates used within the Oh model. Polarizations are identical to those for Figure 5.13.

5.2.2 Agreement Results using Measured ϵ_r

Figures 5.15 and 5.16 illustrate agreement between UW-Scat and TerraSAR-X measurements of X-band backscatter with corresponding Oh model estimates which used measured ϵ_r for parametrization. Table 5.2 presents average differences between the model estimates and remote sensing measurements for all RMS levels and polarizations. The ϵ_r values used within this comparison are not shown as they can be seen within the agreement figure for measured vs. TD GRMDM estimated ϵ_r (Figure 5.8). For UW-Scat (Figure 5.15) and TerraSAR-X (Figure 5.16), Oh estimates using measured ϵ_r demonstrate little variability throughout the study period. This resulted from the limited number of frozen ϵ_r measurements obtained during the whole form experiment. Soil temperatures for the top portion of the whole sample did not fall below -7°C, but measured values at the study site fell well below this level on certain dates. The influence of proper soil temperature representation is illustrated at December 18, where Oh model estimates do not capture the increase in UW-Scat backscatter (Figure 5.15). This increase was captured when using TD GRMDM ϵ_r estimates (Figure 5.11), which used *in situ* soil surface temperature measurements. The limited variation in soil surface temperature from the whole form experiment likely did not allow for moisture movement which may have occurred at the study site, limiting the ability of whole form ϵ_r measurements to contribute to appropriate Oh model estimates. Excluding the lack of variability, Oh estimates using measured ϵ_r exhibited improved agreement for both UW-Scat and TerraSAR-X, with average differences reaching no more than 9 dB. The 1.84 cm roughness level achieved the greatest agreement on average, with differences less than 6 dB occurring for all UW-Scat and TerraSAR-X polarizations.

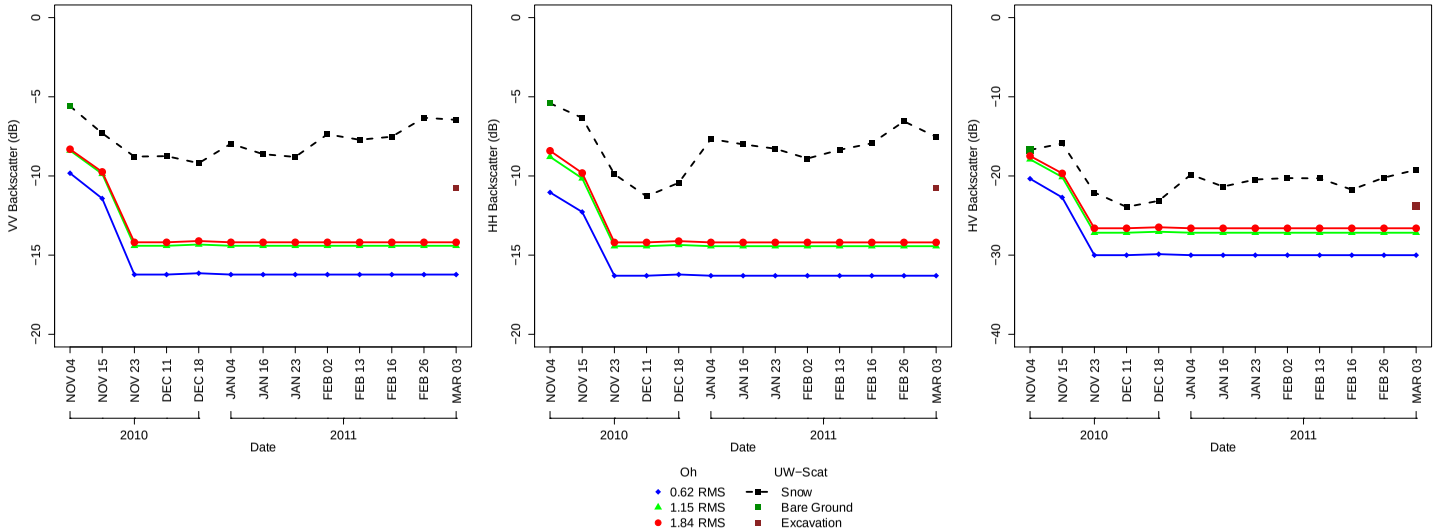


Figure 5.15: Agreement between Oh model and UW-Scat backscatter with measured ϵ_r used within the Oh model. Agreement for VV, HH and HV polarizations is shown in the left, centre and right figures respectively.

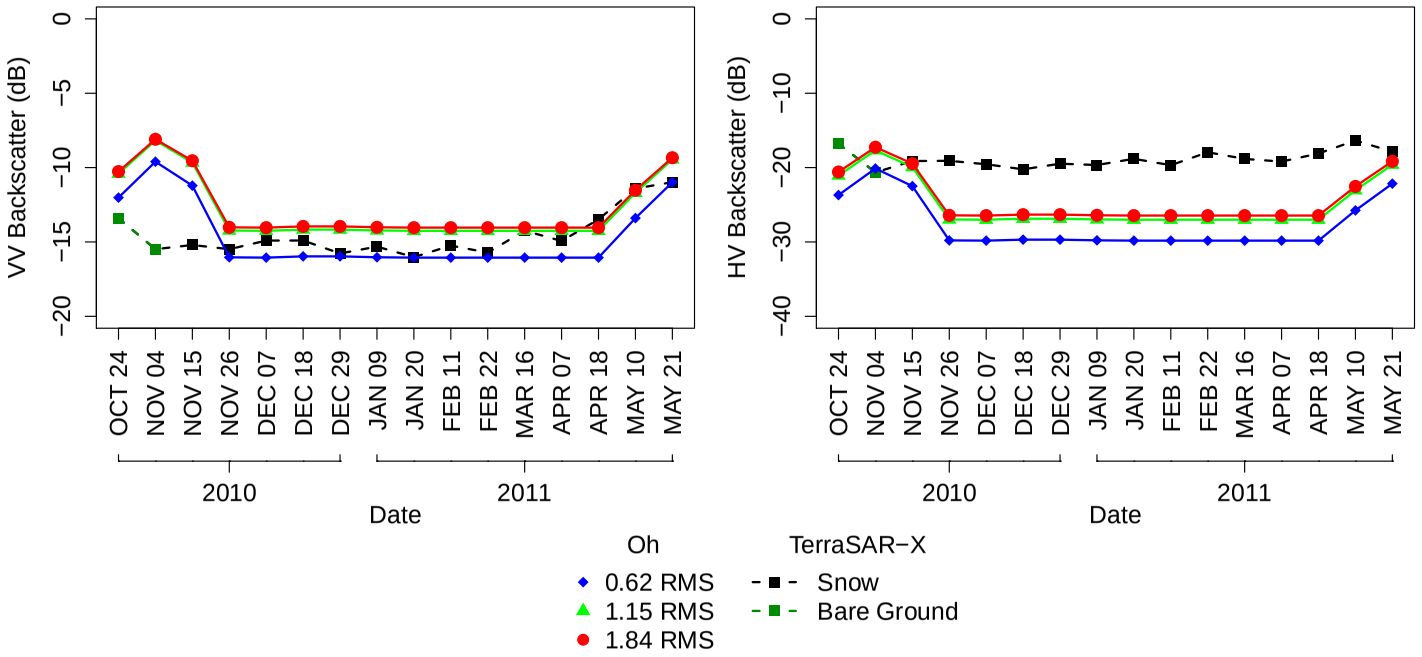


Figure 5.16: Agreement between Oh model and TerraSAR-X backscatter with measured ϵ_r used within the Oh model. Agreement for VV and HV backscatter is shown in the left and right figures respectively.

Table 5.2: Average σ^o differences between TerraSAR-X, UW-Scat and the Oh model using measured ϵ_r (UW-Scat & TerraSAR-X - Oh Model). Pre-Excavation refers to differences calculated for UW-Scat measurements obtained prior to initiation of excavation procedure at study site. Post-Excavation refers to differences calculated for UW-Scat measurements obtained after snow was removed from the study site. Note that excavation differences are not averages as only one UW-Scat excavation scan was taken per site. Units are in dB.

Polarization	Roughness Level	UW-Scat		TerraSAR-X
		Pre-Excavation	Post-Excavation	
HH	0.62	7.38	5.52	N/A
	1.15	5.46	3.66	
	1.84	5.21	3.42	
VV	0.62	7.64	4.58	0.11
	1.15	5.87	2.77	-1.61
	1.84	5.66	2.54	-1.80
HV	0.62	8.30	6.22	8.85
	1.15	5.51	3.38	6.11
	1.84	4.97	2.82	5.59

5.2.3 Oh Model Evaluation Discussion

From the comparison results, it is clear that the Oh model's representation of sub-Arctic terrain X-band backscatter is not ideal. In most cases model estimates consistently underestimate all UW-Scat measurements (Figures 5.11 and 5.15) and TerraSAR-X VH measurements (Figures 5.13 and 5.16) measurements. TerraSAR-X VV measurements present an exception with improved agreement with the Oh model. ϵ_r estimates and measurements used to produce Oh model estimates contributed to this result. Estimates using measured ϵ_r (Figures 5.15 and 5.16) did not allow the Oh model to capture variation in UW-Scat and TerraSAR-X measurements observed during winter portions of the study period. The minimum temperature achieved during the whole form peat experiment (i.e. -7°C) was insufficient to capture the range of freezing soil surface temperatures observed at the study site. In addition, while these measurements were obtained from a peat sample acquired from the study site, its characteristics at the time of measurement may not have matched those of the study site during the study period. The exact nature of these potential differences cannot be quantified as soil measurements were not performed during the study period.

Oh model estimates derived using TD GRMDM ϵ_r estimates captured more of the variation exhibited by UW-Scat (Figure 5.11) and TerraSAR-X (Figure 5.13) backscatter. Soil surface temperature likely contributed to this result by enabling improved TD GRMDM estimates for each acquisition. Due to offsets between the timing of soil temperature measurements and the remote sensing measurements, improved agreement may have been achieved with selecting appropriately timed soil surface temperatures.

Estimates produced for TerraSAR-X VV measurements achieved the best result of all comparisons, with average differences of $\sim$ 1.5 dB occurring for all RMS levels. This improved agreement is interesting as estimates for UW-Scat VV measurements did not exhibit increased agreement. Agreement for TerraSAR-X VH measurements also suggest sensor type does not contribute to improved agreement. At this stage it is difficult to identify a specific reason for higher TerraSAR-X VV agreement. Potential error in the Oh model may be a primary cause as UW-Scat and TerraSAR-X VV measurements were not substantially different. The use of different frequencies for each comparison could have impacted this result, but it does not appear to be a factor for TerraSAR-X HV estimates, which demonstrated similar agreement as UW-Scat HV estimates using TD GRMDM (Figure 5.13 and measured (Figure 5.16) ϵ_r. Further investigation of the model's calculation of VV backscatter may be required to fully understand improved agreement for this polarization.

Improved agreement for UW-Scat excavation measurements (Figures 5.11 and 5.15) also

suggests a potential influence of snow on backscatter. Excavation measurements produced ∼2 dB improvement in agreement for UW-Scat comparisons for all polarizations. This influence is also supported by improved agreement for bare ground UW-Scat and TerraSAR-X measurements. The increase in agreement for bare ground acquisitions is less consistent than that for excavation measurements, possibly because of variations in soil conditions (i.e. soil moisture). It is also possible that the improved agreement observed for excavation measurements was due to the removal of other scattering mechanisms, such as vegetation. It is only through a less destructive snow removal technique that this observation will be fully understood.

Overall, these results demonstrate uncertainty for Oh model representation of backscatter from snow covered organic terrain. In the majority of cases, model estimates fell below measurements obtained by UW-Scat and TerraSAR-X. Oh estimates which used TD GRMDM ϵ_r were better able to represent variation in UW-Scat (Figure 5.11) and TerraSAR-X (Figure 5.13) measurements, particularly during winter months, due to the incorporation of measured soil surface temperatures. Minimum temperatures explored within the whole form peat experiment did not reach those observed at the study site, limiting the appropriateness of measured ϵ_r within the Oh model and producing the limited estimate variability observed in Figures 5.15 and 5.16. TerraSAR-X VV measurements presented an exception to the poor agreement with sub-decibel agreement observed throughout the study period. Further research will be required to fully understand this observation. Potential influence of snow was also identified through improved agreement with UW-Scat excavation measurements, as well as bare ground TerraSAR-X and UW-Scat measurements. This finding was not expected and challenges the potential use of the Oh model within future dual-frequency Ku- and X-band SWE retrieval missions. This is explored further in the following section.

5.3 Oh Model Applicability within Potential Dual-Frequency SWE Retrieval Missions

The proposed use of the Oh model within potential dual-frequency SWE retrieval missions relies on the theoretical transparency of shallow dry snow at X-band as explained in Section 2.2.2. The apparent influence of snow demonstrated through Oh model comparisons with UW-Scat excavation as well as TerraSAR-X and UW-Scat bare ground measurements challenges this assumption; therefore, the appropriateness of using the existing Oh model approach within SWE retrieval algorithms is uncertain.

The observed potential influence of snow may be the result of snow conditions at the study site. Depth hoar comprised the bottom portion of the snow pack throughout the winter months, developing larger grains over time (maximum of 4.8 mm). Eventually, the aggregation of these grains may have produced sufficiently sized structures to influence X-band signals from UW-Scat and TerraSAR-X signals through volume scattering, increasing backscatter. Removal of the depth hoar layer, represented by UW-Scat excavation measurements, would have eliminated this scattering component, reducing backscatter and improving agreement with Oh model estimates. Improved agreement with bare ground measurements also demonstrates the capability of the Oh model to better represent UW-Scat and TerraSAR-X backscatter when volume scattering from vegetation and/or snow is absent. From these results, applying the Oh model with no modification appears to be inappropriate for representation of X-band backscatter from the snow covered terrain of the study site. This finding suggests that the proposed use of the model within a Ku- and X-band retrieval framework should be re-evaluated for application in sub-Arctic areas.

It must be noted that these results only apply to the snow and soil conditions of the study site. However, the environment of the study site, namely high winds with low temperatures, complex snow conditions characterized by substantial depth hoar development, and subsequent complex backscatter interactions is not dissimilar to other Arctic and sub-Arctic tundra regions. Organic soil conditions with high moisture content contribute significantly to this complexity through high permittivity conditions. The lack of substantial previous research in sub-Arctic organic soil landscapes prevents the analysis of the applicability of these conditions in other high latitude regions. This research has demonstrated that under different snow and soil conditions, Oh model agreement with X-band measurements may be more acceptable than results observed within this research. As well, the original design of the Oh model did not intend for its application within organic soil environments. The good agreement identified in this research, such as for TerraSAR-X VV measurements, suggests potential for improved application within organic soil environments through inclusion of these soil characteristics within the modelling framework. Through further understanding of snow and soil conditions in sub-Arctic regions, improved representations of active microwave scattering may be possible. Such work should be undertaken with a direct focus on multi-frequency radar retrievals in order to fully understand the appropriateness of the model for use within areas of focus for future dual-frequency SWE retrieval missions.

5.4 Recommendations for Oh Model Improvement

With the observed deficiencies in Oh model X-band backscatter representation for sub-Arctic terrain of the HBL, an opportunity exists to improve the model for this environment. This improvement can be achieved through the two primary parameters of the model, namely soil surface roughness and ϵ_r.

With respect to soil surface roughness, the highest bare soil roughness level explored in this research (1.84 cm) was well within the maximum validated RMS level examined during Oh model development (3.02 cm) (Oh *et al.*, 1992). However, additional surface roughness, presented primarily through vegetation, is not accounted for within the model. While development of a vegetation scattering model specific to sub-Arctic environments may improve the representation of surface roughness within the Oh model, the degree of improvement will depend on the vegetation characteristics within a given region. As demonstrated by Magagi *et al.* (2002), small scale vegetation structures, which are common in sub-Arctic regions, are not able to exceed the backscatter contributions of snow and the snow-ground interface. Larger structures, represented primarily through trees, can generate signal interaction under the correct conditions. Thus, the importance of vegetation within SWE retrieval algorithms will depend on the regions being observed. Improved understanding of sub-Arctic vegetation interaction with X-band signals, followed by development of representations for this interaction, may thus improve Oh model estimates of sub-Arctic backscatter.

The greatest area for Oh model estimate improvement may be found through the representation of ϵ_r. As demonstrated through limited variation in Oh model estimates using measured ϵ_r (Figures 5.15 and 5.16), improper representation of ϵ_r will contribute to poor model agreement. Enhancement of TD GRMDM estimates present the best opportunity for Oh model representation improvement, as *in-situ* ϵ_r measurements are impractical within a satellite retrieval program. Substantial TD GRMDM improvement may be achieved through representation of soil in its natural state, rather than the destroyed soil structure explored within Mironov *et al.* (2010). As observed through the replication of TD GRMDM soil measurements within this research (Section 5.1.4), the ground soil method does not allow for an accurate representation of natural soil, particularly for the natural moisture condition of organic sub-Arctic soil (Figure 5.9). Enhancement of TD GRMDM for a natural soil structure would substantially improve the quality of ϵ_r estimates for sub-Arctic soil. TD GRMDM was also not designed for the high soil moisture contents observed in this research. Expanding the model's validation to higher moisture contents should improve the representation of ϵ_r within the HBL and other sub-Arctic areas. With the development of improved ϵ_r, further evaluation of the

Oh model with ϵ_r estimates characteristic of natural sub-Arctic terrain will be required to ensure it operates correctly under realistic organic sub-Arctic soil ϵ_r characteristics.

Oh model improvement should be conducted thorough *in situ* measurement of soil surface roughness and/or, in conjunction with ground-based remote sensing observations of sub-Arctic terrain through a freeze up and thawing out regime. A primary motivator of this research was the lack of existing understanding of sub-Arctic soil characteristics and their impact on X-band measurements. This remains an important issue, particularly for improving our understanding of sub-Arctic organic soil characteristics over large areas. It is only through in-depth field campaigns at locations with various soil and climate conditions that sub-Arctic soil properties, and subsequently Oh model representation of these properties for microwave observations, can be properly evaluated.

Chapter 6

Conclusion

This research has explored the application of the Oh soil scattering model for representation of X-band backscatter from sub-Arctic terrain of the HBL region of Canada. Using *in situ* measurements of soil surface roughness, as well as modelled and measured soil ϵ_r values, derived Oh model estimates were compared to UW-Scat and TerraSAR-X measurements acquired during the winter of 2010 - 2011. Results of these comparisons have revealed uncertainty in the application of the Oh model for backscatter representation of the organic terrain of the study site. These results also call into question the use of the existing Oh model within a dual-frequency SWE retrieval framework. However, this research has also identified potential for improved Oh model application within sub-Arctic organic soil environments through improved understanding and inclusion of these soil characteristics within the modelling framework.

Observed uncertainty did not result entirely from the model. TD GRMDM estimates, while allowing the Oh model to better represent variations in UW-Scat and TerraSAR-X backscatter from months experiencing frozen soil conditions, exhibited uncertainties with representing measured ϵ_r from soil obtained from the study area. In addition, measured ϵ_r values were not obtained for the minimum soil surface temperature observed at the study site, limiting their capability for proper ϵ_r representation of soil conditions at the time of UW-Scat and TerraSAR-X acquisitions. Nevertheless, measured and estimated ϵ_r values did allow for good agreement with TerraSAR-X VV measurements, illustrating potential for the model's use under sub-Arctic organic soil conditions.

Measured soil surface roughness values may also exhibit uncertainty as they were not obtained in conjunction with UW-Scat and TerraSAR-X measurements. However, based on low rates of terrestrial change within the HBL region, it is unlikely that soil surface

roughness characteristics were altered substantially between UW-Scat/TerraSAR-X acquisitions and roughness measurement. The limited area over which soil surface roughness measurements were performed may also limit their appropriateness for representing the roughness condition of UW-Scat and TerraSAR-X's field of view. Due to the consistent nature of the terrain at the study site, this limitation is not expected to substantially alter the characterization of the site's surface roughness within the fields of view of TerraSAR-X and UW-Scat.

Unexpected uncertainty was also presented by the potential influence of snow in UW-Scat and TerraSAR-X backscatter. UW-Scat excavation measurements as well as bare ground TerraSAR-X and UW-Scat acquisitions demonstrated improved agreement with Oh model estimates in all cases, illustrating the potential influence of volume scattering of snow through depth hoar. It is also possible that the reduction of surface roughness through the removal of vegetation may have contributed to this result. Further research implementing less destructive snow removal techniques will be required to fully quantify the potential volume scattering of snow observed within this research, particularly as this finding would not be supported by the majority of previous research involving X-band backscatter from snow covered terrain.

These results illustrate significant challenges for Oh model application within the sub-Arctic environment of the study site. Without the inclusion of an organic soil sub-layer, it is unlikely that the model will be able to completely represent X-band backscatter obtained from organic soil conditions, particularly as the model was not designed to incorporate potential influences of high soil moisture, frozen soil and organic soil components which characterize many sub-Arctic areas. Therefore, the application of the Oh model within a dual-frequency Ku- and X-band retrieval framework without further modification for organic soil scattering may increase uncertainty in retrievals obtained over sub-Arctic regions. Through increased understanding of roughness, soil moisture and ϵ_r for organic sub-Arctic soils, in addition to potential snow scattering from these environments, improvements to model design may allow for improved retrieval applications to be developed.

APPENDICES

Appendix A

TD GRMDM Evaluation Plots for Bottom Peat Samples

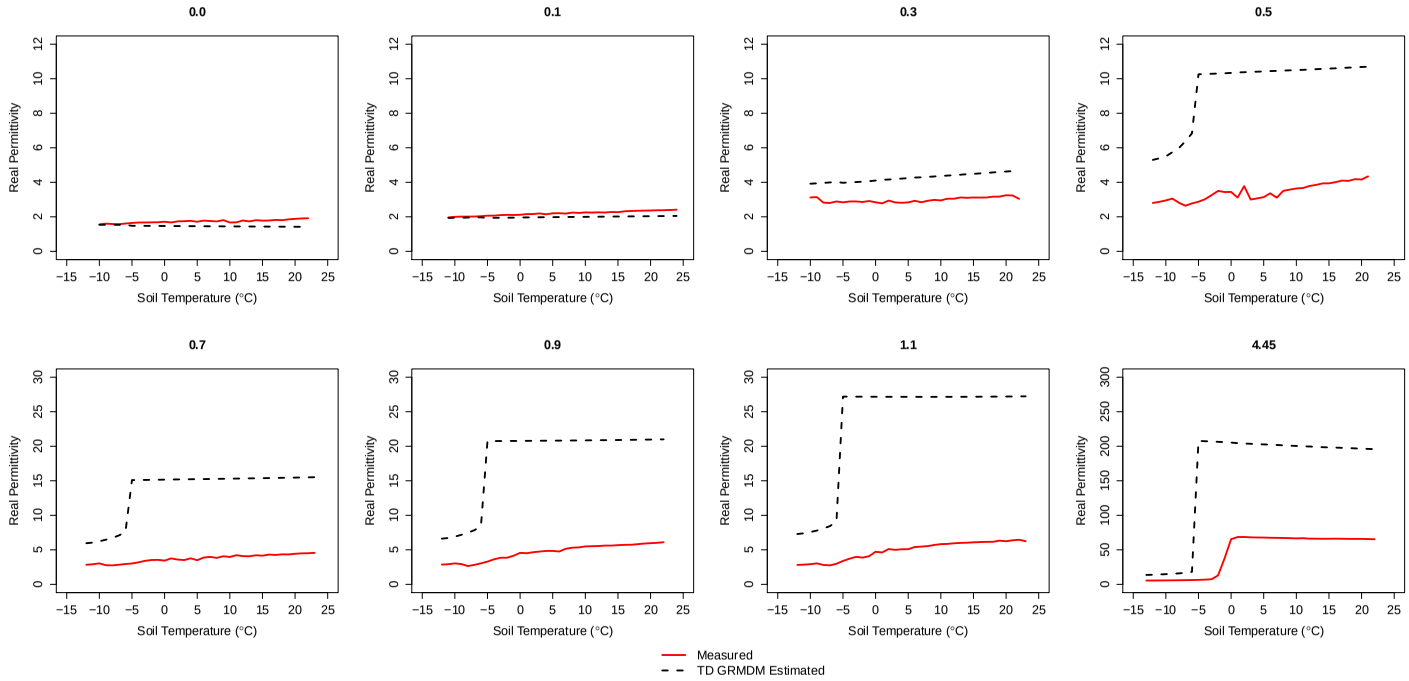


Figure A.1: Agreement between measured and TD GRMDM 50 MHz estimates of $\epsilon_r^{'}$ obtained for the ground-up bottom sample. Gravimetric moisture levels of 0.0, 0.1, 0.3, 0.5, 0.7, 0.9, and 1.1 g/g represent a sample of moisture levels examined within TD GRMDM. The 3.97 g/g level represents the measured gravimetric moisture of the small scale bottom sample in its field state.

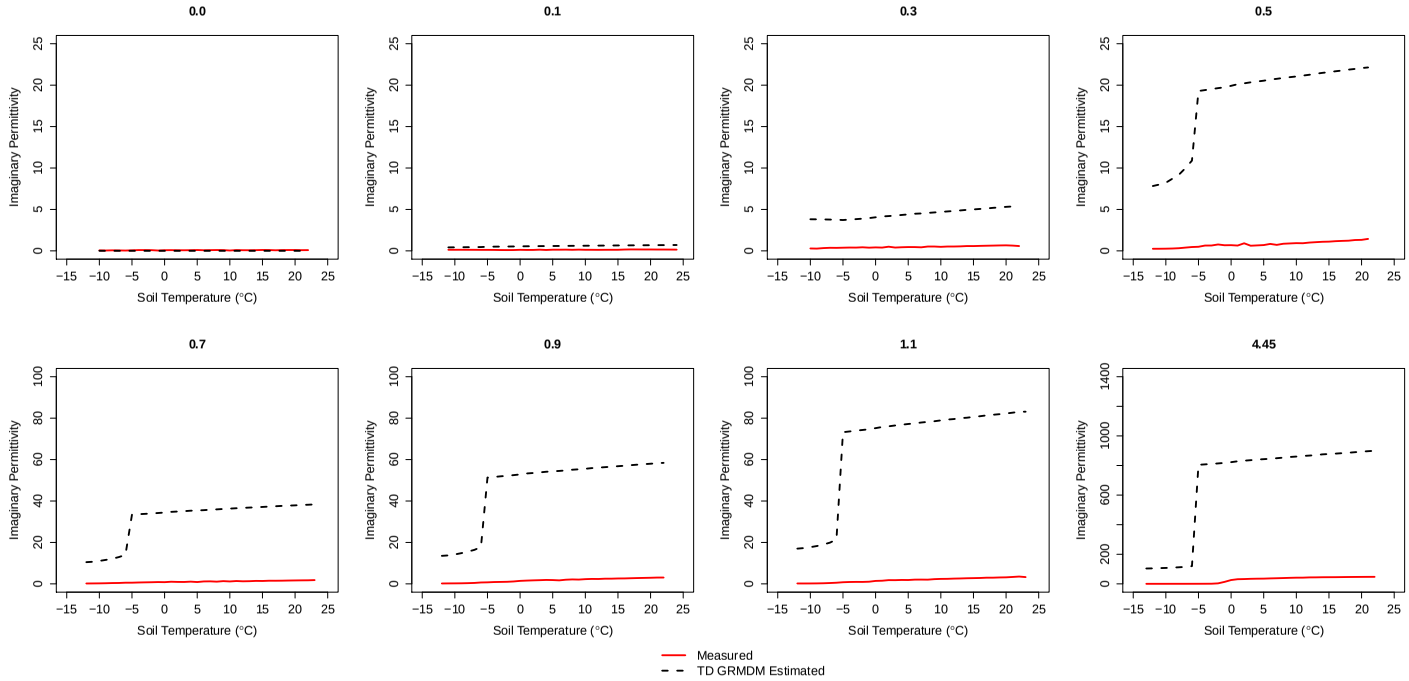


Figure A.2: Agreement between measured and TD GRMDM 50 MHz estimates of ϵ_r'' obtained for the ground-up bottom sample. See Figure A.1 for an explanation of presented moisture levels.

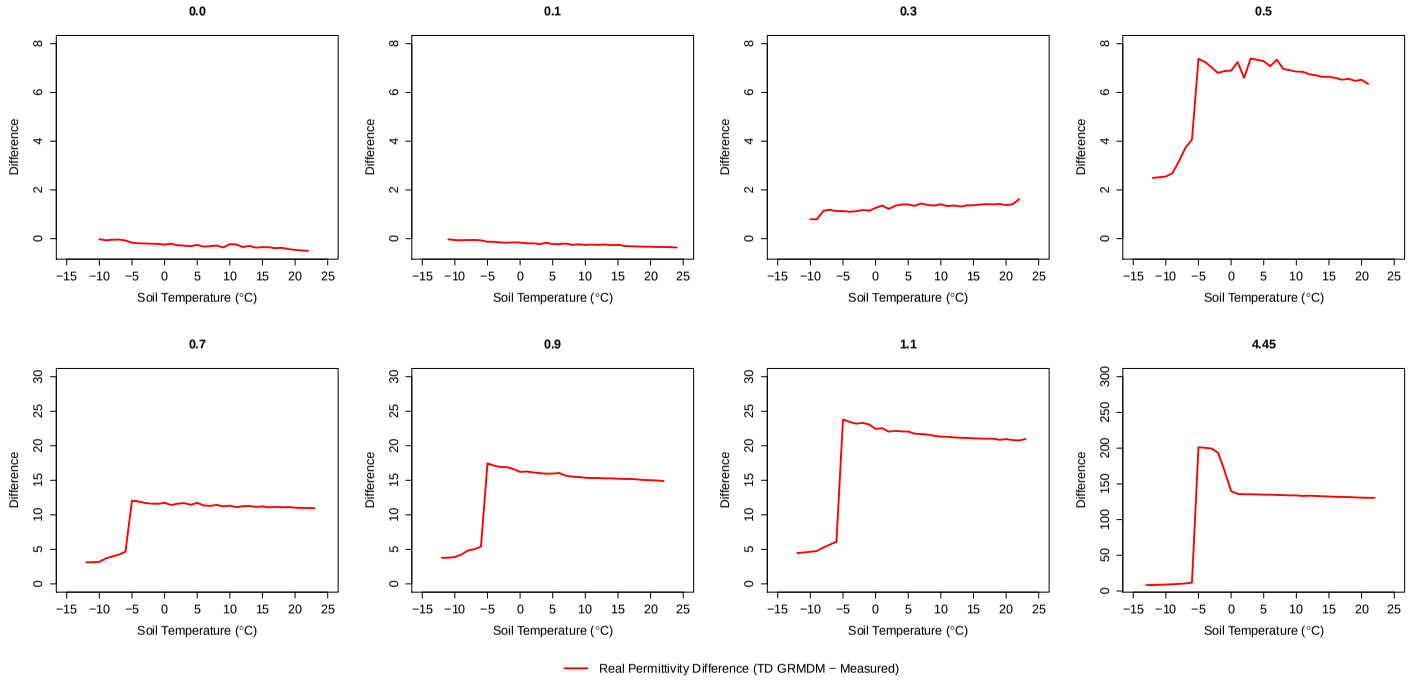


Figure A.3: Differences between measured and TD GRMDM 50 MHz estimates of $\epsilon_r^{'}$ obtained for the ground-up bottom sample (TD GRMDM - Measured).

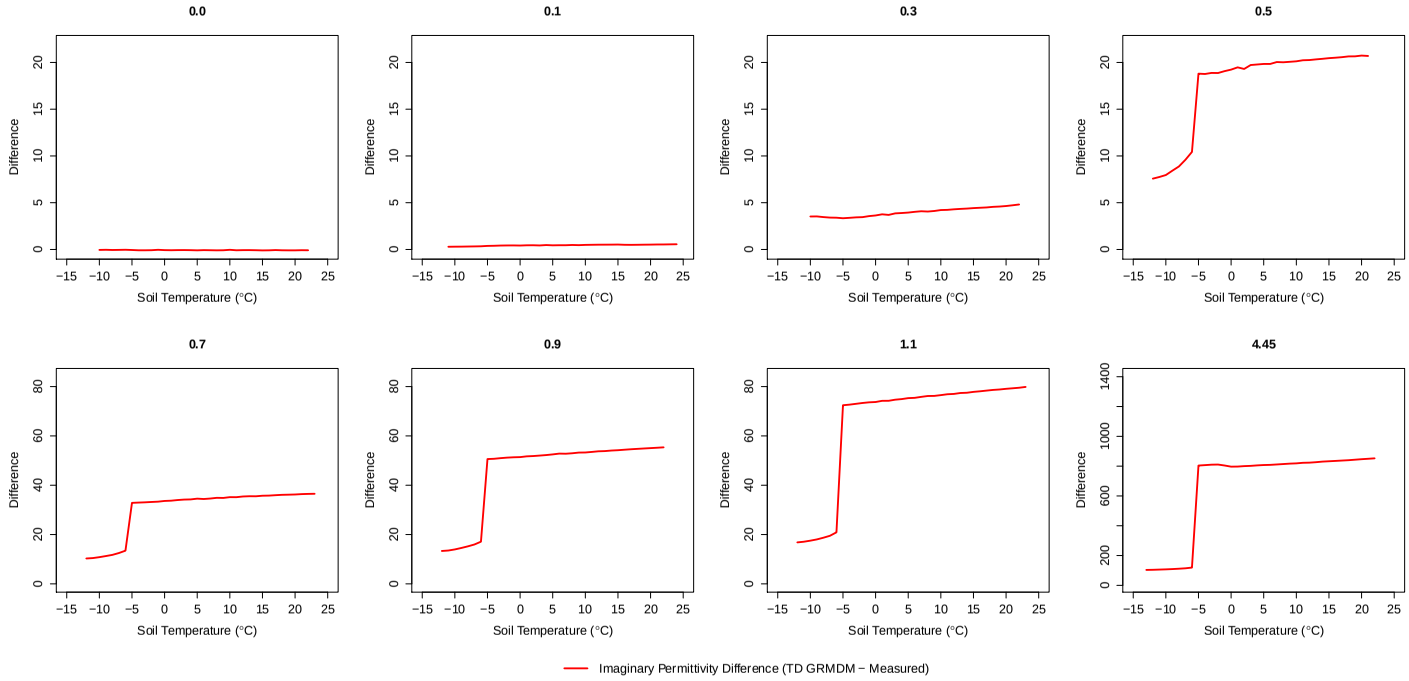


Figure A.4: Differences between measured and TD GRMDM 50 MHz estimates of ϵ_r'' obtained for the ground-up bottom sample (TD GRMDM - Measured).

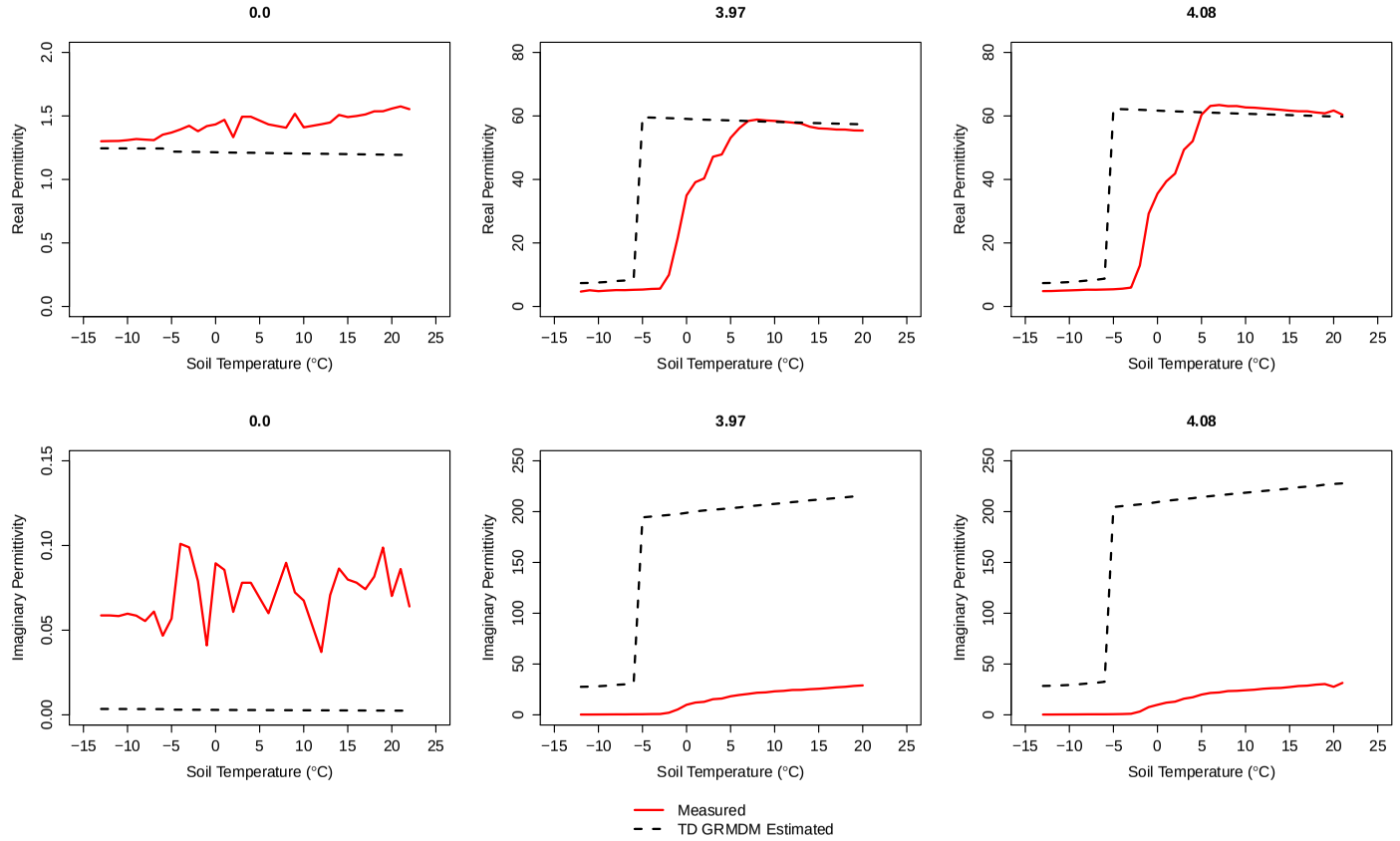


Figure A.5: Agreement between measured and TD GRMDM 50 MHz estimates of $\epsilon_r^{'}$ and $\epsilon_r^{'}$ for the small bottom sample. Gravimetric moisture levels of 0.0, 3.97 and 4.08 g/g represent the sample in its dried, field state and saturated conditions respectively.

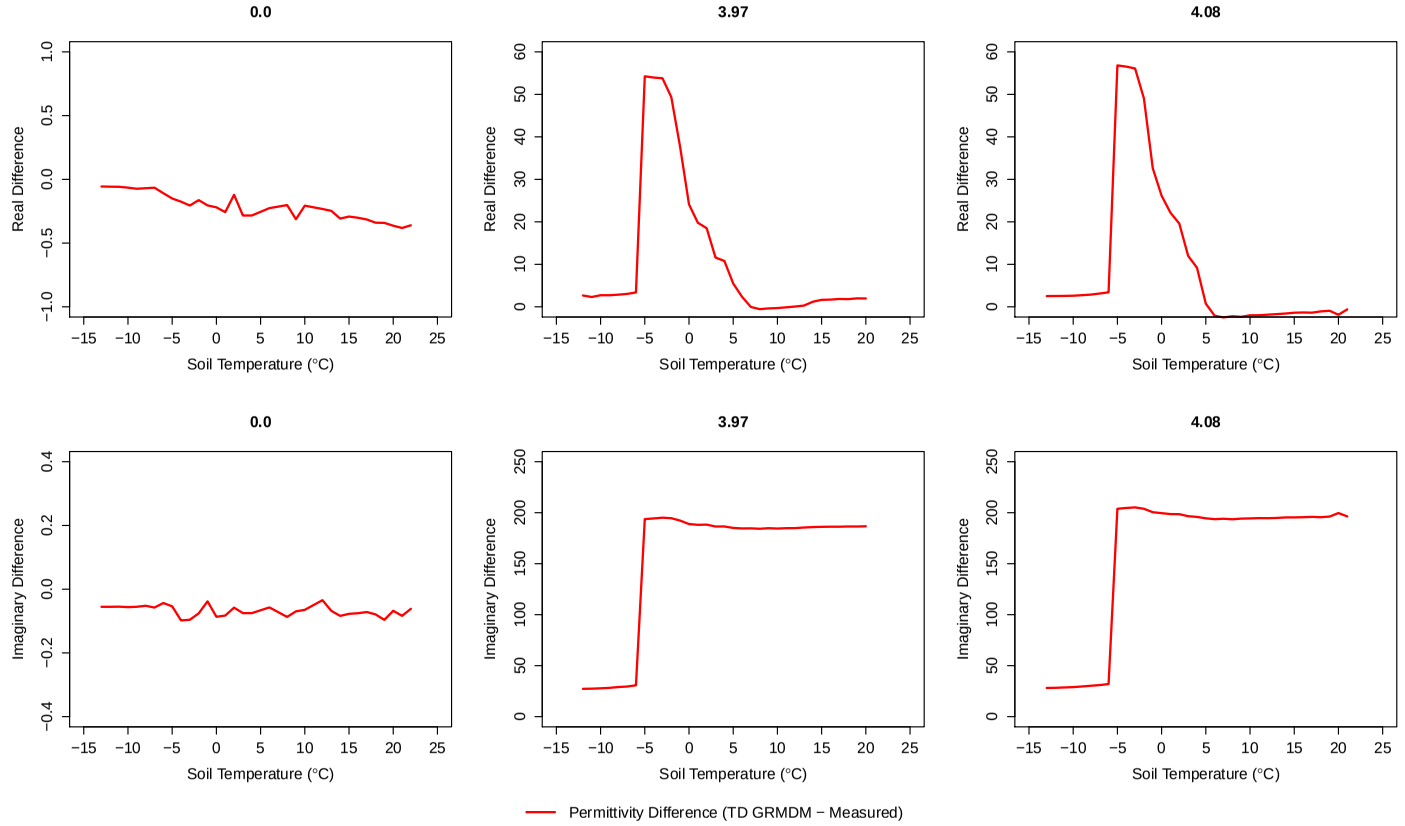


Figure A.6: Differences between measured and TD GRMDM 50 MHz estimates of $\epsilon_r^{'}$ and $\epsilon_r^{''}$ obtained for the small bottom sample (TD GRMDM - Measured).

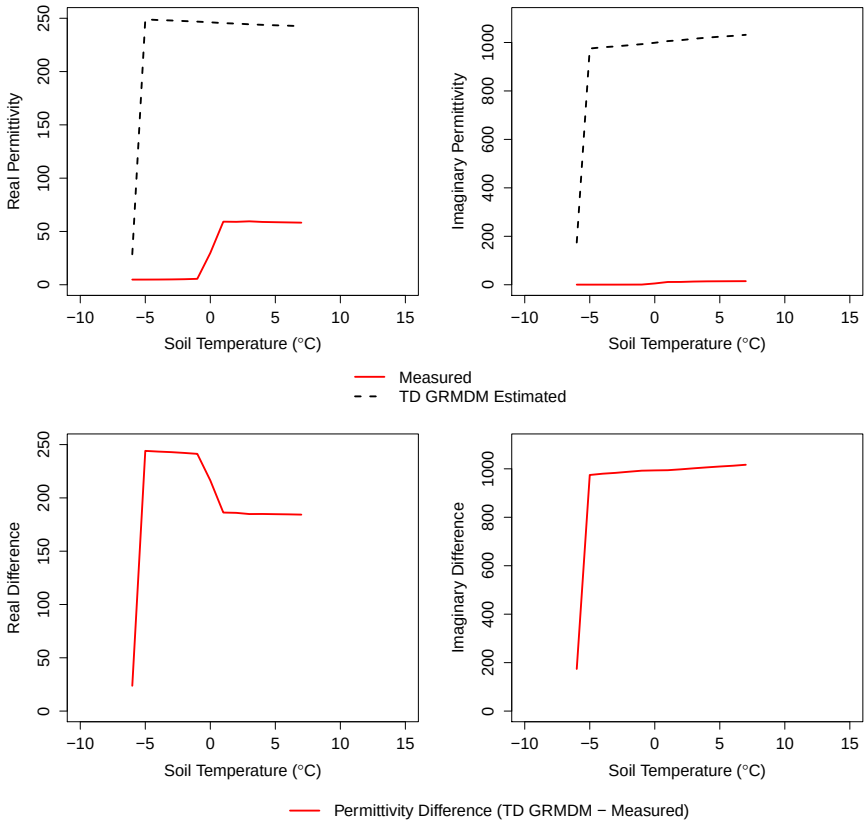


Figure A.7: Agreement (top) and differences (bottom) between measured and TD GRMDM 50 MHz estimates of $\epsilon_r^{'}$ and $\epsilon_r^{''}$ obtained for bottom portion of the whole sample (TD GRMDM - Measured).

References

Abraham, K. F., & Keddy, C. J. 2005. *The World's Largest Wetlands: Ecology and Conservation*. New York, NY: Cambridge University Press. Chap. 4: The Hudson Bay Lowland, pages 118–148.

ASTM International. 2010. *ASTM Standard D2216-10: Standard Test Methods for Laboratory Determination of Water (Moisture) Content of Soil and Rock by Mass*.

Atlas of Canada. 2009. *Atlas of Canada - Shapefile of Canadian Provinces*. Computer File. Available Online: http://geogratis.cgdi.gc.ca/geogratis/en/option/select.do?id=0BCF289A-0131-247B-FDBD-4CC70989CBCB.

Bartnikas, R. 1997. *The Electrical Engineering Handbook*. 2nd edn. Boca Raton, FL: CRC Press. Chap. 55: Dielectrics and Insulators.

Baumgartner, F., Munk, J., Jezek, K. C., & Gogineni, S. 2002. On Reconciling Ground-Based with Spaceborne Normalized Radar Cross Section Measurements. *IEEE Transactions on Geoscience and Remote Sensing*, **40**(2), 494–496.

Bernier, M., & Fortin, J. 1991. Evaluation of the Potential of C- and X-band SAR Data to Monitor Dry and Wet Snow Cover. *Pages 2315–2318 of: Geoscience and Remote Sensing Symposium, 1991. IGARSS '91. Remote Sensing: Global Monitoring for Earth Management., International*, vol. 4.

Bernier, M., & Fortin, J. P. 1998. The Potential of Time Series of C-Band SAR Data to Monitor Dry and Shallow Snow Cover. *IEEE Transactions on Geoscience and Remote Sensing*, **36**(1), 226–243.

Colbeck, S. C. 1982. The Geometry and Permittivity of Snow at High Frequencies. *Journal of Applied Physics*, **53**(6), 4495–4500.

Cumming, W. A. 1952. The Dielectric Properties of Ice and Snow at 3.2 Centimeters. *Journal of Applied Physics*, **23**(7), 768–773.

Dobson, M. C., & Ulaby, F. 1981. Microwave Backscatter Dependence on Surface Roughness, Soil Moisture, and Soil Texture: PArt III - Soil Tension. *IEEE Transactions on Geoscience and Remote Sensing*, **GE-19**(1), 51–61.

Duguay, C. R., Pultz, T. J., Lafleur, P. M., & Drai, D. 2002. RADARSAT Backscatter Characteristics of Ice Growing on Shallow, Sub-Arctic Lakes, Churchill, Manitoba, Canada. *Hydrological Processes*, **16**(8), 1631–1644.

Encyclopædia Britannica. 2013. Refractive Index. *In: Encyclopædia Britannica*.

Etzold, K. F. 2008. *RF and Microwave Passive and Active Technologies*. Boca Ratan, FL: CRC Press-Taylor & Francis Group. Chap. 27: Dielectrics.

European Space Agency. 2012. *Report for Mission Selection: CoReH$_2$O*. Tech. rept. ESA SP-1324/2.

Floricioiu, D., & Rott, H. 2001. Seasonal and Short-Term Variability of Multifrequency, Polarimetric Radar Backscatter of Alpine Terrain from SIR-C/X-SAR and AIRSAR Data. *IEEE Transactions on Geoscience and Remote Sensing*, **39**(12), 2634–2648.

Fox, M. 2001. *Optical Properties of Solids*. New York, NY: Oxford University Press.

French, H. M. 2007. *The Periglacial Environment*. 3rd edn. Hoboken, NJ: Wiley.

Goodison, B. E., Ferguson, H. L., & McKay, G. A. 1981. *Handbook of Snow: Principles, Processes, Management & Use*. Willowdale, ON: Pergamon Press. Chap. 6: Measurement and Data Analysis.

Grim, R. E. 1953. *Clay Mineralogy*. New York, NY: McGraw-Hill.

Hallikainen, M., & Winebrenner, D. P. 1992. *Microwave Remote Sensing of Sea Ice*. Washington, DC: American Geophysical Union. Chap. 3: The Physical Basis for Sea Ice Remote Sensing.

Hallikainen, M., Ulaby, F. T., & El-Rayes, M. 1984. Dielectric Measurements of Soils in the 3- to 37 GHz Band between -50°C and 23°C. *Pages 163–167 of: Geoscience and Remote Sensing Symposium, 1984. IGARSS '84. From Research Towards Operational Use., International*.

Hallikainen, M. T., Ullaby, F. T., Dobson, M. C., El-Rayes, M. A., & Wu, L. 1985. Microwave Dielectric Behavior of Wet Soil - Part 1: Empirical Models and Experimental Observations. *IEEE Transcations on Geoscience and Remote Sensing*, **GE-23**(1), 25–34.

Hallikainen, M. T., Ulaby, F. T., & Abdelrazik, M. 1986. Dielectric Properties of Snow in the 3 to 37 GHz Range. *IEEE Transactions on Antennas and Propogation*, **AP-34**(11), 1329–1340.

Heidinger, M., Nagler, T., & Rott, H. 2010. *Development of Snow Retrieval Algorithms for $CoReH_2O$*. Tech. rept. Enveo.

Hoekstra, P., & Delaney, A. 1974. Dielectric Properties of Soils at UHF and Microwave Frequencies. *Journal of Geophysical Research*, **79**(11), 1699–1708.

Infoterra GmbH. 2009. *TerraSAR-X Services - Image Product Guide*. Available Online: http://www2.astrium-geo.com/files/pmedia/public/r459_9_20091208_tsxx-itd-ma-0009_tsx-productguide_i1.00.pdf.

Jensen, J. R. 2007. *Remote Sensing of the Environment: An Earth Resource Perspective*. 2nd edn. Upper Saddle River, NJ: Pearson Prentice Hall.

Kendra, J R., Sarabandi, K., & Ulaby, F. T. 1998. Radar Measurements of Snow: Experiment and Analysis. *IEEE Transactions on Geoscience and Remote Sensing*, **36**(3), 864–879.

King, J. M. L., Kelly, R., Kasurak, A., Duguay, C., Gunn, G., & Mead, J. B. 2013. UW-Scat: A Ground-Based Dual-Frequency Scatterometer for Observation of Snow Properties. *IEEE Geoscience and Remote Sensing Letters*, **10**(3), 528–532.

Lafleur, P., Wurtele, A. B., & Duguay, C. R. 1997. Spatial and Temporal Variations in Surface Albedo of a Subarctic Landscape Using Surface-based Measurements and Remote Sensing. *Arctic and Alpine Research*, **29**(3), 261–269.

Lakowicz, J. R. 2006. *Principles of Fluorescence Spectroscopy*. 3rd edn. New York, NY: Springer.

Langham, E. J. 1981. *Handbook of Snow: Principles, Processes, Management & Use*. Willowdale, ON: Pergamon Press. Chap. 7: Physics and Properties of Snowcover.

Lillesand, T. M., Kiefer, R. W., & Chipman, J. W. 2008. *Remote Sensing and Image Interpretation*. 6th edn. Hoboken, NJ: John Wiley & Sons, Inc.

Mack, C. A. 2006. *Field Guide to Optical Lithography*. Bellingham, WA: SPIE Press.

Magagi, R., Bernier, M., & Bouchard, M. 2002. Use of Ground Observations to Simulate the Seasonal Changes in the Backscattering Coefficient of the Subarctic Forest. *IEEE Transactions on Geoscience and Remote Sensing*, **40**(2), 281–297.

Mätzler, C. 1987. Applications of the Interaction of Microwaves with the Natural Snow Cover. *Remote Sensing Reviews*, **2**, 259–387.

Mätzler, C., & Schanda, E. 1984. Snow Mapping with Active Microwave Sensors. *International Journal of Remote Sensing*, **5**(2), 409–422.

Mätzler, C., Schanda, E., & Good, W. 1982. Towards the Definition of Optimum Sensor Specifications for Microwave Remote Sensing of Snow. *IEEE Transactions on Geoscience and Remte Sensing*, **GE-20**(1), 57–66.

Mätzler, C., Strozzi, T., Weise, T., Floricioiu, D. M., & Rott, H. 1997. Microwave Snowpack Studies made in the Austrian Alps during the SIR-C/X-SAR Experiment. *International Journal of Remote Sensing*, **18**, 2505–2530.

Mironov, V. L., & Savin, I. V. 2010. Temperature Dependence of the Tundra Soil Permittivity during Freezing of Water in the Soil Capillaries. *Russian Physics*, **53**(9/3), 241–246.

Mironov, V. L., & Savin, I. V. 2011. Temperature Dependable Microwave Dielectric Model for a Pine Litter Thawed and Frozen. *PIERS Online*, **7**(8), 781–785.

Mironov, V. L., De Roo, R. D., & Savin, I. V. 2010. Temperature-Dependable Microwave Dielectric Model for an Arctic Soil. *IEEE Transactions on Geoscience and Remote Sensing*, **48**(6), 2544–2556.

Mitsch, W. J., & Gosselink, J. G. 2007. *Wetlands*. 4th edn. Hoboken, NJ: John Wiley & Sons, Inc.

Moreira, A., Prats-Iraola, P., Younis, M., Krieger, G., Hajnsek, I., & Papathanassiou, K. P. 2013. A Tutoiral on Synthetic Aperture Radar. *IEEE Geoscience and Remote Sensing Magazing*, **1**(1), 6–43.

Nagare, R. M., Schincariol, R. A., Quniton, W. L., & Hayashi, M. 2012. Effects of Freezing on Soil Temperature, Freezing Front Propagation and Moisture Redistribution in Peat: Laboratory Investigations. *Hydrology and Earth System Sciences*, **16**(2), 501–515.

National Aeronautics and Space Administration. 2010. *Landsat 5 Thematic Mapper Scene*. Computer File. Scene ID: L5031019_01920100904. Processing Level: L1T. Publisher: United States Geological Survey. Publisher Location: Sioux Falls, South Dakota. Image Date: September 4, 2010.

Oh, Y., Sarabandi, K., & Ulaby, F. T. 1992. An Empirical Model and an Inversion Technique for Radar Scattering from Bare Soil Surfaces. *IEEE Transactions on Geoscience and Remote Sensing*, **30**(2), 370–381.

R Development Core Team. 2011. *R: A Language and Environment for Statistical Computing*. R Foundation for Statistical Computing, Vienna, Austria. ISBN 3-900051-07-0.

Richards, J. A. 2009. *Remote Sensing with Imaging Radar*. Signals and Communication Technology. Springer.

Rott, H., Sturm, K., & Miller, H. 1993. Active and Passive Microwave Signatures of Antarctic Firn by means of Field Measurements of Satellite Data. *Annals of Glaciology*, **17**, 337–343.

Rott, H., Yueh, S. H., Cline, D. W., Duguay, C., Essery, R., Haas, C., Hélière, F., Kern, M., Macelloni, G., Malnes, E., Nagler, T., Pulliainen, J., Rebhan, H., & Thompson, A. 2010. Cold Regions Hydrology High-Resolution Observatory for Snow and Cold Land Processes. *Proceedings of the IEEE*, **98**(5), 752–765.

Scherer, D., Hall, D. K., Hochschild, V., König, M., Winther, J., Duguay, C. R., Pivot, F., Mätzler, C., Rau, F., Seidel, K., Solberg, R., & Walker, A. E. 2005. *Remote Sensing in Northern Hydrology: Measuring Environmental Change*. Washington, DC: American Geophysical Union. Chap. 1: Remote Sensing of Snow Cover.

Shi, J., Dozier, J., & Rott, H. 1993. Modeling and Observation of Polarimetric SAR Response to Dry Snow. *Pages 1042 –1045 of: Geoscience and Remote Sensing Symposium, 1993. IGARSS '93. Better Understanding of Earth Environment., International*, vol. 3.

Speers, D. D., Ashton, G. D., Rockwood, D. M., & Garen, D. C. 1996. *Hydrology Handbook*. Second edn. American Society of Civil Engineers. Chap. 7: Snow and Snowmelt.

Stevens Water Monitoring System Inc. 2007. *Comprehensive Stevens Hydra Probe Users Manual*.

Stiles, W. H., & Ulaby, F. T. 1980. The Active and Passive Microwave Response to Snow Paramters. 1: Wetness. *Journal of Geophysical Research: Oceans*, **85**(C2), 1037–1044.

Tarnocai, C. 2009. *Permafrost Soils*. Berlin: Springer. Chap. Arctic Permafrost Soils, pages 3–16.

The Institute of Electrical and Electronics Engineers. 1997. *IEEE Standard Definitions of Terms for Radio Wave Propagation*. Tech. rept. New York, NY.

Tse, K. K., Tsang, L., Chan, C. H., Ding, K. H., & Leung, K. W. 2007. Multiple Scattering of Waves by Dense Random Distributions of Sticky Particles for Applications in Microwave Scattering by Terrestrial Snow. *Radio Science*, **42**(5), 1–14.

Ulaby, F. T., & Stiles, W. H. 1980. The Active and Passive Microwave Response to Snow Parameters. 2: Water Equivalent of Dry Snow. *Journal of Geophysical Research: Oceans*, **85**(C2), 1045–1049.

Ulaby, F. T., Batlivala, P. P., & Dobson, M. C. 1978. Microwave Backscatter Dependence on Surface Roughness, Soil Moisture, and Soil Texture: Part I - Bare Soil. *IEEE Transactions on Geoscience Electronics*, **GE-16**(4), 286–295.

Ulaby, F. T., Moore, R. K., & Fung, A. K. 1982. *Microwave Remote Sensing: Active and Passive - Volume 2: Radar Remote Sensing and Surface Scattering and Emission Theory*. Norwood, MA: Artech House.

Ulaby, F. T., Stiles, W. H., & Abdelrazik, M. 1984. Snowcover Influence on Backscattering from Terrain. *IEEE Transactions on Geoscience and Remote Sensing*, **GE-22**(2), 126–133.

Ulaby, F. T., Moore, R. K., & Fung, A. K. 1986. *Microwave Remote Sensing: Active and Passive - Volume 3: From Theory to Applications*. Norwood, MA: Artech House.

Ulaby, F. T., Dubois, P. C., & van Zyl, J. 1996. Radar Mapping of Surface Soil Moisture. *Journal of Hydrology*, **184**(1-2), 57–84.

Wang, J. R., & Schmugge, T. J. 1980. An Empirical Model for the Complex Dielectric Permittivity of Soils as a Function of Water Content. *IEEE Transactions on Geoscience and Remote Sensing*, **18**(4), 288–295.

Wegmüller, U. 1990. The Effect of Freezing and Thawing on the Microwave Signatures of Bare Soil. *Remote Sensing of Environment*, **33**, 123–135.

Yoshino, T. 2011. *Encyclopedia of Solid Earth Geophysics*. Dordrecht, The Netherlands: Springer. Chap. Electrical Properties of Rocks.

Yueh, S. H., Dinardo, S. J., Akgiray, A., West, R., Cline, D. W., & Elder, Kelly. 2009. Airborne Ku-Band Polarimetric Radar Remote Sensing of Terrestrial Snow Cover. *IEEE Transactions on Geoscience and Remote Sensing*, **47**(10), 3347–3364.